Astronomy Letters, Vol. 29, No. 3, 2003, pp. 133–141. Translated from Pis'ma v Astronomicheskiĭ Zhurnal, Vol. 29, No. 3, 2003, pp. 163–171.

Observational Study of UGC 4892—a Candidate for Polar-Ring Galaxies

V. A. Hagen-Thorn, L. V. Shalyapina, G. M. Karataeva*, and V. A. Yakovleva

Astronomical Institute, St. Petersburg State University,
Universitetskiĭ pr. 28, Petrodvorets, St. Petersburg, 198504 Russia

Received October 3, 2002; in final form, October 11, 2002

Abstract—We present the results of photometric and spectroscopic observations of UGC 4892—a candidate for polar-ring galaxies. We show that the feature in the brightness distribution described by Whitmore *et al.* (1990) as a possible polar ring is actually a companion galaxy that interacts with the giant main galaxy. The velocity fields of the gas and stellar components can be explained by assuming that the gas lost by the companion galaxy and captured by the main galaxy forms a gaseous stream rotating around the latter in a plane almost perpendicular to its principal plane. © *2003 MAIK "Nauka/Interperiodica".*

Key words: *galaxies, groups and clusters of galaxies, intergalactic gas.*

INTRODUCTION

The galaxy UGC 4892 has a complex and unusual structure that is clearly illustrated in Fig. 1. We constructed this figure by processing a CCD frame obtained in the B band with the 6-m (BTA) telescope. Two bright condensations spaced 5″ apart can be seen at the center of the object. The northeastern (NE), brighter condensation is most likely the nucleus of the galaxy elongated in the E–W direction. Vorontsov-Velyaminov (1977) included UGC 4892 in his catalog of interacting galaxies under no. VV 593 by assuming it to be a binary galaxy and placed it in the Nests subgroup.

The brightness distribution exhibits a feature at a position angle of 198° from the nucleus with the second condensation lying at its base. Assuming this feature to be attributable to the existence of a kinematic system orthogonal to the principal plane of the galaxy, Whitmore *et al.* (1990) included UGC 4892 in their catalog (PRC) of polar-ring galaxies (PRGs), PRG candidates, and related objects under no. D-12 as an object related to PRGs.

Spectroscopic observations of UGC 4892 are available in Reshetnikov and Combes (1994), who provided radial-velocity curves constructed from emission lines for two position angles (82° and 195°). They found the radial velocity of the galaxy to be $V_{\rm Hel} = 7917$ km s^{-1}. Although the lack of correspondence between the figure and the text severely complicates the use of these data, we can assert that they established the existence of two nearly orthogonal kinematic systems.

*E-mail: narka@astro.spbu.ru

As far as we know, no detailed photometric study of UGC 4892 has been carried out. Therefore, the galaxy was included in the program of observations of PRG candidates that is being conducted at the Astronomical Institute of St. Petersburg State University. In this paper, we present the results of our photometric and spectroscopic studies of UGC 4892.

We found the radial velocity of the galaxy (after applying a correction of +23 km s^{-1} for galactic rotation) from absorption lines (see below) to be 7708 km s^{-1}. For $H_0 = 65$ km s^{-1} Mpc^{-1}, the distance to the galaxy is 119 Mpc, so 1″ corresponds to 0.58 kpc.

OBSERVATIONS AND DATA REDUCTION

The photometric observations of UGC 4892 were performed in March 1994 at the prime focus of the 6-m Special Astrophysical Observatory (SAO) telescope at seeing 1.″5–2″ in bands close to the Johnson B and V bands and in the Cousins $R_{\rm c}$ band (see Table 1). Direct images were obtained using a K983-type 530 × 580-pixel (18 × 24 μm each) CCD array with readout noise 12–20 e^-. The angular pixel size was 0.″15 × 0.″20, and the field of view was 1.′3 × 2.′0.

Table 1. Photometric observational material

Date	Band	Exposure, s	z, deg
Mar. 10, 1994	V	450	7
	$R_{\rm c}$	300	7.5
Mar. 17, 1994	B	600	7

1063-7737/03/2903-0133$24.00

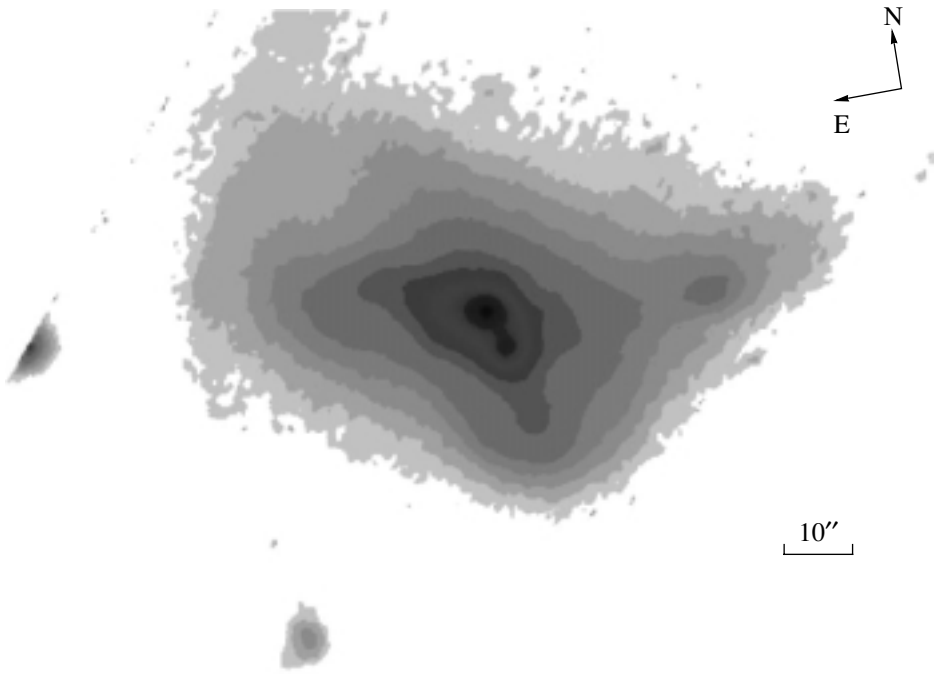

Fig. 1. UGC 4892: the processed CCD frame obtained in the B band with the 6-m telescope.

During the night, standard stars from the lists of Landolt (1983) and Smith *et al.* (1991) were observed for the calibration and conversion to the standard photometric system (B, V, R_c).

The observations were reduced at the Astronomical Institute of St. Petersburg State University using the ESO-MIDAS software package. The mean transparency coefficients for the SAO were used to correct the magnitudes for atmospheric extinction.

The spectroscopic observations of UGC 4892 (see Table 2) were carried out at the prime focus of the 6-m SAO telescope with a long-slit spectrograph (UAGS) and a multipupil field spectrograph (MPFS). The UAGS spectrograph has the following basic parameters: the slit length is 140″, the slit width is 2″, the reciprocal dispersion is 1.2 Å pixel^{-1}, and the spectral resolution is ~3.6 Å. The radial velocities were determined from the most intense Hα emission line.

The UAGS observations were reduced by using standard ESO-MIDAS procedures. The accuracy of determining the radial velocities was estimated from the night-sky [OI] λ6300 Å line measurements to be $\pm$10 km s^{-1}.

We investigated the central region of the galaxy with the MPFS spectrograph, whose description is given on the Internet at the SAO site (http://www.sao.ru/gafan/devices/mpfs/mpfs_main.htm). The angular size of the spatial element in the micropupil raster during our observations was 1″, and the MPFS field of view was 16″ × 15″. The reciprocal dispersion in the red was 1.35 Å pixel^{-1}. The stellar Na I D absorption line, other weaker absorption lines, and the Hα and [NII] λ6583 emission lines fell within the range λ5900–7100 Å.

To construct the velocity field of the stellar component, we used a cross-correlation method modified to work with 2D spectroscopy (Moiseev 2001). HD 88547 and HD 91612 were the standard stars. The MPFS data were reduced with the software developed at the SAO. The accuracy of determining the radial velocities from absorption and emission lines is $\pm$10 and $\pm$15 km s^{-1}, respectively.

RESULTS

The Photometric Observations

Isophotes of UGC 4892 in the B, V, and R_c bands are shown in Fig. 2. The isophotal pattern is similar to that obtained previously for the PRG candidate PRC C-71 (ZGC 2315 + 03), where, as we showed, there is simply a projection of two galaxies onto one another (Karataeva *et al.* 2000). However, in the peripheral regions of UGC 4892, the galactic disk is clearly warped and the isophotal pattern becomes irregular. In addition, the second condensation (classified as a polar ring in the PRC) is more pronounced. Note the blue color of the second condensation and a brightening in the western part of the galaxy.

Table 2. Spectroscopic observational material

Date	Instrument	Exposure, s	Field, arcsec	Seeing, arcsec	Spectral range, Å	Position angle (PA), deg
May 5, 2000	UAGS	1200	2×140	3.0	6200–7000	198
May 28, 2000	UAGS	1800	2×140	1.5	6200–7000	198
Jan. 31, 2000	MPFS	1200	16×15	2.2	5900–7100	Center

Because of the isophotal twist on the periphery, the galaxy inclination to the line of sight is difficult to estimate. A rough estimate yields $i = 65°$ ($\cos i = b/a = 0.4$). Multiaperture photometry [the brightness-rise curve agrees with the curve expected for $T = -1$, although the type of the galaxy in the RC3 catalog (de Vaucouleurs *et al.* 1991) is Sab, i.e., $T = 4$] gives the following total magnitudes and color indices: $B_t = 14.64 \pm 0.1$, $(B-V)_t = 0.81 \pm 0.10$, $(V-R_c)_t = +0.54 \pm 0.10$ (RC3 gives 14.80 for B_t). The large errors are attributable to the uncertainty in extrapolating the brightness-rise curve to infinity, because the galaxy is peculiar.

Figure 3 shows the photometric scans through the brighter condensation along the major axis of the galaxy in three spectral bands. We see that the brightness decline to the west of the condensation (presumably the nucleus) is steeper than that in its eastern part. Based on the less distorted eastern part of the profile, we performed a decomposition into a bulge and a disk (for the B band, it is shown in Fig. 4).

In Table 3, we present the results that provide basic information on UGC 4892 according to RC3 and our study.

The parameters (disk scale length h and effective bulge radius R_e) for the other bands are approximately the same.

Figure 5 shows the $B-V$ color distribution along the scans that pass through the brighter condensation along the major axis of the galaxy and toward the southwestern (SW) condensation. The second condensation is appreciably bluer than the first one. Its color index is about 0.73 (0.87 for the bright condensation). It is perhaps the bluest region of the galaxy, as can be seen from Fig. 6, which shows the $B-V$ color distribution over the galaxy (the lighter, the redder). The regions to the west from the first condensation and between them are the reddest regions of the galaxy (according to Fig. 5, $B-V$ reaches 1.1 here). The region of the brightness feature in the SW part of the galaxy is blue ($B-V \sim 0.75$–0.80). The brightening in the western part of the galaxy is its bluest region ($B-V \sim 0.65$–0.73).

The Spectroscopic Observations

We took long-slit spectra only at the slit passing through the two condensations ($PA = 198°$). The radial-velocity curve constructed from emission lines (pluses in Fig. 7) qualitatively agrees with the curve published by Reshetnikov and Combes (1994) (if we assume that the scan orientation in their figure is wrong but the caption to the figure and the information in the text are correct). The radial-velocity curve is straight from $-5''$ to $+7''$; the gas recedes from the observer in the SW part and approaches the observer in the NE part. However, our inclination of this segment ($\sim$30 km s^{-1} arcsec^{-1}) is much larger than that given by Reshetnikov and Combes (8.3 km s^{-1} arcsec^{-1}). Further out, the curve becomes flatter (the points near $-19''$).

Table 3. Basic characteristics of UGC 4892

v_{abs}	7708 km s^{-1}
D	118.6 Mpc ($H_0 = 65$ km s Mpc^{-1})
Scale	0.58 kpc on $1''$
B_t	14.64 ± 0.10
$(B-V)_t$	$+0.81 \pm 0.10$
$(V-R_c)_t$	$+0.54 \pm 0.10$
Morphological type	Sbc, $T = 4$ (RC3)
Sizes	$1'.2 \times 0'.7$ (RC3)
Semimajor axis a ($\mu_B = 25.0$)	$21''$ (12.2 kpc)
PA of major axis	98°
M_B	−20.7
A_B	0.00
μ_0^B	21.73
h	$11''.92$ (6.9 kpc)
μ_e	22.53
R_e	$5''.45$ (3.2 kpc)
B/D (bulge/disk)	1.0

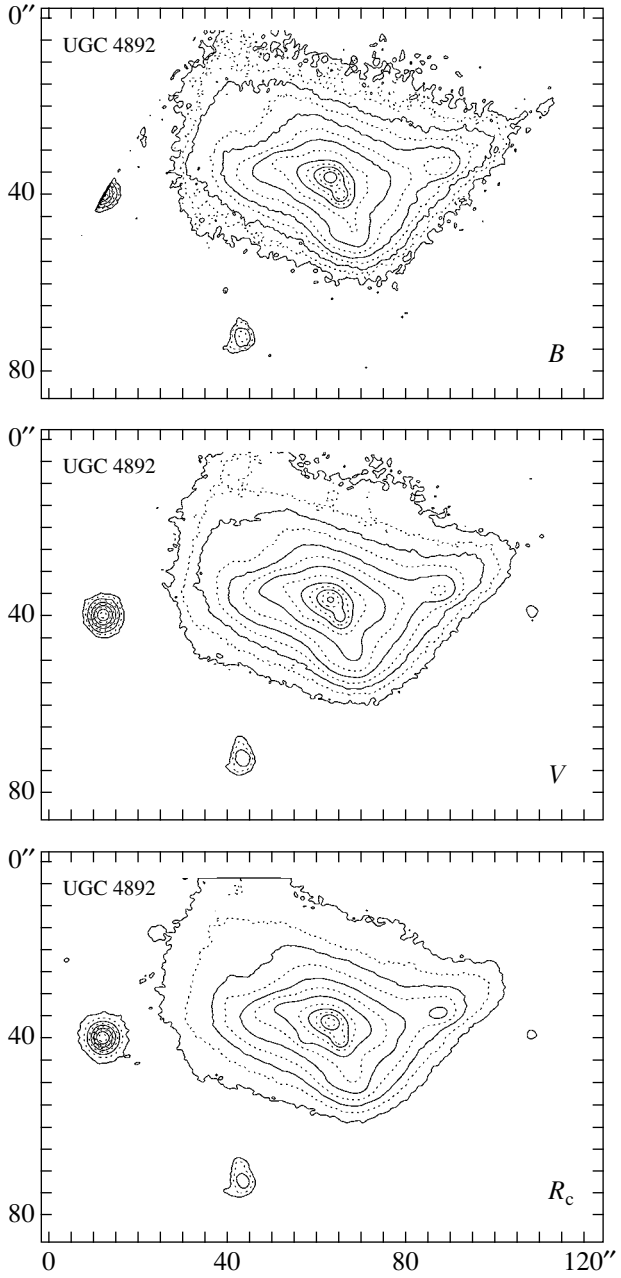

Fig. 2. Isophotes of UGC 4892 in the B, V, and R_c bands at 0.5 mag/□″ steps. The ranges in B, V, and R_c are from 20.0 to 26.0 mag/□″, from 19.0 to 25.0 mag/□″, and from 18.5 to 24.0 mag/□″, respectively.

Figure 7 shows similar data obtained with the MPFS spectrograph (*4*). The good agreement between the results obtained with two different spectrographs suggests that they are reliable, despite their disagreement with the data published by Reshetnikov and Combes (1994).

The gas and stellar velocity fields determined from the Hα emission line and the absorption lines are shown in Figs. 8a and 8b, respectively. These figures also provide information on the brightness distribution in the central part of the galaxy in Hα and in the continuum near λ6100 Å. The significant difference between the isovel patterns for the gas and stellar components and the difference between the Hα and continuum brightness distributions are immediately apparent. The gas velocity field is relatively regular and suggests the rotation of the gas masses around an axis close to the major axis of the galaxy. The isovels for the stellar component that twist at an almost right angle at a distance of about 3″ to the SW of the center point to the existence of two almost perpendicular kinematic systems.

The radial-velocity curves derived from these data for the stellar component at position angles of 198° (through the two condensations) and 82° (along the major axis of the galaxy) are shown in Fig. 7 (open and filled triangles, respectively). Note the counterrotation of the gas and stellar components in the region of the second condensation.

DISCUSSION AND CONCLUSIONS

We begin our discussion with the nature of the condensations. The central position of the NE condensation in the object and its highest brightness (see Fig. 1) suggest that it is the nucleus of the galaxy whose major axis is in the east–west direction.

As regards the second condensation, which is one of the bluest regions in UGC 4892, we could assume that this is a giant H II region. However, Figs. 8a and 8b, which exhibit no enhancement of the Hα flux (although there is a clear rise in the continuum flux), and circumstantial evidence that the linear sizes of the condensation are about 1.2 kpc at its observed angular size of about 2″, which exceeds the sizes of the brightest H II regions even in ScI galaxies [about 700 pc, as estimated by Sandage and Tamman (1974)], are in conflict with this assumption. Therefore, we assume, as was done by Vorontsov-Velyaminov (1977), that the SW condensation is the nucleus of a galaxy (we will call it a companion galaxy) interacting with a galaxy elongated in the east–west direction (we will call it the main galaxy). The fact that the galaxy is double is also suggested by the kinematics of the stellar component. The similarity between the radial velocities of the two galaxies, the irregular isophotal pattern, and the peculiar velocity field rule out the possibility that this is a chance projection of two galaxies onto one another.

The data in Table 3 largely refer to the main galaxy. Its size (72″ or 42 kpc), luminosity $M_B = -20^m.7$ [a correction for the internal extinction, which can be about $0^m.6$ as follows from the formulas of Boselli and Gavazzi (1994), would further increase this luminosity; however, an allowance for the contribution of

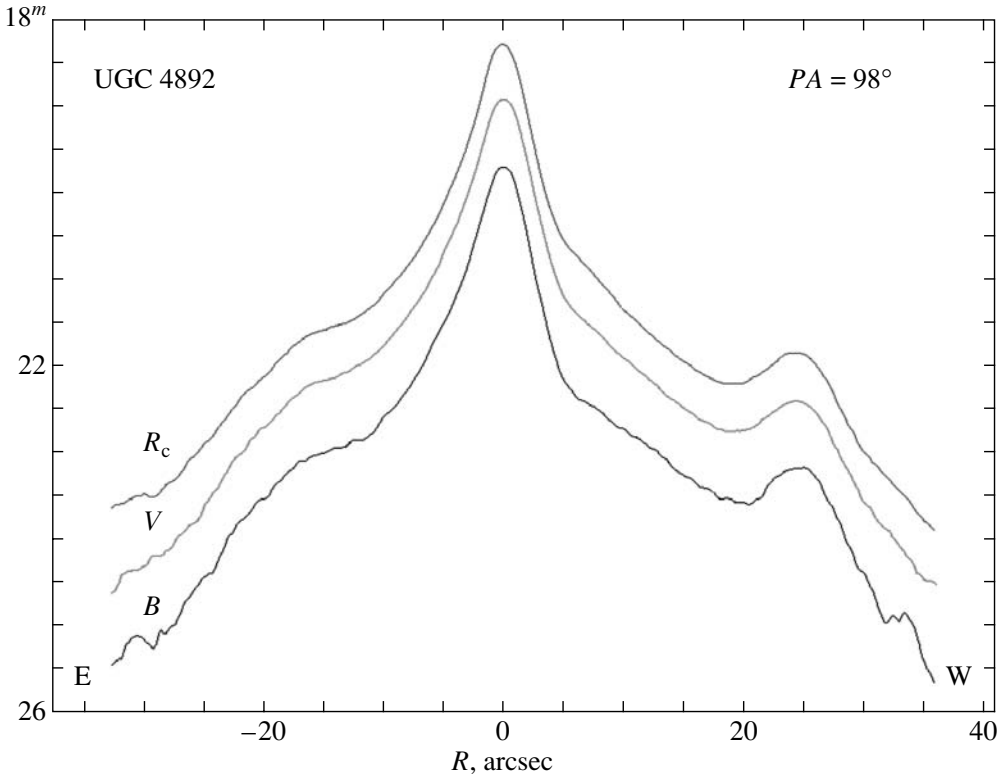

Fig. 3. Photometric scans along the major axis of the galaxy.

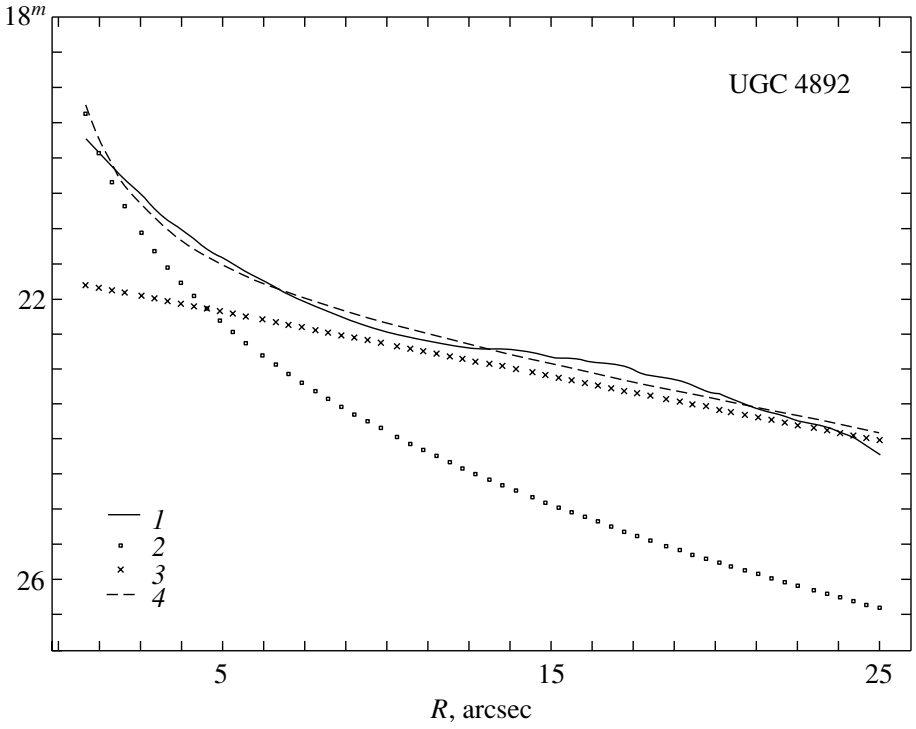

Fig. 4. Decomposition of the observed B-band brightness profile along the major axis to the east from the nucleus (*1*) into a bulge (*2*) and a disk (*3*); a bulge + a disk is denoted by (*4*).

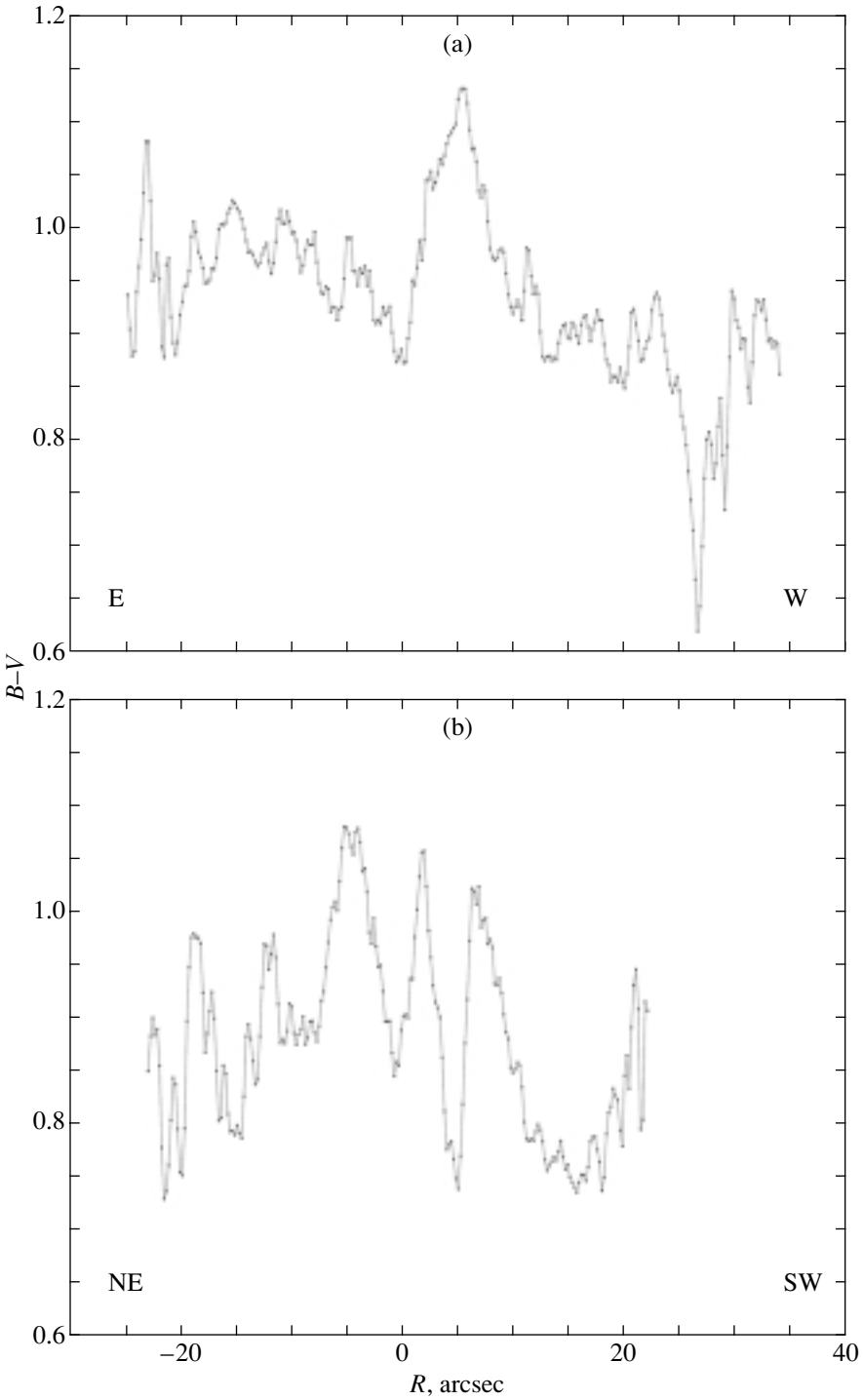

Fig. 5. Color scans through the NE condensation: (a) along the major axis and (b) through the SW condensation.

the companion galaxy would give approximately the same correction but with the opposite sign], and the mass of the central region $\sim 1.7 \times 10^{10} M_\odot$ within 8″ (4.6 kpc), which can be estimated from the radial-velocity curve at a position angle of 82° (Fig. 7) by taking into account the galaxy inclination, suggest that this is a giant galaxy. Its influence on the companion galaxy must be strong.

We begin our discussion of the complex kinematics in UGC 4892 with an examination of Figs. 7 and 8b. The isovel pattern and the radial-velocity curve for the stellar component suggest that the main galaxy rotates around its minor axis; the western part

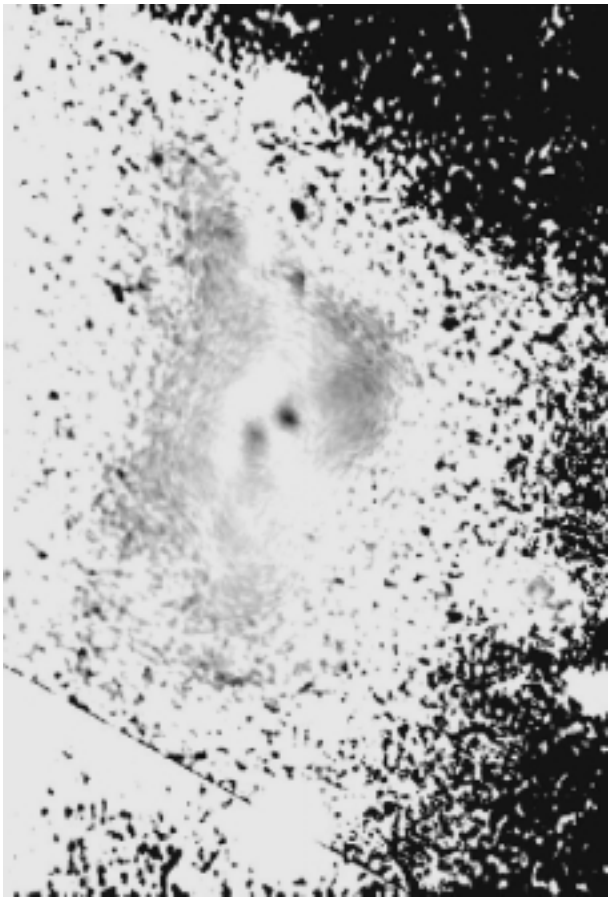

Fig. 6. The $B-V$ color distribution in UGC 4892 (the lighter, the redder); the color index ranges from $0^m.6$ to $1^m.1$.

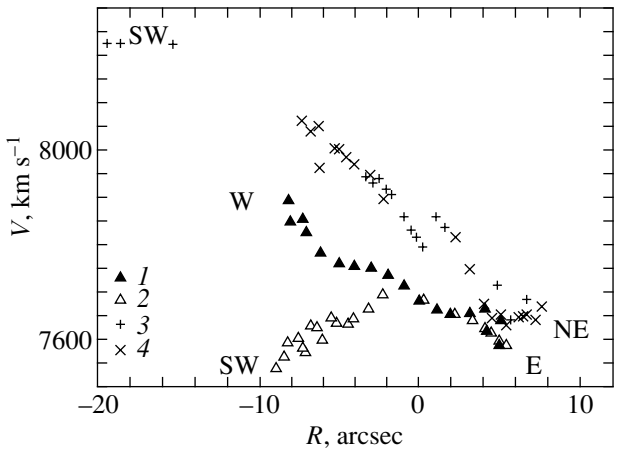

Fig. 7. The radial-velocity curves ($R = 0$ in the NE condensation); the different symbols denote the following: (*1*) the stellar component at $PA = 82°$; (*2*) the stellar component at $PA = 198°$ (the coordinates of the SW condensation $R = -5$); and (*3* and *4*) the gas component at $PA = 198°$ for the UAGS and MPFS data.

of the galaxy recedes from the observer, while its eastern part approaches the observer. The velocities at a distance of $8''$ are about ± 100 km s^{-1}, which gives the above mass estimate for the central part of the galaxy. The radial velocity for the nuclear region of the galaxy is $v_{\rm Hel} = 7685$ km s^{-1}. The velocity determined from the gas component is larger by approximately 100 km s^{-1}, i.e., 7785 km s^{-1} (the same value can also be obtained from the velocity curve in Fig. 7). This value is more than 200 km s^{-1} lower than the value published by Reshetnikov and Combes (1994) but is in excellent agreement with the value derived from the H I data by Van Driel *et al.* (2000), who give $v_{\rm Hel}^{\rm H\,I} = 7778$ km s^{-1}. (Note that differences of the order of 100 km s^{-1} between the radial velocities determined from stars and gas are commonly observed for PRGs (see, e.g., the review of Richter *et al.* 1994).)

An examination of Figs. 7 and 8a points to a large-scale rotation of the gas masses around an axis close to the major axis of the main galaxy and to a direction perpendicular to the direction of the feature. Clearly, this gas could not initially belong to the main galaxy but was captured by the latter [unless it belongs to the companion galaxy; however, the Hα flux distribution (Fig. 8a) and the counterrotation of the stellar component of the companion galaxy and of the gas masses provide evidence against this suggestion]. Since the companion galaxy is in the immediate proximity of the main galaxy, it would be natural to assume that this is the gas that was lost by it through its interaction with the main galaxy. The sense of gas rotation then reflects either the direction of the orbital motion of the companion galaxy (if the galaxies constitute a physical pair) or the direction of its passage. As calculations show, gaseous streams or even rings can be formed during such an interaction (see, e.g., Sotnikova 1996).

Note yet another important circumstance. An examination of Fig. 7 indicates that, for the stellar component, the radial velocity of the nucleus of the companion galaxy is lower (by 50 km s^{-1} if the dynamical centers of the galaxies are assumed to be close to their optical centers) than the corresponding velocity of the main galaxy. For the direction of orbital motion established above from gas rotation, this rules out the possibility of the galaxies being (if they constitute a physical pair) in circular orbits.

The hypothesis that a gaseous stream (ring) is formed through the chance passage of the companion galaxy near the main galaxy should probably also be abandoned. During a chance passage, the radial velocity of the companion galaxy can, of course, be lower than that of the main galaxy. Obviously (since the gaseous stream has already been formed), the companion galaxy for the observed direction of gas

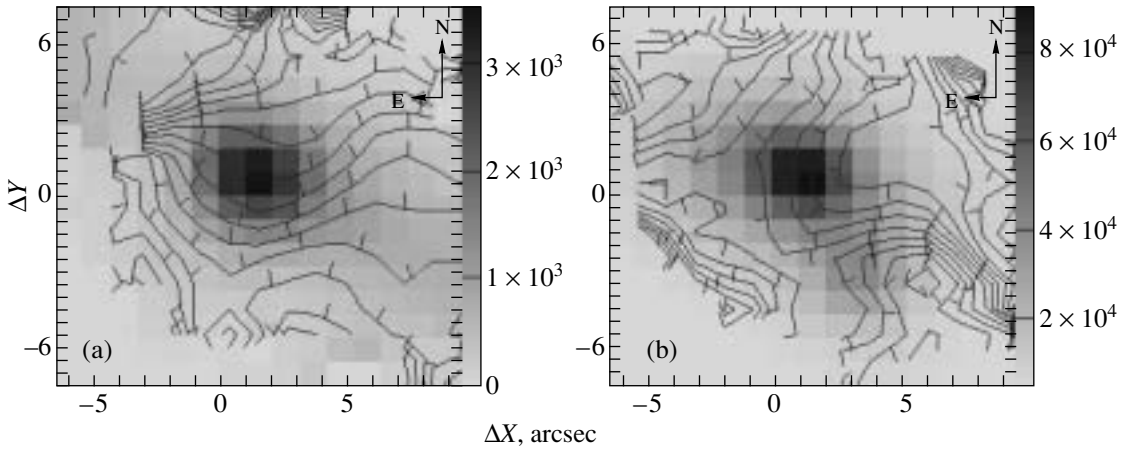

Fig. 8. The velocity fields determined from (a) the Hα line and (b) absorption lines and the brightness distribution in Hα (a) and in the continuum near λ6100 Å (b). The isovels are drawn at steps of (a) 30 and (b) 20 km s^{-1}. The velocities at point (0, 0) are (a) 7830 and (b) 7710 km s^{-1}. The coordinated of the nucleus of the main galaxy are $\Delta X = 1.5$ and $\Delta Y = 1.5$.

motion must be closer to the observer and must recede (in the plane of the sky) from the main galaxy. However, the rotating gas is observed in the SW direction much farther (at least up to 19″, according to Fig. 7) than the nucleus of the companion galaxy, and it is unclear how it could overtake the galaxy in its motion.

The observational facts can probably be explained if the galaxies are assumed to actually constitute a physical pair, with the companion galaxy moving in a highly elongated elliptical orbit whose pericenter lies to the NE of the nucleus of the main galaxy. In this case, irrespective of whether the companion galaxy is closer to (i.e., recedes from the pericenter) or farther from the observer, this galaxy will exhibit a negative radial velocity relative to the main galaxy. The large extent of the gaseous structure should be explained by the fact that the companion galaxy has already made more than one turn around the main galaxy.

Our model can account for several more observational facts. In this model, the pericenter of the orbit of the companion galaxy is near the eastern part of the main galaxy. According to our measurements, the emission in the forbidden [N*II*] λ6583 line 3″–4″ to the east from the nucleus of the main galaxy is enhanced compared to that in other regions of the main galaxy. The [N*II*]/Hα intensity ratio here is 2.0, whereas its value at the center and in the western part is about 1.0. An additional collisional excitation of gas emission through the interaction between the gas masses of the two galaxies may take place here. The difference between the radial velocities for the stars and gas in the nucleus of the main galaxy probably also results from this interaction (Fig. 7).

The decomposition of the brightness profile for the main galaxy into a bulge and a disk reveals no significant anomalies. The disk parameters and the bulge-to-disk (B/D) luminosity ratio does not differ significantly from their means for early-type spirals.

UGC 4892 is not a strong infrared source (it was not included in the IRAS catalog). Nevertheless, the presence of dust in the galaxy is beyond doubt. It is clearly seen in Figs. 5 and 6. However, according to Fig. 5, the color excess in the regions that enclose the nucleus from the south, west, and north is only $E_{B-V} = 0.2$. Thus, the visual absorption in these regions does not exceed $A_V \sim 0^m.7$.

As regards the extended blue region in the SW, this can be assumed to be the result of a partial destruction of the companion galaxy, which was initially either a late-type spiral or a blue irregular galaxy. The hot stars of this galaxy remnant may be involved in the excitation of stream gas emission in Hα. In addition, star formation can also take place in the stream gas.

In conclusion, note that although the existence of two almost orthogonal kinematic systems in UGC 4892 is beyond doubt, the picture differs greatly from that for classical PRGs. The available observational data and theoretical information are not enough to ascertain whether a polar ring will be formed in the system or the gas will gradually settle on the main galaxy. A further study of UGC 4892 is undoubtedly of great interest. In particular, we plan to perform its observations with a Fabry–Perot interferometer to study the kinematics in the far peripheral regions of the object.

ACKNOWLEDGMENTS

We wish to thank the Committee on the Subject of Large Telescopes for allocating time on the 6-m SAO telescope. We are also grateful to A.N. Burenkov

and A.V. Moiseev, the responsible observers on the UAGS and MPFS spectrographs, for carrying out the observations and for help in reducing the observational data. This study was supported by the Russian Foundation for Basic Research (project no. 02-02-16033) and the Federal Program "Astronomy" (project no. 40.022.1.1.1001).

REFERENCES

1. A. Boselli and G. Gavazzi, Astron. Astrophys. **283**, 12 (1994).
2. W. van Driel, M. Arnaboldi, F. Combes, and L. S. Sparke, Astron. Astrophys., Suppl. Ser. **141**, 385 (2000).
3. G. M. Karataeva, V. A. Hagen-Thorn, and V. A. Yakovleva, Pis'ma Astron. Zh. **26**, 883 (2000) [Astron. Lett. **26**, 757 (2000)].
4. A. U. Landolt, Astron. J. **88**, 439 (1983).
5. A. V. Moiseev, Bull. SAO **51**, 11 (2001).
6. V. P. Reshetnikov and F. Combes, Astron. Astrophys. **291**, 57 (1994).
7. O. R. Richter, P. D. Sackett, and L. S. Sparke, Astron. J. **107**, 99 (1994).
8. A. R. Sandage and G. A. Tamman, Astrophys. J. **190**, 525 (1974).
9. R. S. Smith, B. J. Jannuzi, and R. Elston, Astrophys. J., Suppl. Ser. **77**, 67 (1991).
10. N. Ya. Sotnikova, Astrofizika **39**, 259 (1996).
11. G. de Vaucouleurs, A. de Vaucouleurs, J. R. Corwin, *et al.*, *Third Reference Catalog of Bright Galaxies* (Springer-Verlag, Berlin, 1991).
12. B. A. Vorontsov-Velyaminov, Astron. Astrophys., Suppl. Ser. **28**, 1 (1977).
13. B. C. Whitmore, R. A. Lucas, D. B. McElroy, *et al.*, Astron. J. **100**, 1489 (1990).

Translated by V. Astakhov

Astronomy Letters, Vol. 29, No. 3, 2003, pp. 142–152. Translated from Pis'ma v Astronomicheskiĭ Zhurnal, Vol. 29, No. 3, 2003, pp. 172–183.

Study of the Anisotropy of Cosmic Rays with $E_0 \geq 5 \times 10^{16}$ eV Using Yakutsk EAS Array Data

A. V. Glushkov*

Institute of Cosmophysical Research and Aeronomy, Siberian Division, Russian Academy of Sciences, pr. Lenina 31, Yakutsk, 677007 Russia

Received October 11, 2002

Abstract—We present the results of a harmonic analysis of and search for clusters in the arrival directions of cosmic rays with energies $E_0 \geq 5 \times 10^{16}$ eV and zenith angles $\theta \leq 53°$ detected at the Yakutsk extensive air shower (EAS) array from 1974 to 2002. We show that the phase of the first harmonic periodically varies greatly and takes on nonrandom values at a confidence level $\geq 4\sigma$. These phases point to the Supergalactic plane (the Local supercluster of galaxies). © *2003 MAIK "Nauka/Interperiodica"*.

Key words: *extensive air showers, cosmic-ray anisotropy.*

1. INTRODUCTION

Studying anisotropy and its dependence on the energy E_0 of primary cosmic rays (PCRs) is of considerable importance in solving the problem of the origin of cosmic rays. The ultrahigh-energy ($E_0 \geq 10^{15}$ eV) PCRs are investigated by using extensive air showers (EASs). One of the main methods for estimating the anisotropy of the global PCR flux is a harmonic analysis of the distribution of shower arrival directions in right ascension (Linsley 1975).

The experimental results obtained before 1991 with various world arrays were summarized by Linsley and Watson (1981), Lloyd-Evans and Watson (1983), Glushkov (1988), and Watson (1992). The pattern proved to be in many ways unstable and contradictory. The data considered by these authors did not allow the statistically significant amplitudes of the first harmonic to be distinguished with confidence. However, the phases of the first harmonic were often close in magnitude. Their average dependence on the PCR energy is indicated by the dashed line in Fig. 1. The statistically significant anisotropy found by Coy *et al.* (1981) with the Haver Park array at $E_0 \approx 10^{17}$ eV was initially confirmed by Mikhailov and Pravdin (1997) with the Yakutsk array but was subsequently refuted by Pravdin *et al.* (2001a, 2001b). The Yakutsk team used a broader energy range ($3 \times 10^{16} < E_0 < 3 \times 10^{17}$ eV), which, in the opinion of Pravdin *et al.* (2001a, 2001b), maximally increased the number of showers without anisotropy distortion.

We present new experimental results, which show a significant dependence of the ultrahigh-energy PCR anisotropy on the choice of energy ranges. Disregarding this circumstance can lead to contradictory results and wrong conclusions.

METHOD OF SELECTION AND DATA ANALYSIS

Below, we consider EASs with energies $E_0 \geq 5 \times 10^{16}$ eV and zenith angles $\theta \leq 53°$ detected by the Yakutsk array from 1974 to 2002. We selected only those showers whose arrival directions were determined at ≥ 4 stations and whose axes were within

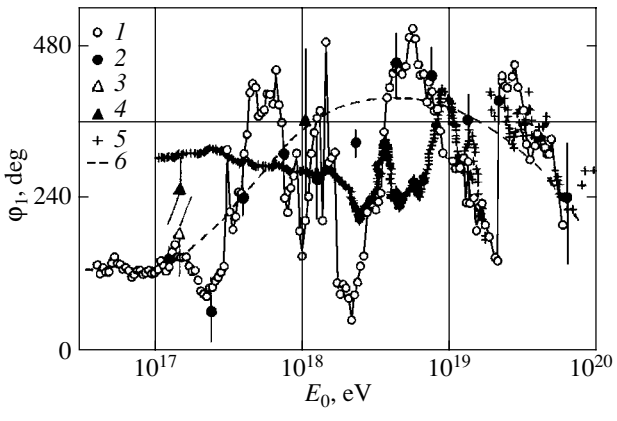

Fig. 1. The phase of the first harmonic versus the PCR energy, as constructed from the Yakutsk EAS data: *1*, our results; *2*, *3*, *4*, the data from Afanasiev *et al.* (1995) and Pravdin *et al.* (2001a, 2001b), respectively; *5*, the AGASA data (Hayashida *et al.* 1999); and *6*, the behavior of the phase φ_1 averaged over the world data from the review of Glushkov (1988).

*E-mail: a.v.glushkov@ikfia.ysn.ru

the array central circle of radius $R \leq 1000$ m. At $E_0 \geq 10^{19}$ eV, we took events with $\theta \leq 60^\circ$ and $R \leq 1700$ m. These give small errors when determining basic EAS parameters (the axis direction and coordinates, E_0, etc.). The primary particle energy E_0 was calculated from the relations

$$E_0 = (4.8 \pm 1.6) \times 10^{17} (\rho_{s,600}(0^\circ))^{1.0\pm0.02} \text{ [eV]}, \quad (1)$$

$$\rho_{s,600}(0^\circ) = \rho_{s,600}(\theta) \times \exp((\sec\theta - 1)1020/\lambda_\rho) \text{ [m}^{-2}\text{]}, \quad (2)$$

$$\lambda_\rho = (450 \pm 44) + (32 \pm 15)\log(\rho_{s,600}(0^\circ)) \text{ [g cm}^{-2}\text{]}, \quad (3)$$

where $\rho_{s,600}(\theta)$ is the charged-particle density measured with ground-based scintillation detectors at the distance $R = 600$ m from the shower axis. A total of 105 012 showers were selected in this way.

We used the standard method of harmonic analysis in equatorial coordinates (Linsley 1975) and studied the behavior of the first harmonic. The sky region surveyed by the Yakutsk array was divided into $n = 24$ identical sectors (at $\Delta\alpha = 15^\circ$ steps in right ascension). The essence of the harmonic analysis is to choose the best amplitude A_1 and phase φ_1 of the function

$$f(\alpha) = f_0 + A_1\cos(\alpha - \varphi_1) \quad (4)$$

by minimizing the quantity

$$X^2 = \sum_{i=1}^{n} (f_i - N_i)^2/N_i, \quad (5)$$

where N_i is the number of showers in the ith spherical sector $\Delta\alpha_i$; $f_0 = (\sum_{i=1}^{n} N_i)/n$.

We studied the anisotropy in $h = \Delta \log E_0 = 0.2$ bins by sequentially shifting them in energy by $0.1h$. This was done to analyze the behavior of the phase φ_1 of the first harmonic in more detail, because Linsley and Watson (1981), Lloyd-Evans and Watson (1983), Glushkov (1988), and Watson (1992) provided evidence of its rapid variations at certain E_0. We believe (Glushkov 1988) that these are not random but reflect the actual pattern of PCR propagation in space.

THE PHASE OF THE FIRST HARMONIC

The amplitude of the first harmonic A_1 is a measure of the global PCR anisotropy. If it is significantly ($>3\sigma$) larger than the amplitude of the corresponding isotropic flux, then the phase φ_1 in this case is assumed to reflect the actual anisotropy. First, we analyze the behavior of the phase of the first harmonic irrespective of its amplitude. The variations of A_1 with E_0 are considered below.

The dependence of φ_1 on the mean bin energy is indicated by the open circles in Fig. 1. We see that the phases of the first harmonic at certain energies have stable and close values. These values periodically vary greatly about the dashed line (taken from the review of Glushkov 1988), which characterizes the behavior of φ_1 averaged over the world data. The filled circles represent the data previously obtained by Afanasiev *et al.* (1995) at the Yakutsk array when the entire energy range was divided into 11 bins at $h = 0.25$ steps. These are in agreement with our data. The open and filled triangles represent, respectively, the results obtained by Pravdin *et al.* (2001a, 2001b) at the Yakutsk array when the showers were divided in energy into bins at $h \approx 1$ steps (in the ranges $3 \times 10^{16} < E_0 < 3 \times 10^{17}$ eV and $3 \times 10^{17} < E_0 < 3 \times 10^{18}$ eV). Here, despite the significant increase in the number of events in the bins, the phases φ_1 were determined with large errors, although, in general, these are consistent with the general pattern of the data shown in Fig. 1. In our view, this occurred because the bins within which events with opposite PCR arrival directions fell were unjustifiably broad. Unstable phases of the first harmonic that strongly depended on the bin locations on the energy axis arose. The energy dependence of φ_1 obtained by Hayashida *et al.* (1999) with AGASA (Akeno Giant Air Shower Array) from the analysis of 114 000 showers with zenith angles $\theta \leq 60^\circ$ is indicated by the crosses in Fig. 1. Before we compare the results of the two arrays, we note that they reflect different parts of the sky. This is clearly seen from Fig. 2, where the open region around the Earth's North pole indicates the sky zone surveyed by the Yakutsk array (in Galactic coordinates) at $\cos\theta \geq 0.6$, and the hatched region indicates the additional part of the sky viewed by AGASA at $\cos\theta \geq 0.5$. The circles in Fig. 2 show the magnetic fields in the Galaxy (Lyne and Graham-Smith 1990). The open and filled circles indicate the field orientations toward and away from the observer, respectively. The field strength is proportional to the circle diameter. The map was constructed in such a way that equal areas in the figure corresponded to sky regions of equal area.

The AGASA data in Fig. 1 also exhibit a certain pattern in the behavior of φ_1 with its local variations, although Hayashida *et al.* (1999) paid no attention to this pattern. They only pointed out that, at $8 \times 10^{17} < E_0 < 2 \times 10^{18}$ eV, there is a significant (at a random probability level $\sim$0.002) excess of the amplitude $A_1 \approx 0.04$ above its random value for the isotropic flux. The phase $\varphi_1 \approx 295^\circ$ of this amplitude (arrow *1* in Fig. 2) corresponds to the direction of the exit from the Orion arm at a Galactic longitude $l_G \approx 50^\circ$. However, Hayashida *et al.* (1999) associated this

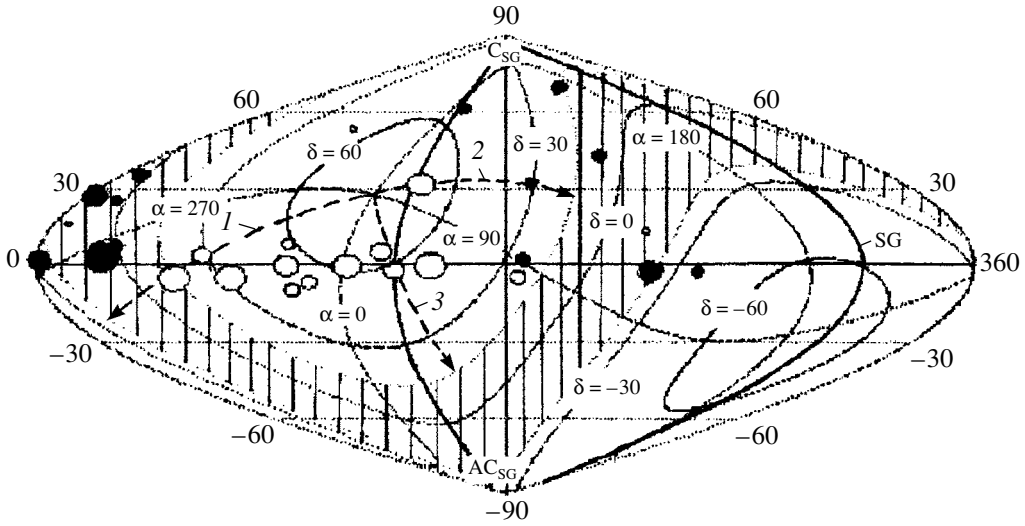

Fig. 2. The sky zones in Galactic coordinates surveyed by the Yakutsk array ($\delta \approx 15°-90°$) and AGASA ($\delta \approx -25°$ to $-90°$); the filled and open circles indicate the locations of the Galactic magnetic arms (Lyne and Graham-Smith 1990) with the directions away from and toward the observer, respectively. The circle diameters are proportional to the field strength. The dashed arrows *1*, *2*, and *3* indicate the phases of the first harmonics for showers with $E_0 \approx 10^{17.9-18.3}$ eV as obtained with AGASA (Hayashida *et al.* 1999) and the Yakutsk array, $\varphi_1 \approx 125°$ at $E_0 < 10^{17.5}$ eV and $\varphi_1 \approx 40°$ at $E_0 \approx 10^{17.7-17.8}$ eV, respectively; α and δ are the right ascension and declination (equatorial coordinates); and SG, C_{SG}, and AC_{SG} are the Supergalactic disk, center, and anticenter, respectively.

phase with the Galactic center, from where, according to their data, an excess PCR flux is observed. Unfortunately, the Yakutsk array does not see the Galactic center.

At first glance, the Yakutsk and AGASA data are in poor agreement. However, this is not the case. In the region with $E_0 \geq 8 \times 10^{18}$ eV, the two arrays show approximately the same E_0 dependence of φ_1. At lower energies, the difference probably stems from the fact that each AGASA data point in Fig. 1 corresponds to the anisotropy for the total PCR flux with energy above the specified value. Under these conditions, the peaks and dips are strongly smoothed out. If we take into account this circumstance, as well as the differences between the energy estimates obtained with the two arrays by a factor of ~1.4 (Glushkov *et al.* 2002) and their different geographic positions (AGASA lies 27° to the south and surveys a much larger region of the sky), then a certain correlation can be said to exist between the data under consideration.

Let us analyze in more detail the peaks and dips in Fig. 1 for the randomness of their occurrence.

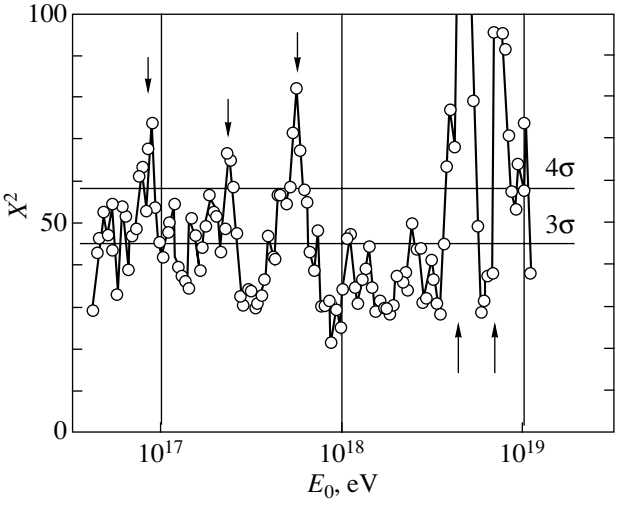

Fig. 3. Comparison of the X^2 values calculated using formula (5) with the tabulated χ^2_{1-p} values for two confidence probabilities, $\beta = 1 - p = 0.998$ (lower 3σ straight line) and $\beta = 0.99996$ (upper 4σ straight line). The arrows indicate the most significant values.

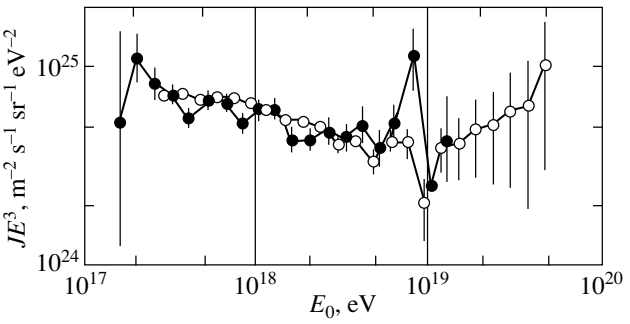

Fig. 4. The differential cosmic-ray energy spectrum measured with the Yakutsk array by Pravdin *et al.* (1999) and with the HiRes-2 array by Sommers (2001).

Consider the hypothesis of an isotropic shower distribution in $n = 24$ angular spherical sectors. We use the values of (5) whose distribution corresponds to the χ^2 distribution with $(n-3)$ degrees of freedom. At $X^2 > \chi^2_{1-p}$, where χ^2_{1-p} is the tabulated χ^2 value that corresponds to a given significance level p, this hypothesis can be rejected with the confidence probability $\beta = 1 - p$.

In Fig. 3, the X^2 values (for the phases φ_1) shown in Fig. 1) are plotted against the mean bin energy. Comparison of the calculated X^2 values and the tabulated χ^2_{1-p} values allows us to reject the hypothesis that the peaks and dips in Fig. 1 occur randomly. Some of these (marked by the arrows in Fig. 3) have a confidence level $\geq 4\sigma$ (with a confidence probability $\beta \geq 0.99996$). Thus, at the above energies, there is a strong local anisotropy that periodically weakens almost to an isotropic distribution of PCR arrival directions.

Note some important features of our results. At $E_0 < 3 \times 10^{17}$ eV, the phases were concentrated near $\varphi_1 \approx 125^\circ$. This direction lies outside the random direction at a confidence level $\geq 3\sigma$ (Fig. 3). It is in no way associated with the Galactic plane, from which one might seemingly expect anisotropy of the charged PCR particle flux in the diffusion model of their propagation. This direction points to the exit of one of the midlatitude Galactic magnetic arms or, possibly, even to the Supergalactic plane (arrow *2* in Fig. 2). The phase dip in Fig. 1 at $E_0 \approx 10^{17.3-17.4}$ eV ($\varphi_1 \approx 90^\circ$) also points to the Supergalactic plane (Fig. 2). Glushkov and Pravdin (2002) showed that some of the PCRs at such energies form a set of clusters that correlate with extragalactic sources.

Yet another significant peak is located at energies $E_0 \approx 10^{17.6-17.9}$ eV (Fig. 3). The phase $\varphi_1 \approx 40^\circ$ in Fig. 1 points to the line of intersection of the Galactic and Supergalactic planes (arrow *3* in Fig. 2). The two planes are almost perpendicular in space.

The phase dip in Fig. 1 at energies $E_0 \approx 10^{18.25-18.45}$ eV shows up in the data of both arrays. Undoubtedly, it has to become the subject of a special study to be carried out. For now, we can note once again that the phase $\varphi_1 \approx 90^\circ$ obtained with the Yakutsk array points to the Supergalactic plane.

Finally, note the energies $E_0 \approx 10^{18.6-18.9}$ eV at which the PCR flux changes its global direction, possibly, twice (the arrows in Fig. 3): from $\varphi_1 \approx 90^\circ$ at $E_0 \approx 10^{18.6-18.7}$ and $E_0 \approx 10^{18.8-18.9}$ eV to $\varphi_1 \approx 150^\circ$ at $E_0 \approx 10^{18.7-18.8}$ eV. These peaks are particularly significant in Fig. 3. They correlate with the peak in the differential energy spectrum measured by Pravdin *et al.* (1999) and, with the HiRes-2 array, by Sommers (2001). The two spectra are shown in Fig. 4. The Yakutsk array spectrum from Pravdin *et al.* (1999) includes the showers with zenith angles $\theta \leq 45^\circ$ that were selected only by the master triangles with 500-m separations between the stations. The spectrum taken from Sommers (1999) was normalized by increasing the energy by a factor of 1.4, because it was underestimated with the HiRes-2 array by this factor compared with our value. These peaks in Fig. 4 show up in both cases at a confidence level $\geq 3\sigma$. Note that at $E_0 \geq 5 \times 10^{18}$ eV, the PCR arrival directions correlate with the Supergalactic plane with a $(4-5)\sigma$ excess above the isotropic flux (Glushkov and Pravdin 2001a, 2001b).

SMALL-SCALE PCR ANISOTROPY

We see from the above discussion that at some E_0, there are phases of the first harmonic that do not rule out extragalactic PCR anisotropy. As an example, let us consider in more detail the showers with $E_0 \approx 10^{17.7-17.8}$ eV that form the statistically significant peak in Fig 3. We study the small-scale anisotropy, i.e., local PCR nonuniformities $\sim 5^\circ - 10^\circ$. We take only those EASs whose arrival directions were determined at ≥ 5 stations and whose axes still fell within the array central circle of radius $R \leq 1000$ m.

A total of 7426 showers were selected in this way. As was done previously (Glushkov and Pravdin 2002), we took seven independent samples with approximately the same number of events, ≈ 1000. These differ only in that the axes for them fell into different annular areas within the central circle of the array. Each of the seven samples was separately analyzed for the presence of local groups of showers on the sky. This was done in the same way as previously (Gluskov and Pravding 2001b). All neighbors were located around the arrival direction of any shower at an angular distance of $d \leq 3^\circ$. If ≥ 3 showers were within the circle, then their coordinates were averaged and subsequently used as new points (we call them nodes).

Next, the nodes were separately analyzed for the intersection $m \geq 2$ times in any of the seven samples, provided that their centers were at $d \leq 3^\circ$. If such nodes were found, then the arrival directions of all of the showers included in them were again averaged and this larger node (we call it a cluster) was taken for the subsequent analysis.

Figure 5 shows a map of the nodes (dots) and clusters with $m = 2$ (crosses) and $m \geq 3$ (filled circles) nodes that include a total of 1812 showers from the seven samples mentioned above on a developed celestial sphere in Galactic coordinates. For convenience, the equatorial coordinates are also shown in this map.

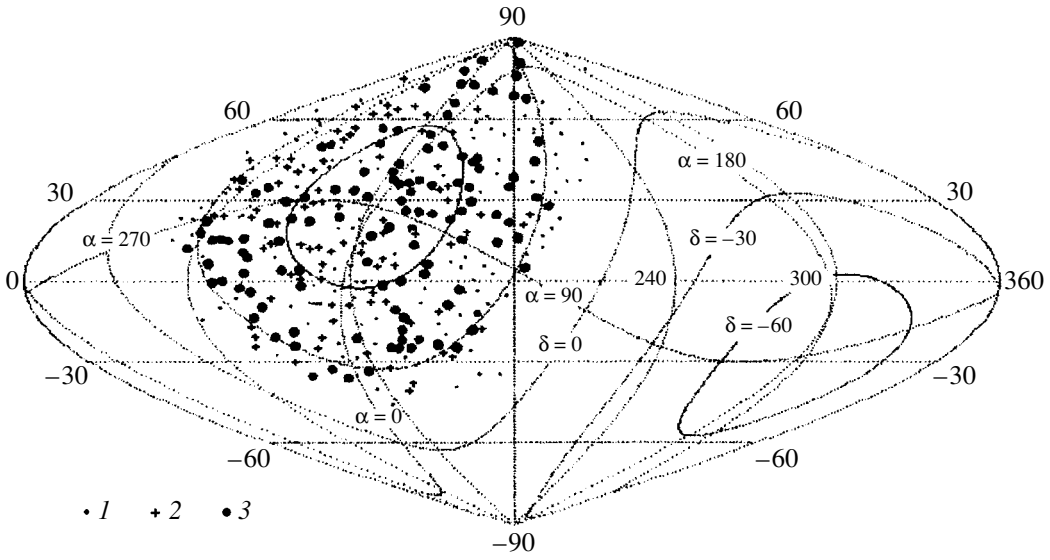

Fig. 5. The map of the nodes, *1*, and clusters of 1812 showers with $E_0 = 10^{17.7-17.8}$ eV and $\theta \leq 53^\circ$ in Galactic coordinates, as constructed from the Yakutsk EAS data: *2* and *3* are clusters of $m = 2$ and $m \geq 3$ nodes with $d \leq 3^\circ$, respectively.

Here, we clearly see the small-scale anisotropy with a large number of dense groups and chains. Monte Carlo drawing indicated that the cluster locations in Fig. 5 are not random in nature. Figure 6a shows the arrival latitude distributions of node showers in Galactic (G) and Supergalactic (SG) coordinates (at $\Delta b = 3^\circ$ steps). The upper panels (*1*) show the observed ($N_{\rm exp}$) and expected ($N_{\rm ran}$) distributions; the lower panels (*2*) show the deviations of the number of measured events from the expected number in units of the standard $\sigma = \sqrt{N_{\rm ran}}$; $n_\sigma = (N_{\rm exp} - N_{\rm ran})/\sigma$. The smooth curves in Fig. 6a (*2*) correspond to the average behavior of n_σ when smoothed by a Fourier series with five harmonics.

The values of $N_{\rm ran}$ were determined by drawing the number of showers under consideration randomly distributed over the celestial sphere. This was done as follows. For each measured shower, we found 500 directions in Galactic coordinates by substituting random arrival times and azimuths for their actual values (in horizontal coordinates of the array). The distributions of random events obtained in this way were then normalized in absolute value to the actual distributions.

Here, we have large χ^2 values, $\approx$110–150, for $n = 50$ degrees of freedom in both coordinate systems. The probability of such random outcomes is $<10^{-5}$. A statistically significant ($\approx 5\sigma$), large excess of events is observed in the Supergalactic plane. By contrast, the Galactic plane manifests itself (Fig. 6a *2*(G)) only as a small dip, which is more pronounced against the background of the distribution segments that adjoin it on both sides. Note that a similar, but more significant dip ($\approx 9.2\sigma$) in the Galactic disk is also observed at energies $E_0 \approx 10^{17.1-17.6}$ eV (Glushkov and Pravdin 2002).

These results can be interpreted as evidence that the part of the PCR contained in the clusters is extragalactic in origin. The Galaxy appears to only absorb this radiation, with the absorption being stronger in the disk. The other significant peaks and dips in Fig. 6a most likely suggest a complex and nonuniform structure of the space where the PCR sources that form the clusters are located.

Similar distributions for the rest of the showers that were not included in the above clusters (5614 events) are shown in Fig. 6b. We see that the pattern here changed sharply. The measured and expected distributions for the random values are similar ($\chi^2 = 47$–59). This result strongly suggests that the part of the PCR separated in this way is highly isotropic. The fraction of these particles in the total flux is $5614/7426 \approx 0.75$.

Since the Galactic plane is almost perpendicular to the Supergalactic plane (see Fig. 2), we can refine some of the features in Fig. 6. The arrival longitude distributions of the showers in the nodes and clusters from the Galactic and Supergalactic disks ($|b| \leq 2^\circ$) for events with $E_0 = 10^{17.7-17.8}$ eV are shown in Fig. 7a (at $\Delta l = 3^\circ$ steps). The Supergalactic longitude was measured counterclockwise from the anticenter.

Multiple peaks and dips at $\geq 2\sigma$ are observed in the surveyed sectors of the two disks ($l \approx 30^\circ$–210°). The values of $\chi^2 \approx 93$–96 for $n = 50$ degrees of freedom correspond to the probabilities of such random

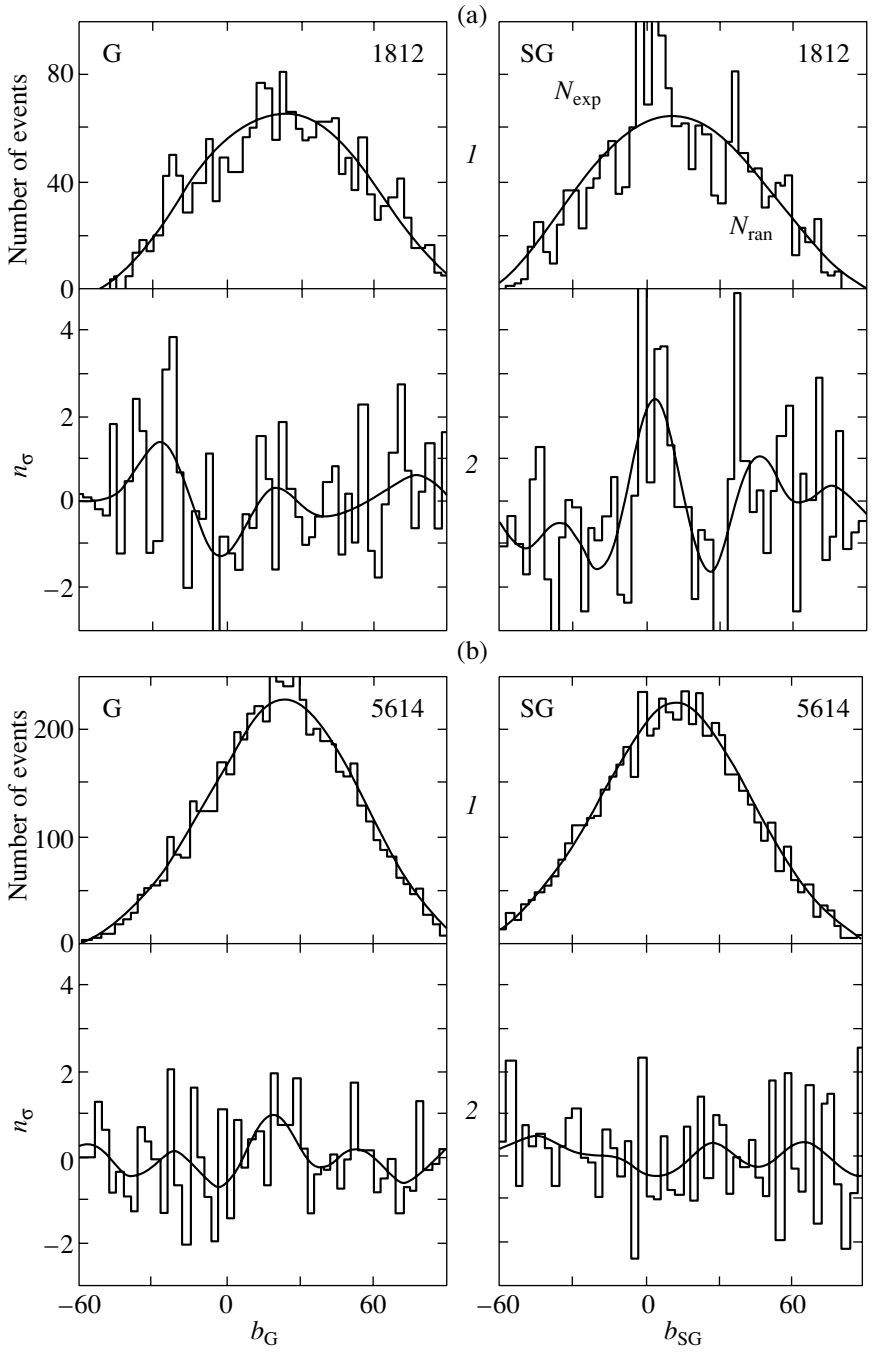

Fig. 6. Histograms *1*—the arrival latitude distributions of showers with $E_0 = 10^{17.7-17.8}$ eV in Galactic (G) and Supergalactic (SG) coordinates: (a) at nodes of seven samples with the number of showers ≥ 3 and $d \leq 3^\circ$; (b) in seven samples without nodes; N_{exp} is the experimental distribution; N_{ran} is the expected distribution for the isotropic flux; and the numbers give the number of showers. Histograms *2*—the deviations $n_\sigma = (N_{exp} - N_{ran})/\sqrt{N_{ran}}$; the smooth curves *2* are the average variations.

outcomes $<10^{-4}$. These spatial PCR flux nonuniformities appear to be associated with small-scale structural features of the objects under consideration. Here, we consider only one point that complements the above assumption that the cluster showers are extragalactic in origin. This is clearly evidenced by the strong peak ($\approx 5\sigma$) in Fig. 7a (G) in the direction $l_G \approx 137^\circ$ that coincides with the line of intersection of the Galactic and Supergalactic planes (arrow *3* in Fig. 2). This peak is actually a local cut of the data in Fig. 6a (SG). It also shows up in Fig. 7a (SG) in the direction $l_{SG} \approx 94^\circ$. Figure 7b shows the distributions of the showers with energies $E_0 = 10^{17.7-17.8}$ eV from the Galactic and Supergalactic disks ($|b| \leq 2^\circ$) that were

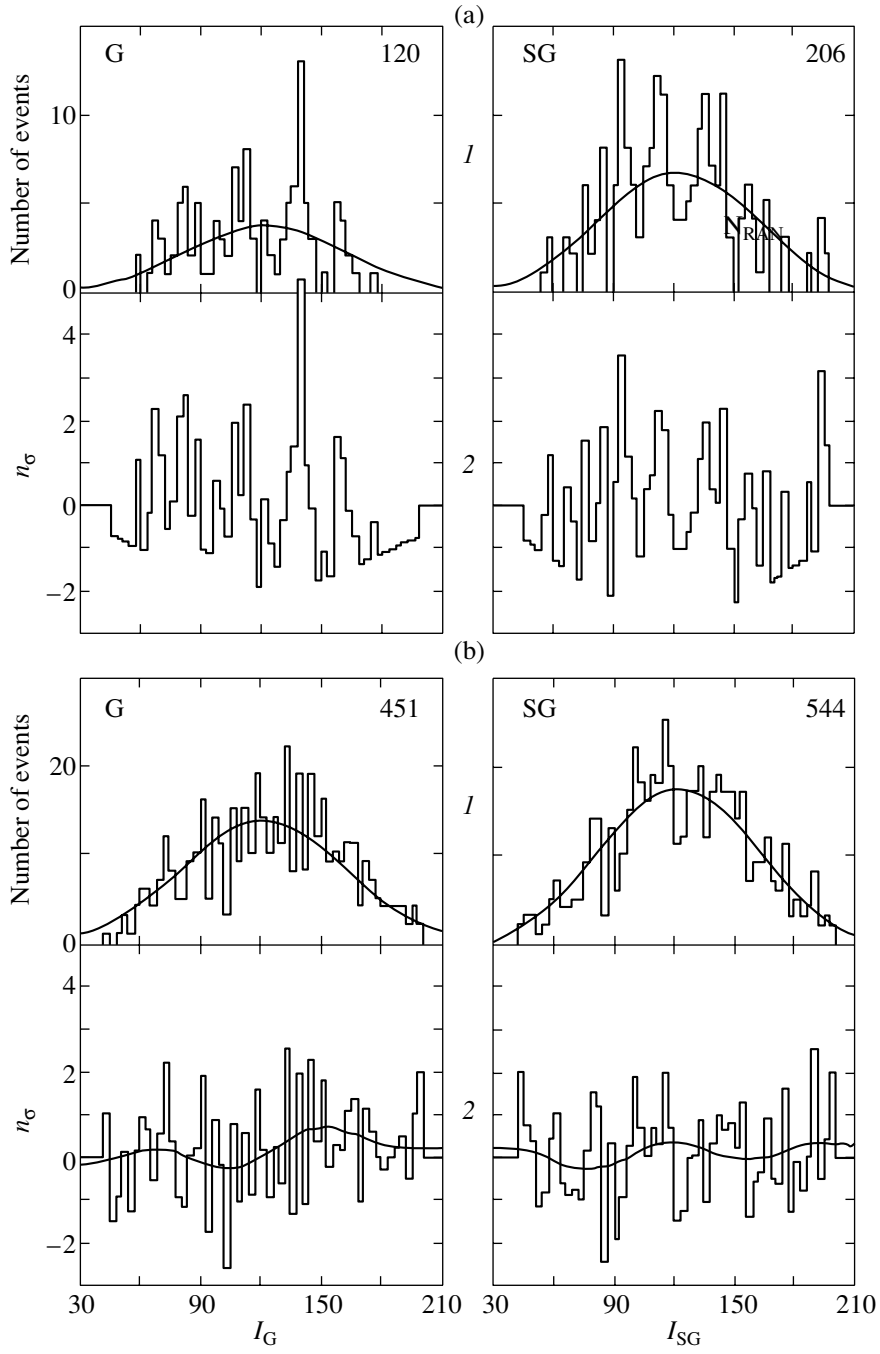

Fig. 7. The arrival longitude distributions of showers with $E_0 = 10^{17.7-17.8}$ eV that arrive from the Galactic (G) and Supergalactic (SG) disks ($|b| \leq 2°$). The notation is the same as in Fig. 6.

not included in the nodes and clusters. These were obtained similarly to Fig. 7a. Here, the measured and expected distributions for the isotropic PCR flux are consistent with each other ($\chi^2 = 54–63$).

Consider the anisotropy of PCRs with $E_0 = 10^{17.7-17.8}$ eV by a harmonic analysis separately in clusters and without them. The shower distributions in $n = 24$ sectors (at $\Delta\alpha = 15°$ steps) are shown in Fig. 8 (histograms *1* and *2*). We see that the distribution *2* of showers without clusters has an insignificant flux difference in different hour sectors. As a result, the phase $\varphi_1 \approx 211° \pm 136°$ in them was determined with a large uncertainty. These data still (see Fig. 6b and Fig. 7b) suggest that the PCRs are highly isotropic.

As for the showers in clusters in Fig. 8 (histogram *1*), as would be expected from the above dis-

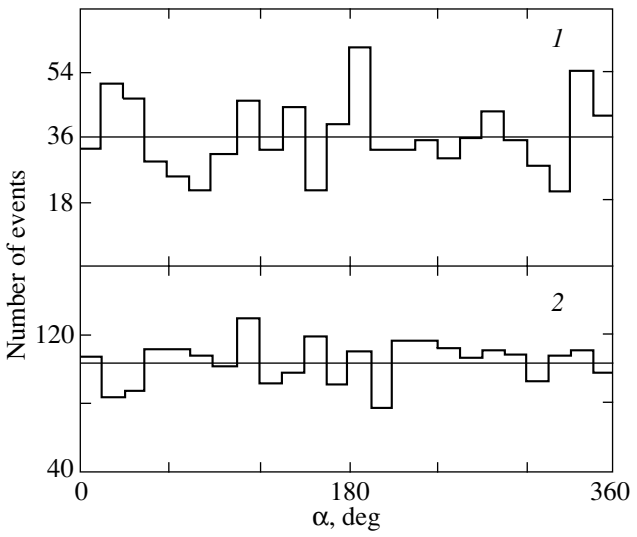

Fig. 8. The right ascension distributions of EASs with energies $E_0 = 10^{17.7-17.8}$ eV at nodes with the number of showers ≥ 3 and $d \leq 3^\circ$ (*1*) and in samples without nodes and clusters (*2*). The smooth curves represent the first harmonics of (4).

cussion, they are essentially inconsistent with the hypothesis of an isotropic distribution. Thus, the scatter of data near fit (*4*) leads to $\chi^2 \approx 71.6$ for $n = 24-3$ degrees of freedom, which corresponds to the probability of a random outcome $<10^{-5}$ (see Fig. 3).

Note some of the important features in these distributions. The peak in Fig. 8b (*1*) at $\alpha \approx 180^\circ-195^\circ$ points to excess radiation from the Supergalactic disk near the center ($C_{\rm SG}$ in Fig. 2), while the peak at $\alpha \approx 15^\circ-45^\circ$ points to an excess PCR flux along the line of intersection of the Galactic and Supergalactic planes (arrow *3* in Fig. 2). They agree with the peaks in these directions in Fig. 7a (SG). In contrast, the peak at $\alpha \approx 315^\circ-345^\circ$ probably refers to the Galactic disk.

The clusters can be assumed to form near local PCR sources. We see from the above data that at $E_0 \approx 10^{17.7-17.8}$ eV, they point to a certain relationship to the Supergalactic plane. The primary particles that constitute them are probably electrically neutral. Otherwise, because of their motion in the Galactic magnetic field, they would lose the relationship along the direction to the sources of their formation. It is unlikely that neutrons can be such particles. At the above energies, they have a Lorentz factor $\approx 5 \times 10^8$ and are able to traverse a distance of ≈ 5 kpc, which is many times smaller than the size of the Supergalaxy (≈ 50 Mpc), before their breakup. These are most likely some other stable neutral particles.

Therefore, consider muons with a threshold energy $E_\mu \approx 1.0 \sec\theta$ GeV whose content in the showers is sensitive to the PCR composition. The lateral distribution function (LDF) of EASs with energies $E_0 \approx 10^{17.7-17.8}$ eV and zenith angles $\cos\theta \geq 0.9$ is indicated by the filled circles in Fig. 9. The solid line represents the following fit to the experimental data

$$\rho_\mu(r) = N_\mu C_\mu (r/280)^{-0.75} \times (1 + r/280)^{0.75-b_\mu}(1 + r/2000)^{-6.5}, \quad (6)$$

where C_μ is the normalization constant, N_μ is the total number of muons at the observational level, and $b_\mu = 2.67 \pm 0.04$. The open circles represent the average LDF from Glushkov *et al.* (2000a, 2000b) for showers without any selection by arrival directions. The dashed line corresponds to (6) with $b_\mu = 1.99 \pm 0.04$ and is consistent with the calculations of Glushkov *et al.* (2000a, 2000b) based on the QGSJET model for a mixed PCR composition of light nuclei with a dominance of protons.

We see that the LDF of the muons in cluster showers is steep. The calculations mentioned above yield a much flatter distribution (6) with $b_\mu = 2.02$ for the primary protons. The air showers from protons and neutrons develop in the same way. Therefore, neutrons cannot be the hypothetical PCR particles either. Neither can gamma-ray photons be such particles, because, according to various model estimates, they produce EASs with the number of muons that is a factor of 7 to 15 smaller than protons do. These are most likely some other stable neutral particles.

DISCUSSION

Let us now consider the amplitude of the first harmonic A_1, which is a measure of the PCR anisotropy in a harmonic analysis. It is compared with the analogous amplitude ΔA_1 for the isotropic flux with the number of events equal to the actual number of showers

$$N = \sum_{i=1}^{n} N_i.$$

It can be calculated by the Monte Carlo method or analytically (Linsley 1975):

$$\Delta A_1 \cong 1.25 \times \sqrt{2/N}. \quad (7)$$

Relation (7) suggests that nonzero amplitudes whose values increase with decreasing number of events N will always be observed during an experiment, even in the absence of actual anisotropy. This occurs when the energy E_0 of the analyzed showers increases; i.e., a random distribution can imitate the physically expected variation of the harmonic amplitude with energy.

The distribution of parameters for the observed anisotropy vector that arises from a limited sample

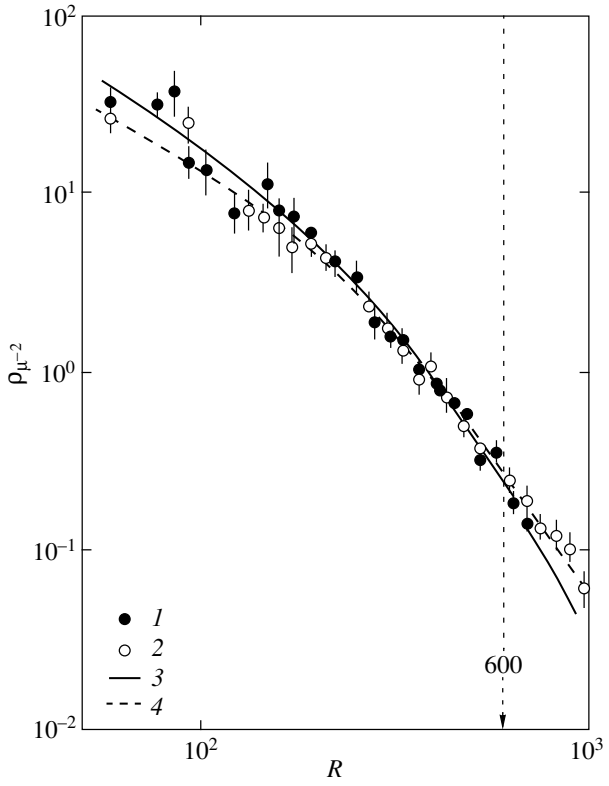

Fig. 9. The lateral distribution of muons (with a threshold energy $E_\mu \approx 1.0 \sec\theta$ GeV) in the showers with $E_0 = 10^{17.7-17.8}$ eV and $\cos\theta \geq 0.9$ included in clusters *1* and in a sample without cluster separation *2*: *3* and *4* fit (5) with $b_\mu = 2.67 \pm 0.04$ and $b_\mu = 2.02 \pm 0.03$, respectively.

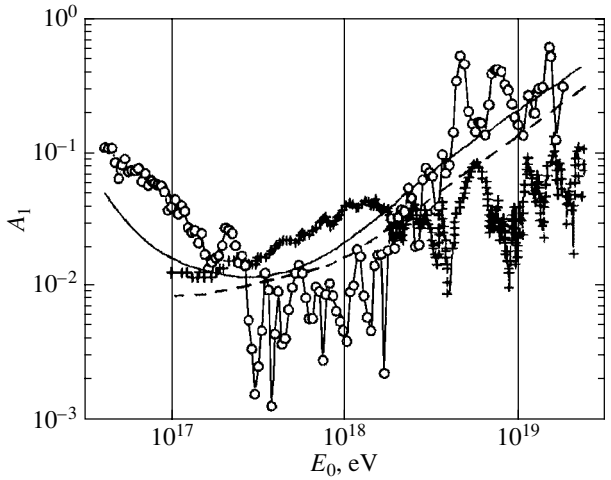

Fig. 10. The amplitude of the first harmonic versus the EAS energy (see Fig. 1 for notation); the solid and dashed lines represent the expected values for an isotropic flux for the Yakutsk and AGASA (Hayashida *et al.* 1999) arrays, respectively.

of N events was considered by Linsley (1975). This author introduced the coefficient $k = N(A_1/2)^2$ and the probability $p(\geq A_1)$ of obtaining the observed A_1 (or a larger value) for an isotropic flux:

$$p(\geq A_1) = \exp(-k). \qquad (8)$$

Figure 10 shows the measured amplitudes (circles) and the amplitudes calculated from relation (7) (solid line) that correspond to the phases φ_1 in Fig. 1. The experimental and calculated data from Hayashida *et al.* (1999) are indicated by the crosses and the dashed line, respectively. The coefficient k is shown in Fig. 11.

We see that at energies $E_0 \approx (3{-}20) \times 10^{17}$ eV, a clear anisotropy with the maximum amplitude at $E_0 \approx 10^{18}$ eV is observed at AGASA. By contrast, the Yakutsk array at these energies reveals small amplitudes A_1. Such a situation is not the result of poor shower statistics. This can be clearly seen from the histogram in Fig. 8, where the measured distributions proved to be anomalously flat; i.e., the sine wave (4) here differs only slightly from the horizontal line. At the same time, the data in angular sectors have many large deviations from this fit, which result in great χ^2 values that are unlikely for a random distribution (see Fig. 3).

In this case, the hypothesis that the Yakutsk array data at the above energies could be attributable to fluctuations in the isotropic PCR flux should be rejected. Here, the cause is probably different. In our view, the anomalously flat distribution of PCR arrival directions arose from the superposition of two counter fluxes with approximately the same amplitudes. This is clearly seen from Fig. 12, where we simulate this hypothesis. Number 1 indicates the original distribution taken for actual showers with energies $E_0 = 10^{16.8-16.9}$ eV and slightly modified so that the phase of the first harmonic points to the Supergalactic plane. We assume that this distribution with phase $\varphi_1 \approx 90^\circ$ roughly reflects the global extragalactic PCR anisotropy. Denote the total number of events in it by $N_{\rm SG}$. Parameters of the anisotropy vector for this distribution are given in the first row of the table.

Histogram *2* in Fig. 12 shows histogram *1* displaced in right ascension by 180°. Parameters of the anisotropy vector for this distribution are given in the second row of the table. These are consistent with the AGASA data. Therefore, we assume that this vector roughly characterizes the global Galactic PCR anisotropy. Denote the total number of events by $N_{\rm G}$.

The total Galactic and extragalactic flux N_Σ was determined by the summation of histograms *2* and *1* with the weights $W_{\rm G} + W_{\rm SG} = 1$:

$$N_\Sigma = W_{\rm G} N_{\rm G} + (1 - W_{\rm G}) N_{\rm SG}, \qquad (9)$$

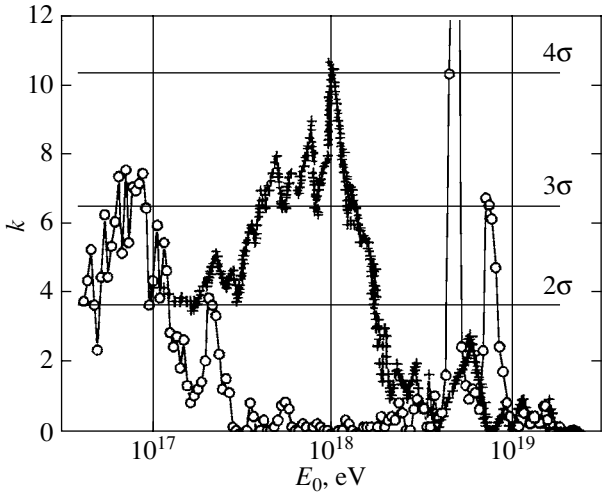

Fig. 11. The coefficient (k) in the formula $p(\geq A_1) = \exp(-k)$ to estimate the probability of obtaining a random amplitude of the first harmonic $\geq A_1$ (A_1 are the measured values in Fig. 10) versus the EAS energy.

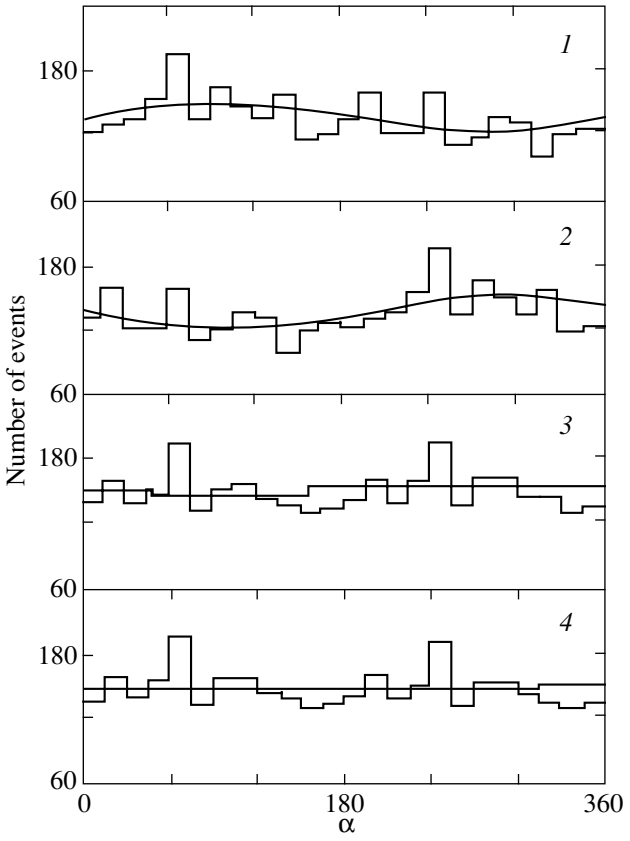

Fig. 12. An artificial distribution of showers in right ascension to simulate the extragalactic, *1*, Galactic, *2*, and their total, *3* and *4*, fluxes (with the anisotropy vector parameters in the table). The smooth curves are the first harmonics of *4*.

where W_G and W_{SG} are the fractions of the Galactic and extragalactic PCR. Histogram *3* in Fig. 12 indicates the case with $W_G = 0.55$, where the fraction of the Galactic PCR is slightly larger than the fraction of the extragalactic PCR. Parameters of the anisotropy vector for this flux are given in the third row of the table. We see that these are consistent with our experimental data.

Histogram *4* indicates the case with $W_G = 0.45$, where the fraction of the Galactic PCR is slightly smaller than the fraction of the extragalactic PCR. In this case, we also observe a distribution with an anomalously small coefficient k, but the phase $\varphi_1 \approx 67°$ points to the Supergalactic plane.

The last two simulation cases show that small changes in the equilibrium of the global counter fluxes in one or another direction shift the phase of the first harmonic toward the stronger flux. The χ^2 values are still large (at a confidence level $\approx 3\sigma$) and are inconsistent with the hypothesis that histograms *3* and *4* are random in nature.

If we attempt to use the simulation results to interpret the anisotropy at $E_0 \approx (3\text{–}20) \times 10^{17}$ eV of the Yakutsk array and AGASA data, then the following picture is possible. Let us assume that the PCR actually consist of the Galactic and extragalactic components. AGASA with a broader sky viewing angle (see Fig. 2) will then predominantly see the Galactic component. In fact, it is "blinded" by the direct cosmic-ray flux from the Galactic center. The Yakutsk EAS array located much farther to the north sees only a faint "gleam" of this component. The anisotropy of the Galactic component is neutralized by the anisotropy of the extragalactic particles, which at some energies tips the scales in its favor. Therefore, the phase of the first harmonic in Fig. 1 periodically varies greatly.

Outside the energy range $E_0 \approx (3\text{–}20) \times 10^{17}$ eV, the Yakutsk array data reveal [criteria (5) and (8) in coordination) significant PCR anisotropies (see Figs. 3 and 11). The strong peak at $E_0 \approx (4\text{–}8) \times 10^{18}$ eV is most likely extragalactic in origin. Glush-

Parameters of the first harmonic in simulating the anisotropy of the extragalactic (*1*), Galactic (*2*), and their total (*3*, *4*) fluxes

Fluxes	W_G	A_1, %	ΔA_1, %	φ_1, deg	X^2	k
1	0	10.6	3.1	96	58.8	9.1
2	1	12.2	3.1	285	58.1	11.7
3	0.55	2.0	3.1	302	41.2	0.3
4	0.45	1.1	3.1	67	41.3	0.1

kov and Pravdin (2001a, 2001b) showed that at $E_0 \geq 5 \times 10^{18}$ eV, the PCR arrival directions strongly correlate with the Supergalactic disk, while Glushkov (2002) pointed out that quasars with redshifts $z \leq 0.3$ could be the sources of PCRs with such energies.

CONCLUSIONS

Our results show that the global anisotropy of the ultrahigh energy PCR arrival directions estimated by a harmonic analysis is critical to the choice of energy bins, because the phase of the first harmonic can vary rapidly and greatly (Fig. 1). These variations are not random (Fig. 3) but are probably attributable to periodic superpositions of the extragalactic PCR flux on the Galactic radiation. This hypothesis is supported by the phases $\varphi_1 \approx 90°$, which point to the Supergalactic plane (Fig. 2) and which are statistically significant, $\geq 4\sigma$ (Fig. 3), with a confidence probability $\beta \geq 0.99996$. In our view, the rapid changes in phases φ_1 can be erroneously perceived as the absence of anisotropy or as evidence of insufficient statistics of the detected showers.

In the case of small measured amplitudes A_1 where their values are much smaller than those admitted by isotropic flux fluctuations, formula (8) is unsuitable for estimating the probability of such a random outcome, because the coefficient k is very small, close to zero. However, quantity (5), which characterizes the χ^2 distribution, still remains effective in estimating the PCR anisotropy by a harmonic analysis.

ACKNOWLEDGMENTS

This study was carried out with the support of the Yakutsk EAS array by the Ministry of Science of Russia (register no. 01-30), which was included in the "List of Unique Research and Experimental Facilities of National Importance," and with support of the Russian Foundation for Basic Research (project no. 00-15-96787; Support of Leading Scientific Schools).

REFERENCES

1. B. N. Afanasiev, M. N. Dyakonov, T. A. Egorov, *et al.*, in *Proceedings of 24th Int. Conf. on Cosmic Rays*, *Rome, 1995*, Vol. 2, p. 796.
2. R. N. Coy, J. Lloyd-Evans, M. Patel, *et al.*, in *Proceedings of 17th Int. Conf. on Cosmic Rays*, *Paris, 1981*, Vol. 9, p. 183.
3. A. V. Glushkov, *Jets in Cosmic Rays?*, Preprint Inst. Kosmofiz. Issled. Aeronom., Siberian Branch of the Russian Academy of Sciences, Yakutsk (1988).
4. A. V. Glushkov, I. T. Makarov, M. I. Pravdin, *et al.*, Pis'ma Zh. Éksp. Teor. Fiz. **71**, 145 (2000a) [JETP Lett. **71**, 97 (2000a)].
5. A. V. Glushkov, M. I. Pravdin, I. E. Sleptsov, *et al.*, Yad. Fiz. **63**, 1557 (2000b) [Phys. At. Nucl. **63**, 1477 (2000b)].
6. A. V. Glushkov and M. I. Pravdin, Zh. Éksp. Teor. Fiz. **119**, 1029 (2001a) [JETP **92**, 887 (2001a)].
7. A. V. Glushkov and M. I. Pravdin, Pis'ma Astron. Zh. **27**, 577 (2001b) [Astron. Lett. **27**, 493 (2001b)].
8. A. V. Glushkov, M. I. Pravdin, I. E. Sleptsov, *et al.*, Yad. Fiz. **65**, 1346 (2002) [Phys. At. Nucl. **65**, 1313 (2002)].
9. A. V. Glushkov and M. I. Pravdin, Pis'ma Astron. Zh. **28**, 341 (2002) [Astron. Lett. **28**, 296 (2002)].
10. A. V. Glushkov, Izv. Ross. Akad. Nauk, Ser. Fiz. **66**, 1601 (2002).
11. N. Hayashida, M. Nagano, D. Nishikawa, *et al.*, Astropart. Phys. **10**, 303 (1999).
12. J. Linsley, Phys. Rev. Lett. **34**, 1530 (1975).
13. J. Linsley and A. A. Watson, Phys. Rev. Lett. **46**, 459 (1981).
14. J. Lloyd-Evans and A. A. Watson, *Invited Talks at the 8th European Cosmic Rays Symp.*, *Bologna, 1983*.
15. A. G. Lyne and F. Graham-Smith, *Pulsar Astronomy* (Cambridge Univers., 1990).
16. A. A. Mikhailov and M. I. Pravdin, Pis'ma Zh. Éksp. Teor. Fiz. **66**, 289 (1997) [JETP Lett. **66**, 305 (1997)].
17. M. I. Pravdin, M. N. Dyakonov, A. V. Glushkov, *et al.*, in *Proceedings of 26th Int. Conf. on Cosmic Rays*, *Salt Lake City, 1999*, Vol. 3, p. 292.
18. M. I. Pravdin, A. A. Ivanov, A. D. Krasil'nikov, *et al.*, Zh. Éksp. Teor. Fiz. **119**, 881 (2001a) [JETP **92**, 766 (2001a)].
19. M. I. Pravdin, A. A. Ivanov, V. A. Kolosov, *et al.*, in *Proceedings of 27th Int. Conf. on Cosmic Rays*, *Hamburg, 2001b*, p. 394.
20. H. Sommers, Invited, Rapporteur and Highlight Papers, in *Proceedings of 27th Int. Conf. on Cosmic Rays*, *Hamburg, 2001*, p. 170.
21. A. A. Watson, Nucl. Phys. B, Proc. Suppl. **28**, 3 (1992).

Translated by V. Astakhov

Astronomy Letters, Vol. 29, No. 3, 2003, pp. 153–157. Translated from Pis'ma v Astronomicheskiĭ Zhurnal, Vol. 29, No. 3, 2003, pp. 184–189.

Unipolar Induction of a Magnetized Accretion Disk around a Black Hole

A. A. Shatskii*

Astrospace Center, Lebedev Institute of Physics, Russian Academy of Sciences, Profsoyuznaya ul. 84/32, Moscow, 117997 Russia

Received October 3, 2002

Abstract—The structure and magnitude of the electromagnetic field produced by a rotating accretion disk around a black hole were determined. The disk matter is assumed to be a magnetized plasma with a frozen-in poloidal magnetic field. The vacuum approximation is used outside the disk. © *2003 MAIK "Nauka/Interperiodica".*

Key words: *pulsars, neutron stars; black holes, quasars, jets, accretion disks.*

INTRODUCTION

Recently, various models of particle acceleration near supermassive black holes (SMBHs) in galactic nuclei and near stellar-mass black holes (BHs) in the Galaxy have been widely discussed in connection with the studies of synchrotron radiation and inverse Compton scattering from narrow-beam jets observed over a wide spectral range, from radio to gamma rays. Nevertheless, the particularly high angular resolution provided by radio interferometers does not allow the central part of a quasar to be distinguished, suggesting that the jet width is extremely small (comparable to the gravitational radius).

Previously (Shatskii 2001), the mechanism of Blandford and Znajek (1977) and Blandford (2001) for electric-field generation through the interaction of the magnetic field from a ring current with the gravimagnetic field (GMF) of a Kerr BH located on the common axis with the ring current was used as the model of particle acceleration. Bisnovatyi-Kogan and Blinnikov (1972) and Shatskii and Kardashev (2002) considered the mechanism of Deutsch (1955) or Goldreich and Julian (1969) for electric-field generation by the unipolar induction produced by the axial rotation of an accretion disk with a frozen-in magnetic field. Here, we suggest a mechanism that combines a unipolar inductor and strong gravitational SMBH effects. Naturally, this mechanism is closer to the actual processes that take place in quasars.

In contrast to the mechanism of Blandford and Znajek (1977), Beskin *et al.* (1992), and Beskin (1997), the mechanisms of Bisnovatyi-Kogan and Blinnikov (1972) used previously (Shatskii 2001; Shatskii and Kardashev 2002) operate in the vacuum approximation; the validity criterion for the latter is the condition of Goldreich and Julian (1969) for the number density of free charges:

$$n_e < |(\mathbf{\Omega H})|/(2\pi ce). \quad (1)$$

Here, $\mathbf{\Omega}$ is the plasma angular velocity, $\mathbf{H}$ is the characteristic magnetic field, c is the speed of light, and e is the elementary charge. Shatskii and Kardashev (2002) showed that condition (1) could be satisfied near a BH, because there are no stable orbits for the particles closer than three gravitational radii (in a Schwarzschild field). The matter for which the vacuum approximation breaks down must be in the accretion disk, which, because of the effect of Bardeen and Petterson (1975), must be located in the equatorial plane of a rotating BH. We do not consider models in which the vacuum approximation breaks down in the entire space outside a BH (models with the magnetohydrodynamic approximation). These were considered in detail, for example, in the review articles by Beskin *et al.* (1992) and Beskin (1997).

Here, we determine the energy of the charged particles accelerated by the unipolar mechanism, as well as the configurations of the electromagnetic field and the acceleration region.

CONSTRUCTING THE MODEL

Consider a Schwarzschild BH surrounded by an equatorial accretion disk. Let the disk have the characteristic size R and width $2a$ (see the figure). Because of the Bardeen–Petterson effect, the disk thickness can be disregarded.

We use the following notation: M is the mass of the central body, $r_g = 2M$ is the Schwarzschild

*E-mail: shatskiy@lukash.asc.rssi.ru

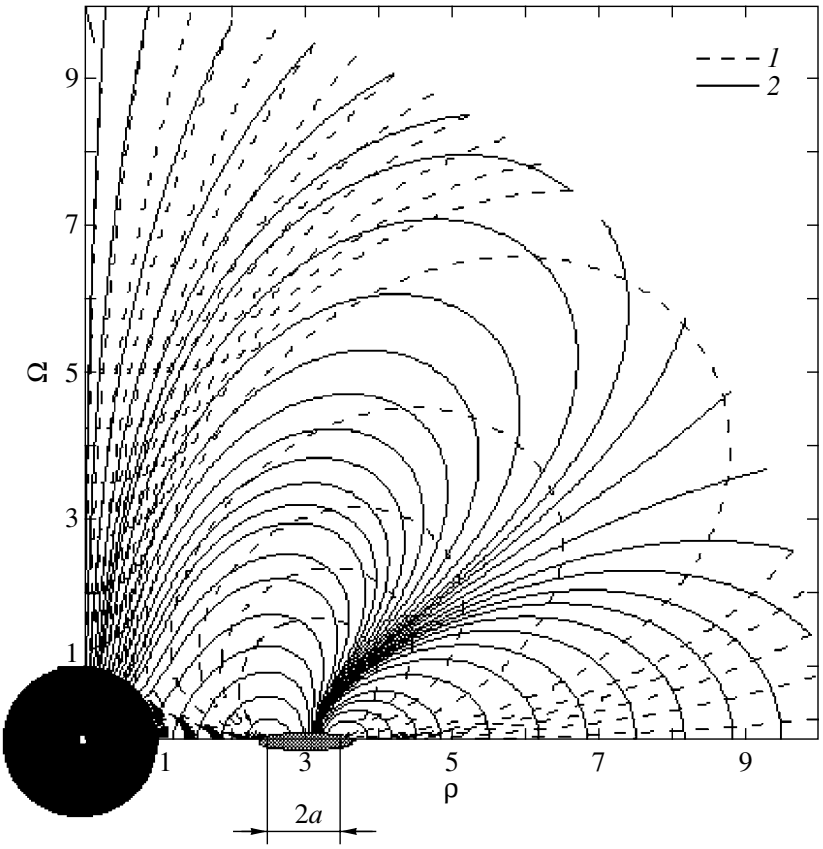

The upper right quarter of the electromagnetic field line pattern in the system. The dashed (*1*) and solid (*2*) lines indicate the electric and magnetic fields, respectively. There is a black hole at the center of the system. An accretion disk of width $2a = 1$ is in the equatorial plane, at distance $R = 3$ (in units of r_g).

radius,[1] m is the mass of the test particle, u^j is its 4-velocity, $F_{ij} = \partial_i A_j - \partial_j A_i$ is the electromagnetic-field (EMF) tensor, A_j is the EMF potential, and Γ^i_{jk} are the Christoffel symbols.

Let us write the Schwarzschild metric and its determinant in spherical coordinate:

$$ds^2 = (1 - r_g/r)dt^2 - (1 - r_g/r)^{-1}dr^2 - r^2 d\theta^2 - r^2 \sin^2\theta d\varphi^2, \quad (2)$$
$$g = -r^4 \sin^2\theta.$$

In general relativity, the following quantity for a charged particle that moves in stationary fields is conserved:

$$\varepsilon = m(u_0 - 1) + eA_0, \quad (3)$$

which matches the particle energy in the nonrelativistic case. To prove this, it will suffice to consider the equation of motion for a charged particle in general relativity (see Landau and Lifshitz 1988):

$$m\frac{du_i}{ds} = mu^k u_l \Gamma^l_{ik} + eu^k F_{ik}, \quad (4)$$

where ds is the element of the particle proper time [see formulas (2)]. After transformation, this expression reduces to

$$\frac{d}{ds}(mu_i + eA_i) = \frac{m}{2}u^l u^k \partial_i g_{kl} + eu^k \partial_i A_k. \quad (5)$$

The conservation of energy ε throughout the particle evolution follows for $i = 0$ in stationary fields.

Since the magnetic field is frozen into the disk, its distribution inside the disk is determined only by the initial conditions of the problem. These conditions depend on the accretion-disk formation mechanism. If the disk is assumed to have been formed through the destruction of a star by BH tidal forces, then the magnetic field of this star in the disk will preserve its direction. This field can have the profile shown in the figure.

In the frame of reference comoving with the accretion disk, there is no electric field inside the disk

[1] Below, we use the system of units in which the speed of light and the gravitational constant are equal to unity: $c = 1$, $G = 1$.

because of its conductivity. Therefore, in a fixed frame of reference (with respect to distant stars), an electric field is induced by disk rotation inside the disk.

Let the plasma in the disk rotate at an angular velocity Ω relative to distant stars. The transformation of coordinates to a rotating frame is then:[2]

$$dx^i = dx'^k[\delta^i_k + \Omega\delta^i_\varphi\delta^0_k]. \quad (6)$$

Because of axial symmetry, only the following EMF potential components are nonzero: A_0, the electric-field potential, and A_φ, the magnetic-field potential. According to (6) (see Landau and Lifshitz 1988), the EMF components transform as

$$A'_0 = A_0 + \Omega A_\varphi, \quad A'_\varphi = A_\varphi, \quad (7)$$
$$F'_{\alpha 0} = F_{\alpha 0} + \Omega F_{\alpha\varphi}, \quad F'_{\alpha\varphi} = F_{\alpha\varphi}.$$

Since $F'_{\alpha 0} = 0$ in plasma, we have inside the disk

$$F_{\alpha 0} = -\Omega F_{\alpha\varphi}, \quad A_0 = \text{const} - \Omega A_\varphi. \quad (8)$$

On the disk surface, continuous boundary conditions exist for the tangential electric-field components and for the normal magnetic-field components. Outside the disk, there are no field sources by the definition of the model. Thus, determining the EMF reduces to solving the Laplace equation in the spacetime curved by gravity with the specified boundary conditions on the disk surface and on the BH horizon. The boundary conditions for the EMF tensor the BH horizon were found previously (Shatskii 2001):

$$\lim_{r\to r_g} F_{0\theta} \propto g_{00} \to 0, \quad \lim_{r\to r_g} F^{r\varphi} \propto g_{00} \to 0. \quad (9)$$

In turn, the boundary conditions on the disk for the magnetic and electric fields are determined solely by the magnetic-field distribution inside it. The specific form of this distribution is not that important for the solution of the problem. This is because at distances from the disk to the point of observation much larger than the disk thickness, the dipole field (the monopole field must be absent, because the total disk charge is zero) mainly contributes to the electric field of the disk element within position angles between φ and $\varphi + d\varphi$ when the field is expanded in multipoles. In this case, the total electric field obtained by integrating over the angle φ has a quadrupole nature:

$$\lim_{(r/r_g)\to\infty} A_0 = \text{const} \times (1 - 3\cos^2\theta)/r^3.$$

[2]Unless otherwise specified, $x^i = t, r, \theta, \varphi$; $x^\alpha = R, \theta$ (Greek and Roman indices).

THE MAXWELL EQUATIONS

The Maxwell equations for the EMF in general relativity are

$$\frac{1}{\sqrt{-g}}\partial_i(\sqrt{-g}F^{ik}) = 4\pi j^k. \quad (10)$$

In the disk, the 4-vector of the current j^k can be determined from a given magnetic field. Let us introduce the physical components of the EMF vectors, their analogs in Euclidean space:[3]

$$\hat{\mathbf{E}}^\alpha = -F_{\beta 0}\sqrt{|g^{00}g^{\alpha\beta}|}, \quad (11)$$
$$\hat{\mathbf{H}}_\alpha = -e_{\alpha\beta\varphi}F_{\gamma\varphi}\sqrt{|g^{\gamma\beta}g^{\varphi\varphi}|},$$
$$\hat{\mathbf{J}}^\alpha = j^\beta\sqrt{|g_{\alpha\beta}|}.$$

Here, $e^{\alpha\beta\gamma} = e_{\alpha\beta\gamma}$ is the Levi–Civita symbol. This form of the EMF physical components was chosen so that Eq. (10) corresponds to the classical Maxwell equations in Euclidean space:

$$\text{div}\,\hat{\mathbf{E}} = 4\pi j^0, \quad \text{curl}\,\hat{\mathbf{H}} = 4\pi\hat{\mathbf{J}}. \quad (12)$$

THE ELECTROMAGNETIC FIELD NEAR A SMBH

The magnetic field of an accretion disk around a Schwarzschild BH was determined by Tomimatsu and Takahashi (2001). The electric field of the disk element within position angles between φ and $\varphi + d\varphi$ can be represented as the field from two charges $+q\frac{d\varphi}{2\pi}$ and $-q\frac{d\varphi}{2\pi}$, located inside the disk; at the system equator; and at distances $+a$ and $-a$ from its center ($r = R, \theta = \pi/2$), respectively.[4] As a result, we obtain an electric dipole $2qad\varphi/\pi$ in the disk element between φ and $\varphi + d\varphi$. In Euclidean space, the radial electric field at the disk center can be obtained by integrating over the angle φ; for $a \ll R$, it is $E_0 = \hat{E}^r_{(r=R,\ \theta=\pi/2)} = -2q/(\pi Ra)$. The corresponding magnetic field (which is responsible for the emergence of the electric field) can be found from the electric field. Note that nothing forbids the frozen-in magnetic field in the disk from having precisely such a profile (see the figure).

In the figure, the accretion disk is located at $r \approx 6M$. The contradictions related to the existence of stable orbits in this region can be removed by the following reasoning:

[3]We denote them by a hat.

[4]Naturally, there are no free charges in the disk; these were introduced for the convenience of representing the dipole field outside the disk.

(1) For the Kerr metrics, the nearest stable orbit is at radius $r = M$ (see, e.g., Landau and Lifshitz 1988).

(2) Even if the orbit is not stable, it is spiral and goes under the horizon, while a new orbit can arrive in place of it. Thus, the pattern is quasi-stationary.

According to (11) and (8), the quantity q can be expressed in terms of the magnetic field at the disk center[5] as follows:

$$q = -\pi RaE_0/2 = \frac{\pi}{2}\Omega R^2 a H_0. \qquad (13)$$

In physical coordinates, the field of a point charge e near a BH was presented by Thorne *et al.* (1998). It was obtained in closed form by Linet (1976):

$$A_0 = \frac{e}{Rr}\left[M + \frac{(R-M)(r-M) - M^2 t}{D}\right], \quad (14)$$

$$\hat{E}^r = \frac{e}{Rr^2}\left\{M\left[1 - \frac{R-M+Mt}{D}\right] + \frac{r\left[(r-M)(R-M) - M^2 t\right]\left[r - M - (R-M)t\right]}{D^3}\right\},$$

$$\hat{E}^\theta = -\frac{e(R-2M)\sqrt{1-2M/r}}{D^3}\partial_\theta t,$$

$$D^2 = (r-M)^2 + (R-M)^2 - M^2 - 2(r-M)(R-M)t + M^2 t^2,$$

where t is the cosine of the angle between the directions of the point charge and the point of observation of the field from the BH center.

The electric field of a charged ring at the BH equator was found by Bičak and Dvorak (1976) in the form of a series. Here, this field is found in quadrature form. To this end, we make the substitutions $t \to \sin\theta\cos\varphi$ and $e \to q\dfrac{d\varphi}{2\pi}$ and integrate over the angle from $-\pi$ to $+\pi$. The model electric-field potential $A_0^{\rm tot}$ is a superposition of the fields from two charged rings at radii $R + a$ and $R - a$ and with charges $+q$ and $-q$, respectively. The quadrature obtained can be expressed in terms of incomplete elliptic integrals. Since this quadrature is cumbersome, it makes no sense to write it here. Instead, we give an expression more useful for practical calculations, an expansion of this quadrature in terms of a. We retain only the first term of the series (because $a \ll R$ is small):[6]

$$A_0^{\rm tot} = \int_{-\pi}^{+\pi} 2a\partial_R A_0 d\varphi = \int_0^{\pi} 4a\left(\partial_r A_0\right)_{(R\leftrightarrow r)} d\varphi = \int_0^{\pi} 4a\hat{E}^r_{(R\leftrightarrow r)} d\varphi.$$

Substituting expression (14) here finally yields

$$A_0^{\rm tot} = \frac{2aq}{\pi r R^2}\int_0^{\pi} d\varphi\left(\frac{M(D - r + M - Mt)}{D} + \frac{R\left[(r-M)(R-M) - M^2 t\right]\left[R - M - (r-M)t\right]}{D^3}\right). \qquad (15)$$

On the Ω axis, the integration over φ is simple and it is easy to see that the only maximum of the potential $A_0^{\rm tot}$ (outside the BH) is on the horizon ($r = 2M$):

$$|A_0^{\rm tot}(r = 2M, \theta = 0)|_{\max} = \frac{\pi\Omega a^2 R^2 H_0}{R^2 - a^2}. \qquad (16)$$

Consider the distribution of energies $\varepsilon(r)$ in an ensemble of test particles at rest on the Ω axis [see (3)]. This distribution has a weak maximum near the horizon and then slowly falls off to zero at distances $r \gg r_{\rm g}$. Subsequently, the energy variation can be virtually disregarded.

DISCUSSION

The necessary condition for particle escape to infinity from rest is the positiveness of the force $m\dfrac{du^r}{ds} = m\dfrac{d^2 r}{ds^2}$ that acts on the test particle at the starting point. This requires that the charge of the test particle e have the sign opposite to that of q:

$$-\mathrm{sign}(eq) = \mathrm{sign}(e\boldsymbol{\Omega}\hat{\mathbf{E}}_{(\theta=0)}) = -\mathrm{sign}(e\boldsymbol{\Omega}\mathbf{H}_0) = 1. \qquad (17)$$

The force that acts on a particle is proportional to the particle energy gradient [see Eq. (4)]:

$$m\frac{du^r}{ds} = -(\partial_r\varepsilon)\sqrt{1-2M/r}. \qquad (18)$$

In the main order in $\alpha = mM/(eq) \ll 1$, the energy maximum is almost equal to the electric component of the particle energy on the horizon,[7]

$$\varepsilon_{\max} = \left(\frac{1}{\alpha}\frac{2Ma}{R^2 - a^2} - 1\right)mc^2 \sim 0.1mc^2/\alpha, \quad (19)$$

and the point at which this maximum is reached is at the following distance from the horizon:

$$r_{\max} - r_{\rm g} = r_{\rm g}\alpha^2 \qquad (20)$$

[5] $H_0 = -\hat{H}_{\theta(r=R,\ \theta=\pi/2)}/\sqrt{1 - R_{\rm g}/R}$.

[6] Here, we make use of the symmetry of the potential A_0 in variables R and r and use their substitution (the subscript "$_{(R\leftrightarrow r)}$").

[7] At $a \sim r_{\rm g} \sim R/3$ [see (16)].

$$\times \frac{(R^2-a^2)^2[(R-M)^2-a^2]^4}{16M^6a^2(3R^2+M^2-4MR+a^2)^2} \sim r_{\rm g}10^3\alpha^2.$$

In conclusion, several more words can be said about the same model in a Kerr field. BH rotation gives rise to a GMF that interacts with the EMF of the disk and changes its components in magnitude and direction. In the linear approximation in BH angular velocity, the GMF gives an additive component to expression (19) for the maximum energy of the charged particle accelerated by an electric field. This component was determined previously (Shatskii 2001); it is convenient to represent it here as

$$\varepsilon_{\rm g} \approx \frac{1}{2\pi^2}\left(\frac{\Omega_{\rm g}r_{\rm g}}{\Omega R}\right)\left(\frac{r_{\rm g}^2}{aR}\right)mc^2/\alpha \sim \varepsilon_{\max}. \quad (21)$$

Here, $\Omega_{\rm g}$ is the angular velocity of the BH horizon (the falling test particles are drawn into rotation by the BH GMF). We see from (19) that at

$$\alpha^{-1} \approx \left(\frac{\Omega R}{c}\right)\left(\frac{aR}{r_{\rm g}^2}\right)\left(\frac{H_0}{10^4\ {\rm G}}\right) \times \left(\frac{M}{10^9M_\odot}\right)\left(\frac{m_e}{m}\right)10^{15} \quad (22)$$

the particle energy[8] accelerated by SMBHs can reach values larger than 10^{20}.

CONCLUSIONS

(1) The model described above yields even a higher energy of the accelerated particles than does the Blandford–Znajek model.

(2) The energy excess can be expended on the radiation reaction and on collisions with particles of the rarefied plasma near the axis.

(3) The derived EMF configuration can be used to numerically calculate the dynamics of the charged particles far from the axis. It will make it possible to compare theoretical conclusions with observational data.

(4) Far from the axis, a force-free field with the approximation of magnetohydrodynamic models can give a large contribution to the EMF amplitude. Therefore, in numerical calculations, the contributions to the EMF configuration from different models should be taken into account with different weights.

ACKNOWLEDGMENTS

This work was supported by the Russian Foundation for Basic Research (project nos. 01-02-16812, 00-15-96698, and 01-02-17829). I wish to thank N.S. Kardashev, R.F. Polishchuk, V.N. Lukash, B.V. Komberg, Yu.Yu. Kovalev, the remaining staff of the theoretical departments at the Astrospace Center and the Lebedev Institute of Physics, and the participants of workshops for an active participation in preparing this paper and for important remarks.

REFERENCES

1. J. M. Bardeen and J. A. Petterson, Astrophys. J. Lett. **195**, L65 (1975).
2. V. S. Beskin, Usp. Fiz. Nauk **167**, 689 (1997).
3. V. S. Beskin, Ya. N. Istomin, and V. I. Par'ev, Astron. Zh. **69**, 1258 (1992) [Sov. Astron. **36**, 642 (1992)].
4. J. Bičak and L. Dvorak, Gen. Relativ. Gravit. **7**, 959 (1976).
5. G. S. Bisnovatyi-Kogan and S. I. Blinnikov, Astrophys. Space Sci. **19**, 119 (1972).
6. R. Blandford and R. Znajek, Mon. Not. R. Astron. Soc. **179**, 433 (1977).
7. R. Blandford, in *Proceedings of IAI Symp. 205*, Ed. by R. T. Schilizzi (ASP, San Francisco, 2001), p. 10.
8. J. Deutsch, Ann. Astrophys. **l**, 1 (1955).
9. P. Goldreich and W. H. Julian, Astrophys. J. **157**, 869 (1969).
10. L. D. Landau and E. M. Lifshitz, *Field Theory* (Nauka, Moscow, 1988).
11. B. Linet, J. Phys. A **9**, 1081 (1976).
12. K. Thorne, P. Price, and D. MacDonald (Eds.), *Black Holes. A Membrane Approach* (Mir, Moscow, 1998).
13. A. Tomimatsu and M. Takahashi, Astrophys. J. **552**, 710 (2001).
14. A. A. Shatskii, Zh. Éksp. Teor. Fiz. **93**, 1062 (2001) [JETP **93**, 920 (2001)].
15. A. A. Shatskii and N. S. Kardashev, Astron. Zh. **46**, 708 (2002) [Astron. Rep. **46**, 639 (2002)].

Translated by G. Rudnitskii

[8] Here, $m_{\rm e}$ is the electron mass.

Astronomy Letters, Vol. 29, No. 3, 2003, pp. 158–162. Translated from Pis'ma v Astronomicheskiĭ Zhurnal, Vol. 29, No. 3, 2003, pp. 190–194.

Exchange and Correlation Interactions in Electron–Positron Plasma

A. V. Yudin* **and D. K. Nadyozhin**

Institute for Theoretical and Experimental Physics,
ul. Bol'shaya Cheremushkinskaya 25, Moscow, 117259 Russia

Received October 15, 2002

Abstract—The effect of particle–particle interaction on the adiabatic index γ for an electron–positron plasma is considered. An improved method for numerically calculating the Hartree–Fock exchange integral is presented and its relativistic asymptotics is determined. An approximation formula is derived for the correlation part of the interaction in the low-density limit. This formula includes degeneracy and the positron component. © *2003 MAIK "Nauka/Interperiodica"*.

Key words: *plasma astrophysics, hydrodynamics, and shock waves.*

INTRODUCTION

Let us consider the effect of particle–particle interaction on the thermodynamic functions of the plasma in the limit $\rho \to 0$. Particular attention will be given to the adiabatic index $\gamma = \left(\frac{\partial \ln P}{\partial \ln \rho}\right)_S$, a quantity that plays a significant role in the theory of stellar structure and, in particular, in problems concerning stellar stability and equilibrium. The problem of stellar-configuration equilibrium is known to reduce to the question of the sign of the equilibrium parameter $(\overline{\gamma} - 4/3)$, where $\overline{\gamma}$ is the star-averaged adiabatic index. Therefore, it is important to find out how the interaction affects this quantity with emphasis placed on the region $\gamma \sim 4/3$.

We consider a completely ionized electron–positron plasma in equilibrium with blackbody radiation. The equilibrium condition implies that $\mu_e + \mu_p = 0$, where μ_e and μ_p are the electron and positron chemical potentials, respectively. The presence of the positron component makes the low-density limit nontrivial, because the number of electron–positron pairs at $\rho = 0$ is not equal to zero but is a function of the temperature. This case is also of interest for the following two reasons. First, the effect of the ion component that makes a significant contribution in other regions vanishes here, which allows us to trace the properties of the electron–positron plasma, as it were, in a pure form. Of course, the final results also include blackbody radiation. Second, for $T \to 0$, when the interaction effect is large, the number of pairs is exponentially small and, conversely, for $T \to \infty$, the interaction effect generally decreases, but the number of pairs increases as T^3; i.e., it is hard to tell in advance in what temperature range the interaction will be significant. Therefore, this case requires special analysis.

We will first consider the exchange and correlation contributions to the thermodynamic quantities without assuming the density to be zero, derive the corresponding asymptotics, and only in the final results will we pass to the limit $\rho \to 0$.

THE EXCHANGE INTERACTION

The contribution from the exchange part of the interaction between particles of the same type (electrons or positrons) to the thermodynamic potential Ω is given by the following expression (see, e.g., Kovetz *et al.* 1972):

$$\triangle\Omega_{ex} = \frac{Ve^2}{h^6}\int\int n_1 n_2 \epsilon_{ex}(\mathbf{p}_1, \mathbf{p}_2) d^3\mathbf{p}_1 d^3\mathbf{p}_2. \quad (1)$$

Here,

$$n_k = \frac{1}{\exp\left(\frac{\varepsilon_k - \mu}{T}\right) + 1};$$

$$\varepsilon_k = mc^2\sqrt{1 + \left(\frac{p_k}{mc}\right)^2}; \quad k = 1, 2;$$

$$\epsilon_{ex}(\mathbf{p}_1, \mathbf{p}_2) = \frac{4\pi\hbar^2 c^2}{\varepsilon_1\varepsilon_2} \times \left(1 - \frac{m^2c^4}{\varepsilon_1\varepsilon_2 - m^2c^4 - (\mathbf{p}_1\mathbf{p}_2)}\right) c^2;$$

*E-mail: udin_avelmer@mtu-net.ru

1063-7737/03/2903-0158$24.00

and μ is the chemical potential with an allowance made for the rest energy mc^2. Integrating over the angles and transforming the integrand to dimensionless form yields

$$\triangle\Omega_{\rm ex} = 4\pi V e^2 \left(\frac{mc}{h}\right)^4 f_{\rm ex}(\alpha, w), \qquad (2)$$

$$f_{\rm ex} = \int_0^\infty \int_0^\infty \frac{n_1 n_2 \xi_1^2 \xi_2^2 d\xi_1 d\xi_2}{\sqrt{1+\xi_1^2}\sqrt{1+\xi_2^2}}$$

$$\times \left[2 - \frac{1}{\xi_1\xi_2} \ln \left| \frac{\sqrt{1+\xi_1^2}\sqrt{1+\xi_2^2} - 1 + \xi_1\xi_2}{\sqrt{1+\xi_1^2}\sqrt{1+\xi_2^2} - 1 - \xi_1\xi_2} \right| \right].$$

Here, $\alpha = mc^2/T$; $w = \mu/mc^2$; and $\xi_k = p_k/mc$; n_k is the previous expression written in terms of the introduced quantities, i.e., with $\alpha\left(\sqrt{1+\xi_k^2} - w\right)$ in the exponential.

Weak Degeneracy

Kovetz *et al.* (1972) showed that in the weak-degeneracy limit, i.e., for $w < 1$, this double integral can be reduced to the sum of the single integrals that are the integral representation of the Macdonald functions:

$$f_{\rm ex} = \frac{2}{\alpha} \sum_{m,n=1}^{\infty} \frac{(-e^{\alpha w})^{n+m}}{m+n} (a_n b_m + a_m b_n),$$

$$a_n = \int_0^\infty e^{-n\alpha\sqrt{1+x^2}} dx = K_1(n\alpha),$$

$$b_n = \int_0^\infty \frac{x^2-1}{\sqrt{1+x^2}}\, e^{-n\alpha\sqrt{1+x^2}} dx$$

$$= \frac{K_1(n\alpha)}{n\alpha} - K_0(n\alpha),$$

where $K_i(x)$ are the Macdonald functions. However, this result, which we obtained independently, is not quite convenient for practical calculations: at $w \sim 1$, the series converges slowly. The following equivalent representation is more effective:

$$f_{\rm ex} = \frac{2}{\alpha} \sum_{l=1}^{\infty} \frac{1}{[1+2e^{\alpha(1-w)}]^{l+1}} \qquad (3)$$

$$\times \sum_{n=1}^{l} \sum_{m=1}^{l-n+1} C_{l+1}^{n+m} \frac{(-2e^{\alpha})^{n+m}}{l+1} [a_n b_m + a_m b_n],$$

where C_n^k are the binomial coefficients. Although here we have to perform a triple summation instead of a double summation, regrouping the terms increases the rate of convergence and the series converges even at $w \sim 2$–3.

Relativistic Asymptotics

For the function $f_{\rm ex}$, we also determined the relativistic asymptotics, which is valid either at high temperatures or at high densities, where the kinetic energy of the particles becomes comparable to their rest energy. At high densities and at moderately high temperatures, this asymptotics yields the same result as does Chandrasekhar's expansion given by Kovetz *et al.* (1972):

$$f_{\rm ex}^{\rm rel}(\alpha, w) = \frac{2F_1^2(w)}{\alpha^4} + \frac{S_1(\alpha, w)}{\alpha^2} + S_2(\alpha, w), \quad (4)$$

$$S_1(\alpha, w) = 2F_1(w) \left[q_0 \left(\ln\frac{\alpha}{2} - \frac{1}{2}\right) - I_2(w)\right]$$

$$- \Pi(w) + 2\ln^2(1+e^w) \ln\frac{\alpha}{2},$$

$$S_2(\alpha, w) = \frac{3}{2}\left[q_0\left(\ln\frac{\alpha}{2} - \frac{1}{2}\right) - I_2(w)\right]^2 + \frac{q_0^2}{4}$$

$$- \ln(1+e^w)\left[q_1\left(\ln\frac{\alpha}{2} - 1\right) + I_3(w)\right]$$

$$+ \frac{F_1(w)}{4}\left[q_2\left(\ln\frac{\alpha}{2} - \frac{5}{4}\right) - I_4(w)\right].$$

Here, $F_1(w)$ is the Fermi–Dirac integral of index 1,

$$q_j(w) = (-1)^j \frac{\partial^j}{\partial w^j} \frac{1}{1+e^{-w}},$$

$$I_{j+1}(w) = \frac{\partial^j}{\partial w^j} \int_0^\infty \frac{\ln z}{1+e^{z-w}}\, dz,$$

$$\Pi(w) = 2\int_0^\infty \int_0^\infty \frac{\ln\left|\frac{xy}{x-y}\right| dxdy}{(1+e^{x-w})(1+e^{y-w})}.$$

The double integral $\Pi(w)$ can also be reduced to single integrals:

$$\Pi(w) = 4\ln(1+e^w) I_1(w)$$

$$- 4\int_0^\infty \frac{\ln y\,(e^y \ln(1+e^{w-y}) - \ln(1+e^w))}{e^y - 1}\, dy.$$

THE PATTERN OF THE INTERACTION

We can first approach the problem of the magnitude of the interaction effect in an electron–positron plasma from a general standpoint in order to find out its fundamental pattern and then consider the correlation contribution in detail. The interaction between particles of type i is described by the parameter

$$\Gamma_i = \frac{(Z_i e)^2 [\frac{4\pi}{3} n_i]^{1/3}}{\langle E_i \rangle}. \qquad (5)$$

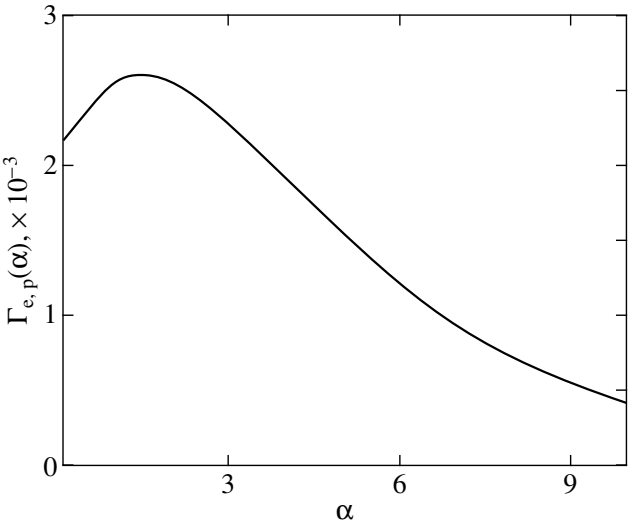

Fig. 1. The dependence $\Gamma_{e,p}(\alpha)$.

Here, n_i is the particle number density, $\langle E_i \rangle$ is their mean kinetic energy; in the absence of degeneracy, $\langle E_i \rangle \sim T$. In the limit $\rho \to 0$,

$$\Gamma_e = \Gamma_p = \Lambda_{fs} \left(\frac{4}{3\pi}\right)^{1/3} \frac{A^{4/3}(\alpha)}{B(\alpha)}. \quad (6)$$

Here, the subscripts "e" and "p" refer to the electrons and positrons, respectively; $\Lambda_{fs} = 1/137.036$ is the fine-structure constant; and $A(\alpha)$ and $B(\alpha)$ are the following integrals:

$$A(\alpha) = \int_0^\infty \frac{\xi^2 d\xi}{1 + \exp(\alpha\sqrt{1+\xi^2})},$$

$$B(\alpha) = \int_0^\infty \frac{\xi^2(\sqrt{1+\xi^2} - 1) d\xi}{1 + \exp(\alpha\sqrt{1+\xi^2})}.$$

Figure 1 shows the $\Gamma_{e,p}(\alpha)$ curve. For $\alpha \to 0$, $\Gamma_{e,p}$ tends to the constant limit $\Lambda_{fs} \left(\frac{4F_2(0)}{3\pi}\right)^{4/3} \frac{90}{7\pi^3} \approx 2.118 \times 10^{-3}$, where $F_2(0) = 1.5\zeta(3) = 1.80308$. For $\alpha \to \infty$, $\Gamma_{e,p}$ exponentially tends to zero as $\Gamma_{e,p} \sim e^{-\frac{\alpha}{3}}/\sqrt{\alpha}$. We see that although the function $\Gamma_{e,p}$ has a maximum of $\Gamma_{e,p} \approx 2.6 \times 10^{-3}$ at $\alpha \sim 1.4$, i.e., at $T \sim 4 \times 10^9$ K, the interaction is generally weak everywhere and, hence, it can be described in a modified Debye–Hückel limit.

The Correlation Part

According to our conclusion that the interaction is weak, it will suffice to take only the first correction to the thermodynamic quantities of the plasma that corresponds to the Debye–Hückel limit, which takes into account the degeneracy of the electron–positron component (Lifshitz and Pitaevskii 2000). In addition, since the electron–positron plasma in the limit $\rho = 0$ is symmetric; i.e., $\sum_i n_i e_i^3 = 0$, where n_i and e_i are the number density and charge of the particles of type i, the next term in the expansion of the thermodynamic quantities in terms of the interaction parameter vanishes (Trubnikov 1996). The correlation contribution to the thermodynamic potential Ω is then

$$\triangle\Omega_{corr} = -\frac{VT\kappa^3}{12\pi}, \quad (7)$$

where κ is a modified inverse Debye length; i.e.,

$$\kappa^2 = 4\pi e^2 \sum_i Z_i^2 \left(\frac{\partial n_i}{\partial \mu_i}\right)_{V,T}. \quad (8)$$

Here, the summation is performed over all types of particles, n_i is the number density of the particles of type i, Z_i is their charge, and μ_i is the chemical potential. Obviously, in the absence of degeneracy, $\partial n_i/\partial\mu_i = n_i/T$ and (8) reduces to the standard Debye expression. We derived an approximation formula for κ:

$$\kappa^2 = \frac{4e^2}{\pi T}\left(\frac{mc}{\hbar}\right)^3 \times \left[\frac{\langle Z^2\rangle}{\langle Z\rangle}\xi + \sqrt{\frac{G(\alpha) + Q(\alpha)\xi^2 + \xi^4}{P(\alpha) + \xi^2}}\right]. \quad (9)$$

Here, we introduced the following quantities: the density parameter

$$\xi = \frac{\langle Z\rangle \rho}{8\pi\langle A\rangle m_u}\left(\frac{h}{mc}\right)^3, \quad (10)$$

where m_u is the atomic mass unit, the temperature functions

$$G(\alpha) = \frac{16J_1^5}{J_2\alpha^4}, \quad Q(\alpha) = \frac{8J_1^2}{\alpha^2}, \quad (11)$$

$$P(\alpha) = \frac{4J_1^3}{J_2\alpha^2},$$

where J_1 and J_2 are the α-dependent integrals:

$$J_1 = \int_0^\infty \frac{1+2\eta^2}{\sqrt{1+\eta^2}} \frac{d\eta}{1 + \exp(\alpha\sqrt{1+\eta^2})}, \quad (12)$$

$$J_2 = \int_0^\infty \frac{1+2\eta^2}{\sqrt{1+\eta^2}} \times \frac{\left(\exp(2\alpha\sqrt{1+\eta^2}) - \exp(\alpha\sqrt{1+\eta^2})\right) d\eta}{\left(1 + \exp(\alpha\sqrt{1+\eta^2})\right)^3}. \quad (13)$$

A few words should be said about the second term of approximation (9), which describes the electron–positron component: at $\xi = 0$, it gives an exact limiting dependence of κ on α; at nonzero densities in the expansion in powers of ξ (the expansion includes only even powers), it also gives an exact temperature dependence of the coefficient of ξ^2 and, for $\alpha \to \infty$, where $J_1 \simeq J_2$, i.e., at low temperatures, it correctly describes the behavior of the term with ξ^4. As the density increases further, this term becomes ξ; i.e., it gives the standard Debye limit. For $\rho \to 0$, the first term in expression (9) for κ, which describes the ion component, vanishes, while the second term reduces to $2J_1/\alpha$.

In addition to the exchange and correlation contributions described above, the peculiar quantum term that describes the features of the particle interaction at distances smaller than the Debye screening length, where the quantum nature of the particles manifests itself, should have also been taken into account. However, as was shown, for example, in the book by Trubnikov (1996), the quantum term is of the order of $\lambda\kappa = \dfrac{\hbar}{p}\kappa$ with respect to the correlation term, i.e., of the order of the ratio of the de Broglie wavelength to the Debye length. In our case, the relative value of this contribution does not exceed several percent, which dispenses with the need for its detailed analysis.

RESULTS OF THE CALCULATIONS

Let us now use the above relations to study the effect of particle–particle interaction on the adiabatic index γ. Pinaeva (1964) considered the behavior of γ in the limit $\rho = 0$ (when $\mu_e = \mu_p = 0$) by disregarding the interaction. In this limit, the numerical effect of the interaction on γ is negligible. However, the fundamental behavior of the $\gamma_{int} - \gamma_{ideal}$ curve shown in Fig. 2 is of considerable interest. The interaction gives a negative contribution to γ up to $T \lesssim 2.4 \times 10^9$ K; i.e., precisely in the range where $\gamma < 4/3$. At high T, γ is larger than 4/3, but the interaction also gives a positive contribution to γ. We can determine the limiting behavior of γ for $T \to \infty$ ($\alpha \to 0$) and compare it with the ideal case (i.e., in the absence of interaction) considered by Blinnikov *et al.* (1996). In the ideal case,

$$\gamma|_{\alpha\to 0} = \frac{4}{3}\left[1 + \frac{5\alpha^2}{22\pi^2}\right]. \qquad (14)$$

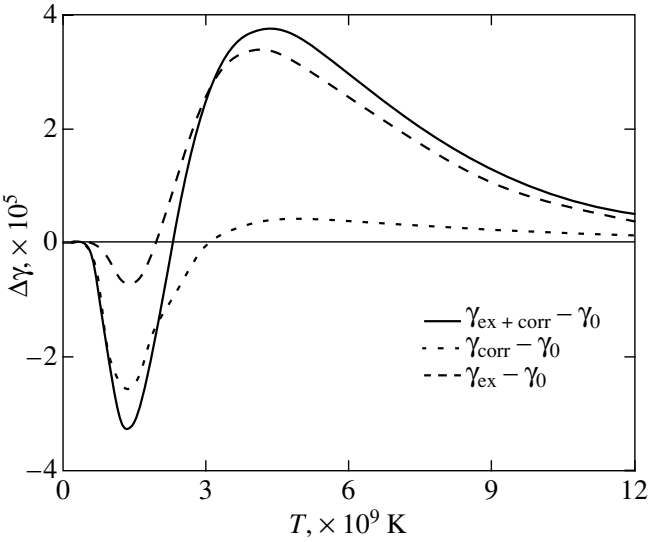

Fig. 2. The dependence $\gamma_{ex+corr} - \gamma_{ideal}$ for the electron–positron component. The dotted line indicates the behavior of $\triangle\gamma$ with an allowance made only for the exchange contribution (dashes) and only for the correlation contribution (dots).

Thus, γ approaches 4/3 as a power law. Allowing for the correlation and exchange interactions yields

$$\gamma|_{\alpha\to 0} = \frac{4}{3}\left[1 + \frac{5\alpha^2}{22\pi^2}\frac{1 + \dfrac{9}{5}\Lambda_{corr} + \dfrac{288}{5\pi^2}\Lambda_{ex}S(\alpha)}{1 + \dfrac{12}{11}(\Lambda_{corr} - \Lambda_{ex})}\right]. \qquad (15)$$

Here, Λ_{corr} and Λ_{ex} are the constants that correspond to the correlation and exchange contributions, respectively:

$$\Lambda_{corr} = 10\left[\frac{\Lambda_{fs}}{3\pi}\right]^{3/2} \simeq 2.15 \times 10^{-4}, \qquad (16)$$

$$\Lambda_{ex} = \frac{15}{144\pi}\Lambda_{fs} \simeq 2.42 \times 10^{-4};$$

$S(\alpha)$ is the following function of α:

$$S(\alpha) = \frac{\pi^2}{12}\left(\ln\frac{\alpha}{2} + 1 - 2I_2(0)\right) \qquad (17)$$

$$- \Pi(0) + 2\left(\ln\frac{\alpha}{2} + \frac{3}{2}\right)\ln^2 2.$$

Although the term with $S(\alpha)$ can asymptotically change the sign of the parameter $\gamma - 4/3$, this could take place at absolutely unattainable temperatures outside the validity range of our formulas, formally at $T \sim 10^{288}$ K.

CONCLUSIONS

Thus, we have found that for all of the reasonably admissible temperatures in the limit of an electron–positron plasma with $\rho = 0$ in equilibrium with blackbody radiation, the interaction effect is negligible (it changes γ only within $\pm 4 \times 10^{-5}$) and changes the sign of $\gamma - 4/3$ nowhere except for the transition region $\gamma \simeq 4/3$ near $T \sim 2.4 \times 10^9$ K.

REFERENCES

1. S. I. Blinnikov, N. V. Dunina-Barkovskaya, and D. K. Nadyozhin, Astrophys. J., Suppl. Ser. **106**, 171 (1996).
2. A. Kovetz, D. Q. Lamb, and H. M. van Horn, Astrophys. J. **174**, 109 (1972).
3. E. M. Lifshitz and L. P. Pitaevskii, *Statistical Physics* (Fizmatlit, Moscow, 2000), Part 2.
4. G. V. Pinaeva, Astron. Zh. **41**, 25 (1964).
5. B. A. Trubnikov, *Plasma Theory* (Énergoatomizdat, Moscow, 1996).

Translated by G. Rudnitskii

Astronomy Letters, Vol. 29, No. 3, 2003, pp. 163–169. Translated from Pis'ma v Astronomicheskiĭ Zhurnal, Vol. 29, No. 3, 2003, pp. 195–201.

What Path the r-Process Takes: Extreme Cases and Comparison with Observations

I. V. Panov*

Institute for Theoretical and Experimental Physics,
ul. Bol'shaya Cheremushkinskaya 25, Moscow, 117259 Russia

Received October 24, 2002

Abstract—The concept of the r-process path is considered from the standpoint of a dynamic model. Rapid nucleosynthesis is shown to proceed not along certain preferential lines called the r-process paths but in the region of nuclei bounded on the one side by the existing nuclei and on the other side by nuclei upon reaching which the r-process enters a cooling phase. This view is shown to account for the main heavy-element abundance patterns. © *2003 MAIK "Nauka/Interperiodica".*

Key words: *nuclear astrophysics, nucleosynthesis, supernovae and supernova remnants.*

INTRODUCTION

The heavy nuclei beyond the iron peak are known to have been produced in nature mostly by neutron-capture reactions (Burbidge *et al.* 1957), with the neutron capture occurring in two extreme cases characterized by different conditions. In the first case, where the β-decay rates are much higher than the rates of the (n, γ) processes, $\lambda_\beta \gg \lambda_{n\gamma}$, the s-process takes place at a neutron density $n_n \sim 10^{16}$ cm^{-3}. Its mechanism is well understood and has been modeled (Käppeler *et al.* 1989). The process passes along the experimentally studied nuclei and its individual stages are well modeled in laboratory, allowing a model to be developed with reliable measurements of key nuclear parameters.

In the other extreme case, before the nucleus undergoes β-decay, a multiple neutron capture by the nucleus (the r-process) takes place. This process proceeds under conditions characterized by high neutron density and temperature, such that $\lambda_\beta \ll \lambda_{n\gamma}$. The nuclei involved in this nucleosynthesis have a large neutron excess and a short lifetime relative to β-decay.

The numerous studies of rapid nucleosynthesis (the r-process) carried out in the past 40 years have adequately determined the conditions required for the heavy nuclei to be synthesized [see, e.g., Käppeler *et. al* (1998) and references therein]. However, the detailed r-process mechanism is not yet completely understood, nor were the astrophysical objects where it could take place ultimately determined. Over these years, many different scenarios have been proposed for the evolution of the various astrophysical objects in which the conditions needed for the r-process to proceed could be realized at some stage. Presently, however, only two of them are more or less physically consistent and are realized in model: the ejection of highly neutronized matter into the interstellar medium in neutron-star mergers during the evolution of close binary systems (Freiburghaus *et al.* 1999a; Lattimer and Schramm 1974; Symbalisty 1982) and the formation of a large number of neutrons in the ejected type-II supernova envelope immediately behind the shock front in the neutrino-heated inner part of the helium shell (Woosley *et al.* 1994; Witti *et al.* 1993).

As we mentioned above, the details of the r-process mechanism are not yet clear, but in recent years, considerable progress has been made in clarifying this issue. The yields of elements obtained in r-process calculations (Freiburghaus *et al.* 1999b) and the observations of old stars (Sneden *et al.* 2000) strongly suggest that there are at least two groups of physical scenarios for the r-process (Wasserburg *et al.* 1996; Qian and Wasserburg 2000). The above scenarios are mostly considered as the main scenarios for the synthesis of elements with atomic masses $A > 120$. Other models, for example, the helium-shell model (Hillebrandt and Thielemann 1977; Truran *et al.* 1978; Truran and Cowan 2000) or the model of rapid nucleosynthesis induced by a neutrino pulse from a collapsing supernova (Epstein *et al.* 1988; Nadyozhin *et al.* 1998), exist to describe the formation of lighter elements.

There are also other, as yet less developed scenarios that were briefly considered by Panov and

*E-mail: Igor.Panov@itep.ru

Chechetkin (2002). In particular, these authors showed that there need not be of the order of 150 neutrons per seed nucleus for the r-process to succeed. The question is what nuclei are seed ones and how they are produced at the nucleosynthesis stage that precedes the r-process. In the presence of a large number of extremely neutron-rich nuclei in the A $\approx$ 130 region, the number of neutrons needed for a successful r-process can be severalfold or even several orders of magnitude smaller. These results have much in common with the results of Cameron (2001). This author considered the possibility of the r-process taking place in accretion disks and jets, showing that a nonstandard approach to such an as yet not completely understood phenomenon as the r-process can yield physically interesting results.

MAIN PROBLEMS OF THE r-PROCESS

Most of the questions that arise when solving the problem of heavy-element formation during rapid nucleosynthesis can be combined mainly into three groups:

(1) The first (main) group includes the following questions: Where and under what conditions does the r-process starts? In what astrophysical objects are the conditions for the r-process realized? What is the scenario that leads to the emergence of necessary conditions and their maintenance for a sufficient time?

(2) The second group includes the questions whose answers give an insight into where the r-process terminates in the first place: What factors cause it to stop? Is it a depletion of free neutrons or a catastrophically rapid decrease in the matter density from the values characteristic of the dense and superdense states of matter to the densities of a rarefied gas? Or is it the fission of transuranium nuclei whose consistent study is just beginning (Panov *et al.* 2001a; Panov and Thielemann 2002)?

(3) The third group includes the problems of determining the dynamics of the change in rapid nucleosynthesis conditions and refining the nuclear-physical properties of nuclei whose solution will make it possible to determine what path the r-process takes in the first place, along what nuclei.

The first group of questions is undoubtedly the most fundamental one, and efforts are focused on their solution.

The main observational data that we have include the observations of the solar heavy-element abundances and the elemental abundances in old metal-poor stars. Strictly speaking, these data are too scarce to determine the objects in which the r-process takes place. However, by solving the direct problem for various, often artificial conditions, we can answer the questions of the second and third groups.

In turn, understanding the dynamic pattern of propagation of the nucleosynthesis wave and determining the most abundant nuclei during the r-process will give a clearer idea of the mechanism of r-process development and termination itself. To this end, some of the questions from the second and third groups may be answered in the near future; there are already preliminary answers to many important questions. Thus, it is already clear from a large number of observations of old stars (Sneden *et al.* 2000; Hill *et al.* 2002) that in one of the main scenarios for the r-process where elements with $120 < A < 240$ are produced, the duration of the r-process τ_r is longer than the so-called cyclic time. The latter is determined by the duration of the r-process from the $A \sim 130$ peak region to the actinide region, in which the various fission processes hamper the formation of nuclei with mass numbers larger than 260 and loop the r-process into the region of nuclei with $A \approx 130$. The most recent data confirm (Panov *et al.* 2001b) that the r-process in the scenarios of neutron-star mergers breaks through fission, in many cases, through induced fission (Panov and Thielemann 2002).

Although the universally accepted view of the r-process path that was introduced in pioneering papers on nucleosynthesis and was successfully used in parametric calculations of direct problems is methodologically useful, it no longer corresponds to the current status of the problem. A new determination of the r-process path, as well as the pattern of propagation of the nucleosynthesis wave, are the subjects of our study.

The concepts and results of the r-process are revised almost continuously as the quality of nuclear data continuously improves [see, e.g., Kratz *et al.* (1998) and references therein] and because of the increasingly consistent searches for astrophysical scenarios of rapid nucleosynthesis (Wasserburg *et al.* 1996; Epstein *et al.* 1988; Cameron 2001).

Here, we investigate the pattern of propagation of the nucleosynthesis wave, which is required to properly choose nuclear data and/or an approach for their calculations.

THE PATH OF THE r-PROCESS

It is clear from the analysis of elemental abundances in nature (Cameron 1982) and from the properties of atomic nuclei that approximately half of the heavy nuclei formed in reactions with neutrons were produced in the r-process and the rest of the nuclei were produced in the s-process. This result unequivocally follows from the shell structure of the atomic

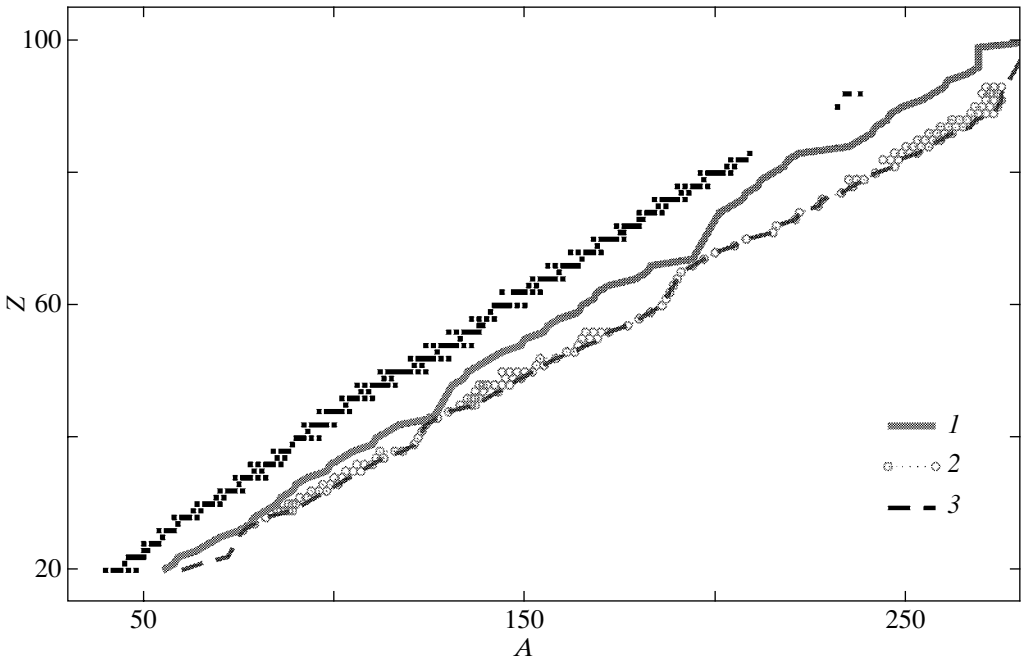

Fig. 1. The path of the r-process (*1*) in the classical model of a static r-process ($S_n \approx 2.2$ MeV) and in the dynamic model (*2*) at the r-process stage for $n_n > 10^{26}$ cm^{-3} ($\tau = 0.3$ s); (*3*) is the neutron stability line.

nuclei, which leads to enhanced abundances of nuclei with filled shells, and has been described repeatedly in the literature.

The solid line in Fig. 1 indicates the typical path of the r-process on the map of nuclei as it is popularly viewed (Kratz *et al.* 1993), where the final r-element abundance is determined by a superposition of the elemental abundances along the various paths along which the conditions for the r-process are mainly unchanged; i.e., nuclei with the same neutron binding energy $S_n = \text{const}$ are formed along each path. Different astrophysical scenarios assume different sets of paths (Kratz *et al.* 1993; Käppeler *et al.* 1989). However, this breakdown is conditional and model-dependent. The view of the dynamic pattern of the r-process (see, e.g., Otsuki *et al.* 2000; Freiburghaus *et al.* 1999b; Panov and Nadyozhin 1999) when the conditions for it change faster than the characteristic duration of the r-process ($\tau_r \gg \tau_\mathrm{h}$), where τ_h is the hydrodynamic time scale that determines the rate of change in rapid nucleosynthesis conditions (Lyutostanskii and Panov 1988), is much more model-independent.

Under such conditions, the path of the r-process is determined quite differently. For definiteness, consider the path of the r-process for the specific model of a neutron star merger (Freiburghaus *et al.* 1999a), which we used when analyzing the various fission channels (Panov *et al.* 2000; Panov and Thielemann 2002). This model gives initial conditions for the r-process characterized by high densities of matter and free neutrons ($n_n \approx 10^{30}$ cm^{-3}). Therefore, at the initial stage, nucleosynthesis proceeds along the neutron stability boundary (circles in Fig. 1).

We clearly see from Fig. 2 that the path of the r-process is displaced toward stable nuclei as the neutron density decreases, while the path of the r-process determined by the most abundant nuclei runs approximately halfway between the region of stable nuclei and the neutron stability line (dotted line), in the region of nuclei with $S_n \approx 2.2$ MeV (Fig. 2b), as n_n decreases to 10^{18} cm^{-3}. Since the pattern rapidly changes, it would be more correct to talk about the region where the r-process proceeds rather than about its path. In that case, the r-process region consists of the nuclei represented by circles and the hatched region of nuclei up to the neutron stability line. Our abundance calculations indicate that under such conditions, the peak positions agree with the observations and there is no need to choose suitable paths (Fig. 3).

During a dynamic r-process, the peak positions on the abundance curve are in excellent agreement with the observations almost for any scenario; depending on the details of the scenario, only the relative yield of the lighter and heavier r elements can change. Thus, Fig. 3 shows our calculations of the dynamic r-process under completely different conditions: for the model of a neutron-star merger (Rosswog *et al.* 1999) and for the model of a hot, rarefied region during

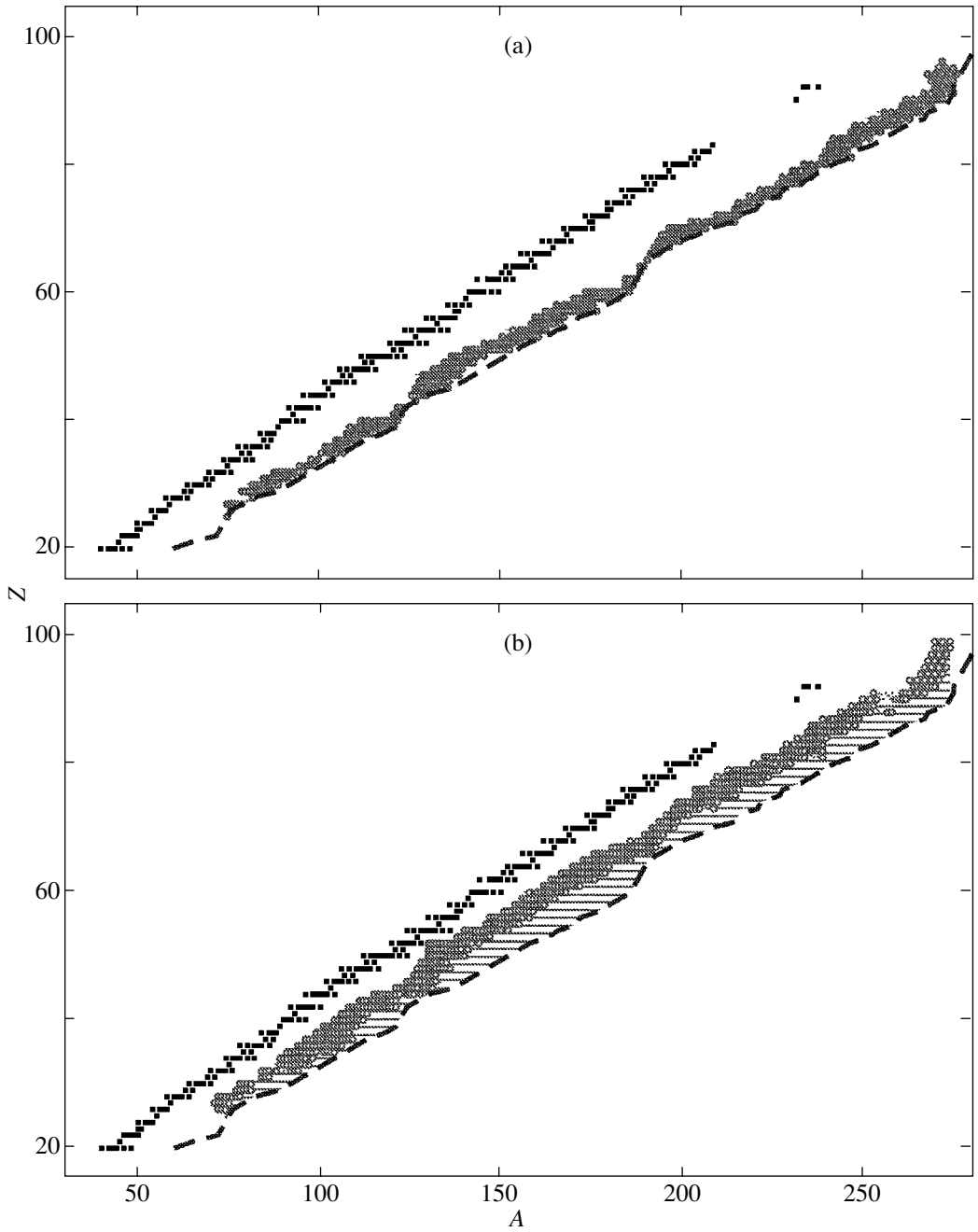

Fig. 2. Change in the path of the r-process as the neutron density n_n decreases: (a) the duration of the r-process $\tau = 0.7$ s, $n_n \sim 10^{22}$ cm^{-3} and (b) $\tau = 1$ s and $n_n \sim 10^{18}$ cm^{-3}. The notation is the same as in Fig. 1.

a supernova explosion, the hot-bubble model (Witti *et al.* 1993). We clearly see that the peak positions and the entire behavior of the abundance curve at $A > 120$ are well described by our calculations. The so-called path of the r-process is the region of the most abundant isotopes of each chemical element, whose location is gradually displaced from the neutron stability boundary (Fig. 2) to the region where the r-process begins to cool down. The rate of this displacement and its specific pattern depend both on the rate of change in the conditions required for nucleosynthesis and on the type and parameters of the object in which the r-process proceeds. Therefore, as is clear from the statement of the problem, the final r-element yield is determined by a weighted superposition of the abundances in one scenario (see., e.g., Woosley *et al.* 1994; Freiburghaus *et al.* 1999b) or by another averaging over the possible variety of scenario

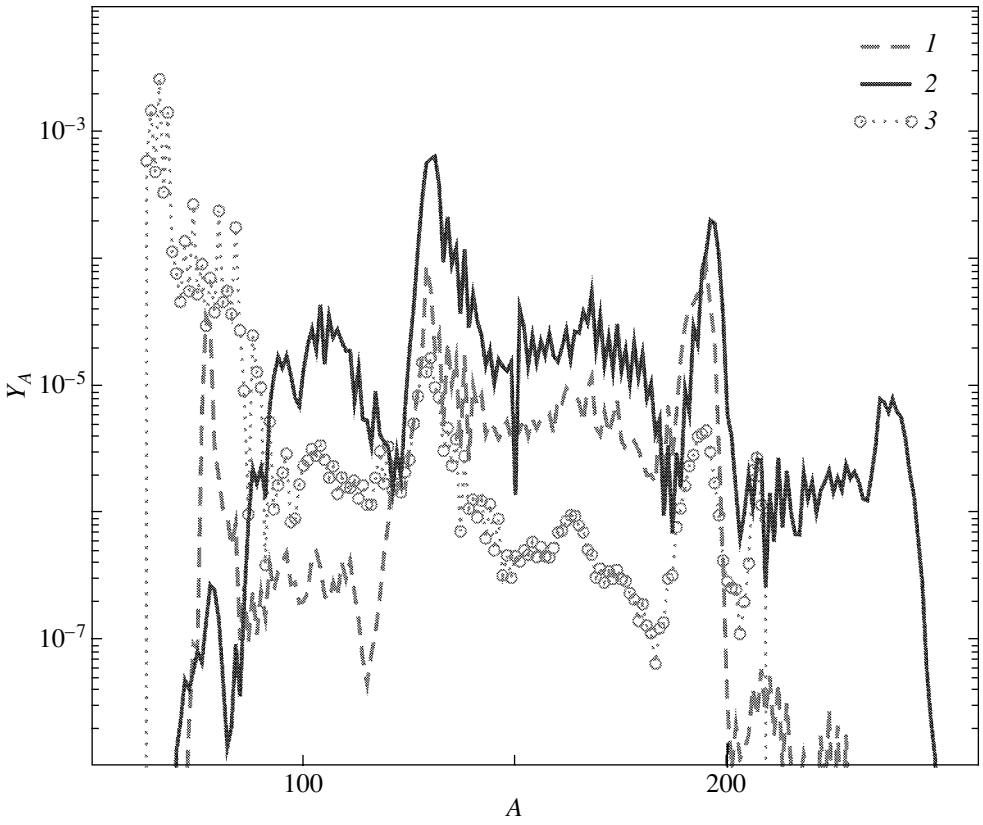

Fig. 3. The computed heavy-element abundances in the model of a neutron star merger (*1*) and in the hot-bubble model (*2*); (*3*) is the the observed elemental abundances in the Solar system (Anders and Grevesse 1989). The normalization of the curves is arbitrary.

objects (e.g., the scenario of a supernova explosion and the formation of heavy elements under the neutrino heating of the medium are realizable during the explosions of supernovae of various masses, which results in a variety of conditions for the r-process).

We obtained all of our results based on calculations with an updated SYNTEZ code (Blinnikov and Panov 1996; Nadyozhin *et al.* 1998). This code has been repeatedly tested (Panov *et al.* 2001a) and used to compute the r-process in various scenarios: a neutron star merger (Panov *et al.* 2000), a type-I supernova explosion (Panov and Chechetkin 2002), and shock passage through a helium shell (Panov and Nadyozhin 1999). All calculations were performed in terms of a full reaction network with an allowance made for the reactions with neutrons; β-decay; fission; and, in the transition cases, at a high temperature and with an allowance made for the pair reactions with protons and α particles. In general, the reaction network included 3076 nuclides from calcium to fermium.

The neutron reaction rates and the partition functions were calculated as prescribed by Thielemann *et al.* (1987) and Cowan *et al.* (1991); the β-decay rates (if no experimental data were available), along with the delayed-neutron emission probabilities were determined from predictions of the QRPA model, which was described in detail by Möller *et al.* (1997). The minimum and maximum values of the mass number A for each Z were specified by the neutron and proton stability boundaries, which were determined from the mass formula. The nuclear masses used were obtained by Kratz *et al.* (1993) with Coulomb corrections and with a more accurate allowance for the pairing effects than that in other mass formulas (Möller and Nix 1992).

CONCLUSIONS AND PROSPECTS

As we see from our typical calculations of the r-process under conditions characteristic of various scenarios (Fig. 3), the dynamic models are in excellent agreement with the observations in peak positions. The question regarding the yields of specific elements and isotopes will be solved as the models are developed further and as an understanding of the process details is reached. However, it is clear that these scenarios can account only for the formation of heavy elements with mass numbers $A > 120$. A

different scenario is probably required to account for the formation of lighter nuclides in the r-process.

Previously, it was assumed that a helium flash in a type-I supernova could give the yields of elements with $A < 120$ (Truran *et al.* 1978; Thielemann *et al.* 1979). However, some number of neutrons required for at least a partial r-process (i.e., the r-process where the nuclei of only one or more new chemical elements can be formed from a seed nucleus) to proceed appear to be produced during the shock passage through a helium or carbon shell, but it is not yet clear whether these and the seed nuclei burn out during the subsequent rise in temperature. The most recent papers (Truran and Cowan 2000; Panov and Nadyozhin 1999) give hope that under certain conditions, the r-process can proceed in these scenarios.

It is clear from our view of the dynamic pattern of the r-process that rapid nucleosynthesis proceeds not along certain preferential lines called the r-process paths but in the region of nuclei bounded on the one side by the boundary of existing nuclei and on the other side by the nuclei upon reaching which the r-process enters a cooling phase. For this reason, the path of the r-process and, hence, the conditions for it, are not strictly preferential but correspond only to one limiting case (as the other extreme case of nucleosynthesis under the effect of neutrons—the s-process): a neutron density $n_n > 10^{18}$ cm^{-3}. Therefore, the resulting abundance curve must be obtained not by a superposition of the various model contributions from nucleosynthesis under constant conditions [a superposition along the various r-process paths determined through $S_n = \text{const}$ (Kratz 1993; Käppeler 1998)] and not randomly, as in the canonical r-process (Goriely and Arnould 1996), but by a superposition in physically distinguishable conditions of the scenarios determined by the uniqueness and variety of astrophysical objects. The path of the r-process determined from nuclei with constant binding energies essentially by double averaging is applicable only to model estimates in the waiting-point approximation or other approximate schemes for the r-process.

Another important result of the new view of the r-process path is the necessity of predicting nuclear data not only for the singled-out nuclei but for virtually all the experimentally poorly studied neutron-rich nuclei. Since these characteristics are difficult to measure, the role of theoretical approaches in studying the nucleosynthesis of heavy nuclei continues to be crucial.

ACKNOWLEDGMENTS

I wish to thank my colleagues, the discussions with whom stimulated the publication of this paper: S.I. Blinnikov, V.S. Imshennik, K.-L. Kratz, K. Langanke, G. Martinez-Pinedo, D.K. Nadyozhin, B. Pfeiffer, T. Rauscher, F.-K. Thielemann, V.M. Chechetkin, and W. Hillebrandt. This study was supported in part by the Russian Foundation for Basic Research (project nos. 00-02-17230 and 00-15-96572).

REFERENCES

1. E. Anders and N. Grevesse, Cosmochimica Acta **53**, 197 (1989).
2. S. I. Blinnikov and I. V. Panov, Pis'ma Astron. Zh. **22**, 39 (1996) [Astron. Lett. **22**, 39 (1996)].
3. G. R. Burbidge, E. M. Burbidge, W. A. Fowler, and F. Hoyle, Rev. Mod. Phys. **29**, 547 (1957).
4. A. G. W. Cameron, Astrophys. Space Sci. **82**, 123 (1982).
5. A. G. W. Cameron, Astrophys. J. **562**, 456 (2001).
6. J. J. Cowan, F.-K. Thielemann, and J. W. Truran, Phys. Rep. **208**, 267 (1991).
7. R. I. Epstein, S. A. Colgate, and W. C. Haxton, Phys. Rev. Lett. **61**, 2038 (1988).
8. C. Freiburghaus, S. Rosswog, and F.-K. Thielemann, Astrophys. J. Lett. **525**, L121 (1999a).
9. C. Freiburghaus, J.-F. Rembges, T. Rausher, *et al.*, Astrophys. J. **516**, 381 (1999b).
10. S. Goriely and M. Arnould, Astron. Astrophys. **312**, 327 (1996).
11. V. Hill, B. Plez, R. Cayrel, *et al.*, Astron. Astrophys. **387**, 560 (2002).
12. W. Hillebrandt and F.-K. Thielemann, Astron. Astrophys. **58**, 357 (1977).
13. F. Käppeler, H. Beer, and K. Wisshak, Rep. Prog. Phys. **52**, 945 (1989).
14. F. Käppeler, F.-K. Thielemann, and M. Wiesher, Annu. Rev. Nucl. Part. Sci. **48**, 175 (1998).
15. K.-L. Kratz, J.-P. Bitouzet, F.-K. Thielemann, *et al.*, Astrophys. J. **403**, 216 (1993).
16. K.-L. Kratz, B. Pfeiffer, and F.-K. Thielemann, Nucl. Phys. A **630**, 352 (1998).
17. J. M. Lattimer and D. N. Schramm, Astrophys. J. Lett. **192**, L145 (1974).
18. Yu. S. Lyutostanskii and I. V. Panov, Pis'ma Astron. Zh. **14**, 168 (1988) [Sov. Astron. Lett. **14**, 70 (1988)].
19. P. Möller and J. R. Nix, Nucl. Phys. A **536**, 20 (1992).
20. P. Möller, J. R. Nix, and K.-L. Kratz, At. Data Nucl. Data Tables **66**, 131 (1997).
21. D. K. Nadyozhin, I. V. Panov, and S. I. Blinnikov, Astron. Astrophys. **335**, 207 (1998).
22. K. Otsuki, H. Tagoshi, T. Kajino, and S. Wanajo, Astrophys. J. **533**, 424 (2000).
23. I. V. Panov and D. K. Nadyozhin, Pis'ma Astron. Zh. **25**, 435 (1999) [Astron. Lett. **25**, 369 (1999)].
24. I. V. Panov and F.-K. Thielemann, *Nuclei in the Cosmos VII*, Ed. by S. Kubono (Fuji-Yoshida, Japan, 2002), in press.
25. I. V. Panov and V. M. Chechetkin, Pis'ma Astron. Zh. **28**, 541 (2002) [Astron. Lett. **28**, 476 (2002)].

26. I. V. Panov, C. Freiburghaus, and F.-K. Thielemann, *Workshop on Nuclear Astrophysics*, Ed. by W. Hillebrandt and E. Muller (Ringberg, Garching, 2000), p. 73.
27. I. V. Panov, S. I. Blinnikov, and F.-K. Thielemann, Pis'ma Astron. Zh. **27**, 248 (2001a) [Astron. Lett. **27**, 239 (2001a)].
28. I. V. Panov, C. Freiburghaus, and F.-K. Thielemann, Nucl. Phys. A **688**, 587 (2001b).
29. Y.-Z. Qian and G. J. Wasserburg, Phys. Rep. **333**, 77 (2000).
30. S. Rosswog, M. Liebendörfer, F.-K. Thielemann, *et al.*, Astron. Astrophys. **341**, 499 (1999).
31. C. Sneden, J. J. Cowan, I. I. Ivans, *et al.*, Astrophys. J. Lett. **533**, L139 (2000).
32. E. M. D. Symbalisty and D. N. Schramm, Astrophys. Lett. **22**, 143 (1982).
33. F.-K. Thielemann, M. Arnould, and W. Hillebrandt, Astron. Astrophys. **74**, 175 (1979).
34. F.-K. Thielemann, M. Arnould, and W. Truran, *Advances in Nuclear Astrophysics*, Ed. by E. Vangioni-Flam *et al.* (Editions Frontiers, Gif sur Yvette, 1987), p. 525.
35. J. W. Truran and J. J. Cowan, *Workshop on Nuclear Astrophysics*, Ed. by W. Hellebrandt and E. Muller (Ringberg, Gardching, 2000), p. 64.
36. J. W. Truran, J. J. Cowan, and A. G. W. Cameron, Astrophys. J. Lett. **222**, L63 (1978).
37. G. J. Wasserburg, M. Busso, and R. Gallino, Astrophys. J. Lett. **466**, L109 (1996).
38. J. Witti, H.-Th. Janka, K. Takahashi, and W. Hillebrandt, *Nuclei in the Cosmos*, Ed. by F. Käppeler and K. Wisshak (Inst. of Phys. Publ., Bristol and Philadelphia, 1993), p. 601.
39. S. E. Woosley, J. R. Wilson, G. J. Mathews, *et al.*, Astrophys. J. **433**, 229 (1994).

Translated by V. Astakhov

Astronomy Letters, Vol. 29, No. 3, 2003, pp. 170–174. Translated from Pis'ma v Astronomicheskiĭ Zhurnal, Vol. 29, No. 3, 2003, pp. 202–207.

Radiation of Magnetoacoustic Waves in the Interstellar Medium by Physical Variable Stars

V. P. Dokuchaev*

Nizhni Novgorod State University, pr. Gagarina 23, Nizhni Novgorod, 630600 Russia

Received January 17, 2002

Abstract—Radially pulsating stars are shown to radiate fast and slow magnetoacoustic waves into the interstellar gas. No Alfvén waves are excited, because the oscillations are radially symmetric. Calculations were performed for the following two limiting cases: hot, weakly magnetized interstellar plasma and cold plasma with a strong magnetic field. In these limiting cases, pulsating stars excite mostly fast magnetoacoustic waves, while the excitation of slow magnetoacoustic waves is weak. Magnetogasdynamic fields of density, velocity, and magnetic-field perturbations in the interstellar medium were found. Relations were derived to calculate the radiated power and its estimates are given for various conditions in the medium. It is shown that radially stratified wave structures with wavelengths from 1 AU to several tenths of a parsec must exist in the vicinity of pulsating stars. © *2003 MAIK "Nauka/Interperiodica"*.

Key words: *physical variable stars, magnetic gas-dynamics, pulsations, waves, radiation power.*

INTRODUCTION

First, the excitation and propagation of low-frequency magnetogasdynamic waves have a direct bearing on the formation and dynamics of the space-time cloud structure of the interstellar gas. Second, the radiation of these waves is accompanied by the loss of part of the stellar internal energy. Thus, the problems of the radiation of magnetoacoustic and Alfvén waves are of considerable interest in the physics of both stars and the interstellar medium. Inhomogeneity of the interstellar gas strongly affects the propagation of high-frequency electromagnetic waves from optical to radio wavelengths (see, e.g., Kaplan and Pikel'ner 1979). The clouds and dynamical processes in the interstellar gas owe their origin mainly to turbulent flows and gas convection (Vainshtein *et al*. 1990). The interaction of stars with the interstellar gas plays an important role in forming the inhomogeneous and nonstationary structure of interstellar cosmic plasma. Shock waves near moving stars and planets were described by Vainshtein *et al*. (1990) and Bochkarev (1990). Far from the stars, these shock waves degenerate into low-amplitude magnetoacoustic and Alfvén waves, which carry away the energy and momentum of the moving stars into the ambient medium (Dokuchaev 1964).

Here, we consider a new mechanism of interaction between pulsating variable stars and the ambient interstellar gas. We disregard the motion of the stars with a constant velocity relative to the ambient gas. Allowance for this effect would severely complicate the pattern of basic parameters of the new interaction mechanism. The approximation of collisionless magnetic gas-dynamics is used to describe the interaction. The interstellar medium is a strongly ionized gas in the general Galactic magnetic field. The slow (in time) and large-scale processes in magnetoactive cosmic plasma are commonly described in the magnetogasdynamic approximation. Other methods of describing the interaction of stars with the ambient gas are also possible (Vainshtein *et al*. 1990). A high percentage of physical variable stars with periodic radial pulsations have characteristic frequencies ω in the range (Cox 1976)

$$10^{-7} < \omega < 10^{-4}\ \mathrm{s}^{-1}, \qquad (1)$$

where the lower and upper limits correspond to the long-period Mira Ceti and RR Lyrae variables, respectively. The frequency range (1) satisfies the criterion of applicability of the magnetogas-dynamic approximation (see, e.g., Syrovatskiĭ 1957):

$$\omega \ll \omega_{Bi} = \frac{eB_0}{m_i c}, \qquad (2)$$

where ω_{Bi} is the gyroscopic frequency of the ions with mass m_i, e is the ion electric charge, c is the speed of light in a vacuum, and B_0 is the mean magnetic induction. For hydrogen plasma at $B_0 = 10^{-6}$ G, we find that $\omega_{Bi} = 10^{-2}$ rad s^{-1}. Thus, criterion (2) holds good in the frequency range (1).

*E-mail: vpd@rf.unn.runnet.ru

1063-7737/03/2903-0170$24.00

Here, the mathematical model of the wave radiation mechanism is based on the standard acoustic model of sound generation in a gas by a radially pulsating elastic sphere with a mean radius a_0 and a radial pulsation amplitude a_1. In other words, we assume that the displacement of the interstellar gas on some reference surface with radius a is described by a simple harmonic function:

$$a(t) = a_0 + a_1 \sin \omega t, \quad a_1 \ll a_0. \tag{3}$$

Here, the frequency $\omega = 2\pi/\Pi$, where Π is the pulsation period, which is measured by observing luminosity variations in variable stars. The oscillation amplitude a_1 is also determined for the photospheres of variable stars and accounts for 10–15% of the stellar radius R_s. However, according to current views of the self-oscillation mechanism for stellar pulsations, the gas perturbations inside the photospheres and even in the coronas of these stars are large and the linear theory of wave radiation is inapplicable. Therefore, we suggest using a sphere with the radius of the stellar supercorona as the boundary a_0. We determine this radius at a distance from the stellar center at which the speed of sound in the interstellar gas surrounding the star is comparable to the parabolic escape velocity of the hydrogen atoms from the gravitational field of a star with mass M_s:

$$\dot{a}_0 = R_{sc} = \frac{2GM_s}{c_s^2}, \tag{4}$$

where G is the gravitational constant and c_s is the mean thermal velocity of the interstellar atoms (the speed of sound). Assuming that $c_s = \kappa T/m_p$, where κ is the Boltzmann constant, m_p is the proton mass, and T is the gas temperature, and substituting the fundamental constants into (4), we obtain

$$a_0 = \left(\frac{M_s}{M_\odot T}\right) \text{ pc}. \tag{5}$$

Here, T should be substituted in kelvins. The radial pulsations of variable stars are currently believed to be caused by nonlinear self-oscillations of the gas layer beneath the photosphere where the regions of singly and doubly ionized helium are located (see, e.g., Cox 1976). As one recedes into the upper stellar atmospheres, the perturbations in the plasma must weaken and the oscillatory–wave processes become weak at the outer coronal boundary at $R = a_0$ (4) and (5). These can be determined in the approximation of linear magnetohydrodynamics. Note that both the quasi-harmonic radial pulsation frequency ω and the supercorona boundary oscillation amplitude a_1 are determined by the physical conditions in the lower dense stellar photospheric layers where the nonlinear self-oscillation mechanism of these layers is acting. Below, we assume that the supercorona boundary oscillation frequency is equal to the photospheric brightness pulsation frequency and that the relative variations ($a_1/a_0 \simeq 0.1$) are constant in the corona and the photosphere.

STATEMENT OF THE PROBLEM OF THE RADIATION OF MAGNETOGASDYNAMIC WAVES

We proceed from the system of magnetogasdynamic equations for a single-fluid magnetoactive plasma (Aleksandrov *et al.* 1978)

$$\rho\left[\frac{\partial \mathbf{v}}{\partial t} + (\mathbf{v}\nabla)\mathbf{v}\right] = -c_s^2 \text{grad}\,\rho - \frac{1}{4\pi}(\mathbf{B} \times \text{curl}\,\mathbf{B}), \tag{6}$$

$$\frac{\partial \rho}{\partial t} + \text{div}\,\rho\mathbf{v} = 0, \tag{7}$$

$$\frac{\partial \mathbf{B}}{\partial t} = \text{curl}(\mathbf{v} \times \mathbf{B}), \tag{8}$$

$$\text{div}\,\mathbf{B} = 0. \tag{9}$$

Here, ρ is the plasma mass density, $\mathbf{v}$ is the velocity of the medium, $\mathbf{B}$ is the magnetic induction vector, and c_s is the speed of ion sound. Equations (6) and (7) express the momentum and mass conservation laws, respectively; Eq. (8) expresses the Faraday induction law for a moving gas. Let us linearize system (6)–(9) by assuming that the following conditions are satisfied:

$$\rho = \rho_0 + \rho_1(R,t), \quad \rho_1 \ll \rho_0; \tag{10}$$

$$\mathbf{B} = \mathbf{B}_0 + \mathbf{B}_1(R,t), \quad \mathbf{B}_1 \ll \mathbf{B}_0; \tag{11}$$

$$|\mathbf{v}| = |\mathbf{v}_1(R,t)| \ll c_s, \tag{12}$$

where ρ_0 and $\mathbf{B}_0$ are the mean constant (in space and in time) fields; and ρ_1, $\mathbf{B}_1$, and $\mathbf{v}_1$ are small perturbations. Thus, we finally obtain from (6)–(9)

$$\frac{\partial^2 \mathbf{v}_1}{\partial t^2} = (c_A^2 + c_s^2)\text{grad}\,\text{div}\,\mathbf{v}_1 - c_A^2(\mathbf{b}\nabla)(\mathbf{B}_0 \times \text{curl}\,\mathbf{v}_1 + \mathbf{b}\,\text{div}\,\mathbf{v}_1), \tag{13}$$

$$p_1 = c_s^2\rho_1, \qquad c_s^2 = \frac{dp}{d\rho}, \tag{14}$$

where p_1 are the pressure perturbations in the gas. Here, we use the designation c_A for the Alfvén velocity and a unit vector $\mathbf{b}$ along the magnetic field $\mathbf{B}_0$ lines,

$$c_A = \frac{B_0}{\sqrt{4\pi\rho_0}}, \qquad \mathbf{b} = \frac{\mathbf{B}_0}{B_0}. \tag{15}$$

Equation (13) describes the small perturbations of the following three types of normal waves that exist in magnetoactive plasma: Alfvén, fast magnetoacoustic,

and slow magnetoacoustic waves. Indeed, if we seek a solution to Eq. (13) in the form of a plane wave

$$\mathbf{v}_1 = \mathbf{v}_0 \exp(i\omega t - i\mathbf{kR}), \tag{16}$$

where $\mathbf{v}_0$ is the velocity amplitude, ω is the frequency, and $\mathbf{k}$ is the wave vector, then we find the dispersion relations for these types of normal waves in the medium and the phase velocities from (18):

$$u_\mathrm{A} = \frac{\omega}{k} = c_\mathrm{A}\left(\frac{\mathbf{b}_0\mathbf{k}}{k}\right), \quad \mathbf{b}_0 = \mathbf{B}_0/B_0, \tag{17}$$

$$u_\pm^2 = \frac{\omega^2}{k^2} = \frac{c_\mathrm{A}^2 + c_\mathrm{s}^2 \pm \sqrt{(c_\mathrm{A}^2 + c_\mathrm{s}^2)^2 - 4c_\mathrm{A}^2 c_\mathrm{s}^2 \cos^2\theta}}{2}. \tag{18}$$

Here, u_A is the phase velocity of the Alfvén wave and $u_\pm$ are the phase velocities of the fast (+) and slow (−) magnetoacoustic waves in plasma. In formulas (17), $(\mathbf{kb}_0) = k\cos\theta$, where θ is the angle between the vectors $\mathbf{k}$ and $\mathbf{b}_0$. We see from relations (17) and (18) that, in general, the problems of the radiation of the above waves are difficult to solve analytically, because the wave properties of the medium are anisotropic. Therefore, we use here two additional approximations. First, we consider the case $c_\mathrm{s} \gg c_\mathrm{A}$ where it follows from (17) and (18) that

$$u_\mathrm{A} = c_\mathrm{A}\cos\theta, \quad u_+ = c_\mathrm{s}, \quad u_- = c_\mathrm{A}\cos\theta; \tag{19}$$

i.e., the fast magnetoacoustic wave propagates in plasma isotropically in all directions with the speed of sound, while the Alfvén and slow magnetoacoustic waves have the same angle-dependent phase velocities. In the second limiting case where $c_\mathrm{A} \gg c_\mathrm{s}$, we find from (17) and (18) that

$$u_\mathrm{A} = c_\mathrm{A}\cos\theta, \quad u_+ = c_\mathrm{A}, \quad u_- = c_\mathrm{s}\cos\theta. \tag{20}$$

Here, the fast wave again has an isotropic velocity of propagation, while the slow and Alfvén waves are anisotropic. There is reason to believe that the case $c_\mathrm{A} = c_\mathrm{s} = u_0$, where

$$u_\mathrm{A} = u_0\cos\theta, \quad u_\pm = u_0\sqrt{1 \pm \sin\theta} \tag{21}$$

is of the greatest interest in the physics of the interstellar medium.

However, as we will see from the subsequent analysis, comparatively simple results can be obtained only in the purely acoustic approximation and for strongly magnetized plasma. In the case of purely radial pulsations, since the radiation conditions are symmetric, stars excite mostly fast magnetoacoustic waves.

A PULSATING STAR AS A RADIATOR OF MAGNETOACOUSTIC WAVES

Suppose that the medium near a pulsating star is homogeneous and is in an external uniform galactic magnetic field. The star is assumed to undergo purely radial pulsations. It is clear from the symmetry of the problem that no vortex (rotational) Alfvén waves will be radiated in this case. We use a cylindrical system of r, ϕ, z coordinates with its origin located at the stellar center. Obviously, the velocity components v_r, v_ϕ, and v_z, by symmetry, do not depend on the polar angle ϕ, and Eq. (13) gives

$$\frac{\partial^2 v_r}{\partial t^2} = c_\mathrm{A}^2\frac{\partial^2 v_r}{\partial z^2} + (c_\mathrm{A}^2 + c_\mathrm{s}^2)\frac{\partial}{\partial r}\left(\frac{1}{r}\frac{\partial r v_r}{\partial r}\right) + c_\mathrm{A}^2\frac{\partial^2 v_z}{\partial r \partial z}, \tag{22}$$

$$\frac{\partial^2 v_\phi}{\partial t^2} = c_\mathrm{A}^2\frac{\partial^2 v_\phi}{\partial z^2}, \tag{23}$$

$$\frac{\partial^2 v_z}{\partial t^2} = c_\mathrm{s}^2\frac{\partial}{\partial z}\left[\frac{\partial v_z}{\partial z} + \frac{1}{r}\frac{\partial (r v_r)}{\partial r}\right]. \tag{24}$$

It thus follows that during radial pulsations, the gas velocities on the stellar (photospheric) surface and in the entire surrounding space are $u_\phi = 0$. We analyze the interstellar plasma perturbations in magnetoacoustic waves for the two limiting cases. The acoustic case (19) with $c_\mathrm{A} = 0$ is simplest and reduces to the problem of the radiation of acoustic waves by a radially pulsating elastic sphere (see, e.g., Landau and Lifshitz 1986). In this case, it is convenient to change to the spherical coordinates R, θ, ϕ and to directly use Eq. (13) with $c_\mathrm{A} = 0$. The figure schematically shows the pulsating star and the cylindrical and spherical coordinate systems. According to (3), the boundary condition for a radially pulsating elastic shell is

$$v_R = \frac{da}{dt} = v_1 e^{i\omega t} \quad \text{for} \quad a = a_0. \tag{25}$$

Here, $v_1 = a_1\omega$ is the velocity amplitude and the pulsation velocity $v_R(a_0, t)$ is written in complex exponential form. Thus, the solution of Eq. (13) for the velocity component v_R at $c_\mathrm{A} = 0$ with the boundary condition (25) is

$$v_1 = v_0\frac{a_0^2}{R^2}\frac{1 + ik_\mathrm{s}R}{1 + ik_\mathrm{s}a_0}e^{i\omega\left(t - \frac{R - a_0}{c_\mathrm{s}}\right)}, \tag{26}$$

where $k_\mathrm{s} = \omega/c_\mathrm{s}$ is the acoustic wave number. The time-averaged wave radiation energy flux density is given by the expression (Landau and Lifshitz 1986)

$$\Pi_R = \frac{1}{2}p_1 v_1^* = \frac{\rho_0\omega^2 v_0^2 a_0^4}{2c_\mathrm{s}(1 + k_\mathrm{s}^2 a_0^2)}\frac{1}{R^2}, \tag{27}$$

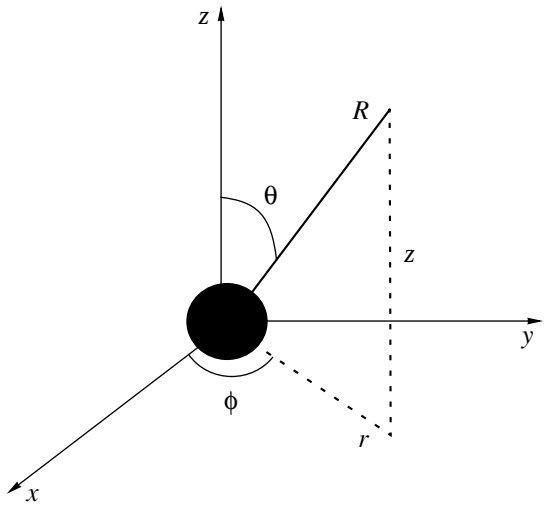

Figure.

where (*) denotes a complex conjugate. We see from (27) that the radiation is monopole in pattern, because the energy flux does not depend on θ and ϕ (an isotropic radiation pattern). The total radiation power W can be determined from (27) by integration over the solid angle $d\Omega = \sin\theta d\theta d\varphi$ on a sphere of radius R. It can be represented as

$$W = \frac{2\pi\rho_0\omega^2 v_0^2 a_0^4}{c_\mathrm{s}(1+k_\mathrm{s}^2 a_0^2)} \tag{28}$$

$$= W_\mathrm{s}\begin{cases}(k_\mathrm{s}a_0)^2 & \text{for} \quad (k_\mathrm{s}a_0) \ll 1,\\ 1 & \text{for} \quad (k_\mathrm{s}a_0) \gg 1,\end{cases}$$

$$W_\mathrm{s} = \frac{(\rho_0 c_\mathrm{s})v_0^2 S_0}{2}, \qquad S_0 = 4\pi a_0^2. \tag{29}$$

Here, for convenience, we use the designation W_s for the power of the "piston" radiation from a pulsating sphere with area S_0 and with a large acoustic radius, $(k_\mathrm{s}a_0) \gg 1$. The wave impedance of the medium for acoustic waves is given in (29) in parentheses.

We also consider the case of strongly magnetized plasma where $c_\mathrm{A} \gg c_\mathrm{s}$ (20) under the assumption of $c_\mathrm{s} \simeq 0$. The velocity component v_{z1} in the cylindrical coordinate system is related to the radiation of a slow magnetoacoustic wave and gives no appreciable contribution to the total radiation energy. In other words, in this case, a pulsating shell also mainly radiates a fast magnetoacoustic wave with the phase velocity c_A (20). The boundary condition for the velocity component v_{r1} is

$$v_{r1} = v_0 \sin\theta e^{i\omega t} \quad \text{for} \quad R = a_0. \tag{30}$$

The solution of the boundary-value problem for Eqs. (23)–(25) at $c_\mathrm{s} = 0$ with condition (30) yields the relations

$$v_{r1} = v_0\left(\frac{a_0}{R}\right)^2 \frac{1+ik_\mathrm{A}R}{1+ik_\mathrm{A}a_0}\sin\theta e^{i\omega\left(t-\frac{R-a_0}{c_\mathrm{A}}\right)}, \tag{31}$$

$$B_{r1} = B_0\left(\frac{v_0}{c_\mathrm{A}}\right)\left(\frac{a_0}{R}\right)^2 \times \frac{1+ik_\mathrm{A}R}{1+ik_\mathrm{A}a_0}\sin\theta\cos\theta e^{i\omega\left(t-\frac{R-a_0}{c_\mathrm{A}}\right)}, \tag{32}$$

$$\rho_1 = \rho_0\left(\frac{v_0}{\omega R}\right)\frac{(k_\mathrm{A}a_0)^2\sin^2\theta}{1+ik_\mathrm{A}a_0}e^{i\omega\left(t-\frac{R-a_0}{c_\mathrm{A}}\right)}, \tag{33}$$

$$B_{z1} = B_0\left(\frac{\rho_1}{\rho_0}\right), \tag{34}$$

where $k_\mathrm{A} = \omega/c_\mathrm{A}$ is the wave number. In this case, the energy flux density can be calculated by using the formula

$$\mathbf{\Pi} = \frac{1}{4\pi}\mathbf{B}_1 \times (\mathbf{B}_0 \times \mathbf{v}_1). \tag{35}$$

After averaging over the pulsation period, we find for the radial Poynting vector component that

$$\Pi_R = \frac{\rho_0 c_\mathrm{A} v_0^2}{2}\left(\frac{a_0}{R}\right)^2 (k_\mathrm{A}a_0)^2\frac{\sin^2\theta}{(1+k_\mathrm{A}^2 a_0^2)}. \tag{36}$$

Here, in contrast to (27), the radiation intensity depends on θ and the radiation has a dipole pattern. The total radiation power is given by the integral

$$W = R^2\int_0^{2\pi}\int_0^{\pi}\Pi_R\sin\theta d\theta d\varphi. \tag{37}$$

Substituting relation (36) into (37) yields

$$W = W_m\begin{cases}(k_\mathrm{A}a_0)^2 & \text{for} \quad (k_\mathrm{A}a_0) \ll 1,\\ 1 & \text{for} \quad (k_\mathrm{A}a_0) \gg 1,\end{cases} \tag{38}$$

Here, W_m is the power of the "piston" radiation of a fast magnetoacoustic wave:

$$W_m = \frac{1}{3}(\rho_0 c_\mathrm{A})v_0^2 S_0, \tag{39}$$

where S_0 is the surface area of the stellar supercorona. Relations (28), (29) and (38), (39) allow us to estimate the power of the radiation of fast magnetoacoustic waves by pulsating variable stars. Note that these relations are similar in structure; the influence of the medium is determined by the characteristic impedances $\rho_0 c_\mathrm{s}$ and $\rho_0 c_\mathrm{A}$. Below, we give estimates for classical Cepheids with the frequency $\omega = 10^{-5}$ s^{-1}, radius $R_\mathrm{s} = 10\,R_\odot$, and mass $M_\mathrm{s} = 10\,M_\odot$. Let us first consider the case where the star is surrounded by hot, rarefied, and weakly magnetized plasma: $T = 1000$ K, $\rho_0 = 10^{-24}$ g cm^{-3}, and $B_0 = 10^{-7}$ G. We find that $a_0 = 0.01$ pc, $c_\mathrm{s} = 3$ km s^{-1},

and $c_A = 0.3$ km s^{-1}; i.e., $c_s \gg c_A$ and $(k_s a_0) \gg 1$. Consequently, relation (29) should be used for our estimates. At $v_0 = 1$ km s^{-1}, we obtain the radiated power (acoustic luminosity) of the pulsating star, $W_s = 10^{24}$ erg s^{-1}. In the other limiting case of a cold ($T = 10$ K), dense ($\rho = 10^{-23}$ g cm^{-3}) cloud with a strong magnetic field, $B_0 = 3 \times 10^{-6}$ G, $c_A = 3$ km s^{-1}, and $c_s = 0.3$ km s^{-1}; $c_A \gg c_s$ and $k_A a_0 \gg 1$. In this case, we obtain the radiation power of a fast magnetoacoustic wave from (39), $W_m = 10^{30}$ erg s^{-1}. Cox (1976) gave the decay times τ_d for typical pulsating stars. In our case, $\tau_d = (2\pi/\omega) \times 10^3$ s and the total maximum energy of the radiative losses through the radiation of fast magnetoacoustic waves is $\varepsilon = \tau_d W_m = 10^{39}$ erg. This value is much smaller than the total store of thermal energy in the star. The radiation of magnetoacoustic waves by regular variable stars has no significant effect on the total mean energy balance of the interstellar gas dynamics in galaxies, because the space density of these stars is low (Cox 1976).

CONCLUSIONS

Radially pulsating physical variable stars produce wave disturbances in the ambient interstellar gas that are described by a system of magnetogasdynamic equations. Stars with purely radial pulsations were shown to generate fast and slow magnetoacoustic waves. The phase and group velocities of these waves depend on the direction of their propagation and on the magnitudes of the two main velocities in plasma—the speed of ion sound c_s and the Alfvén speed c_A. If one of these velocities is much higher than the other, then the corresponding boundary-value problem of the wave radiation by a radially pulsating elastic sphere can be solved completely. In this case, the bulk of the radiation energy was shown to be carried away from the star by fast magnetoacoustic waves. We focused our attention on the analysis of radiation energy parameters—the radiation intensity and total power. We established that for $c_s \gg c_A$, mostly acoustic (density) waves with an isotropic radiation pattern are radiated. In the other limiting case, $c_A \gg c_s$, mostly fast magnetoacoustic waves with a dipole radiation pattern are radiated. In this case, the radiation field is concentrated in the plane that passes through the center of the pulsating star and that is perpendicular to the magnetic field lines. In both cases, slow magnetoacoustic waves give a minor contribution to the radiated energy. We estimated the radiation power. Thus, pulsating variable stars produce a stratified wave structure in the ambient interstellar gas with mean magnetoacoustic wave lengths

$$1 \text{ AU} \leq \lambda \leq 0.01 \text{ pc}, \qquad (40)$$

which slowly travel in the radial direction. It is clear from inequality (40) that the scales of these regular wave inhomogeneities in the interstellar medium are small and that they can be detected near variable stars only by indirect methods. However, the radiation power of these waves can, in principle, affect the rate of thermal energy losses from the layers of singly and doubly ionized helium beneath the stellar photosphere and, eventually, the duration of the self-oscillation regime in the helium shells of variable stars. The motion of a star in space must be accompanied by the Doppler effect and by the radiation of Mach waves both during accretion and during a stellar wind (Dokuchaev 1964). However, these wave generation mechanisms result mainly in translational energy losses through radiation and are not considered here in detail.

REFERENCES

1. A. F. Aleksandrov, L. S. Bogdankevich, and A. A. Rukhadze, *The Basics of Plasma Electrodynamics* (Vysshaya Shkola, Moscow, 1978).
2. N. G. Bochkarev, *Local Interstellar Medium* (Nauka, Moscow, 1990).
3. J. P. Cox, *Stellar Pulsation Theory* (Mir, Moscow, 1976), Vol. 2.
4. V. P. Dokuchaev, Astron. Zh. **41**, 33 (1964).
5. S. A. Kaplan and S. B. Pikel'ner, *Physics of Interstellar Medium* (Nauka, Moscow, 1979).
6. L. D. Landau and E. M. Lifshitz, *Course of Theoretical Physics,* Vol. 6: *Fluid Mechanics* (Nauka, Moscow, 1986; Pergamon, New York, 1987).
7. S. I. Syrovatskiĭ, Usp. Fiz. Nauk **62**, 247 (1957).
8. S. I. Vainshtein, A. M. Bykov, and I. N. Toptygin, *Turbulence, Current Streams, and Shock Waves in Cosmic Plasma* (Nauka, Moscow, 1990).

Translated by V. Astakhov

Astronomy Letters, Vol. 29, No. 3, 2003, pp. 175–187. Translated from Pis'ma v Astronomicheskiĭ Zhurnal, Vol. 29, No. 3, 2003, pp. 208–222.

Fast Line-Profile Variability in the Spectra of O Stars

A. F. Kholtygin[1]*, D. N. Monin[2], A. E. Surkov[2], and S. N. Fabrika[2]

[1] *Astronomical Institute, St. Petersburg State University, Universitetskiĭ pr. 28, Petrodvorets, 198904 Russia*

[2] *Special Astrophysical Observatory, Russian Academy of Sciences, Nizhni Arkhyz, Karachaĭ-Cherkessian Republic, 357147 Russia*

Received October 14, 2002

Abstract—A program of the search for and analysis of profile variability in the spectra of bright O supergiants with a time resolution of 5–30 min is described. Preliminary results of the spectroscopic observations of the stars λ Ori, α Cam, and 19 Cep with the 1-m Special Astrophysical Observatory telescope in 2001 are presented. Line-profile variability was detected in the spectra of all the stars studied; variability in the Hα and C III λ5696 Å lines in the spectrum of λ Ori has been found for the first time. The variability amplitude is 4–5% for 19 Cep and 1–2% for α Cam and λ Ori on time scales from several hours to 3 or 4 days, and the width of the variable features reaches 2 Å (100 km s^{-1}). We detected cyclical variations in the He II λ4686 and C III λ5696 line profiles in the spectrum of λ Ori on time scales of 1.3–1.6 days. Rapid profile variations on time scales of 3.5–7 h were found in the violet parts of the Hα and He I λ4715 line profiles in the spectrum of λ Ori A. © *2003 MAIK "Nauka/Interperiodica".*

Key words: *stars, variable and peculiar; hot stars; line-profile variability.*

INTRODUCTION

One of the most important problems in the physics of stars is the formation of a complex internal structure in the expanding atmospheres of early-type (WR, O, and B) stars, i.e., the stellar-wind formation mechanism. Ultraviolet (Kaper *et al.* 1997, 1999), visible (Kaufer *et al.* 1996; Kaper *et al.* 1997; Lépine and Moffat 1999; de Jong *et al.* 1999, 2001), and X-ray (Kahn *et al.* 2001) observations of these stars suggest that there are inhomogeneities of various sizes and densities in their atmospheres.

The line profiles for WR stars exhibit variable features (subpeaks) that shift from the line center toward the line wings. These are associated with compact structures (commonly called clouds) in the atmosphere. The individual subpeaks contain no more than 1–2% of the total energy emitted in the line and, according to Lépine *et al.* (1996) and Lépine and Moffat (1999), the subpeaks themselves are short-lived profile features. The subpeaks with the highest flux have widths up to 200–300 km s^{-1} and are traceable in the profiles up to one or two days, whereas the smallest detected subpeaks with widths of about 50 km s^{-1} are seen in the profiles for no more than one or two hours. Small cloudlets that form narrow subpeaks with widths of 10–40 km s^{-1} (Kholtygin 1995), which are undetectable in the line profiles with currently available stellar spectroscopy, are assumed to be also present in the atmospheres.

This pattern of profile variability can be interpreted in terms of the stochastic cloud atmospheric model suggested by Kholtygin *et al.* (2000) and Kudryashova and Kholtygin (2001). In this model, which is a generalization of the cloud atmospheric model for Wolf–Rayet stars (Antokhin *et al.* 1988, 1992), the expanding stellar atmosphere (envelope) is a set of dense, small-scale inhomogeneities (clouds) in a rarefied intercloud medium. The formation and destruction of clouds in the atmosphere is treated as a stochastic process. Using the cloud model allows us to calculate both the ionization and thermal atmospheric structures and the variable profiles of the lines that originate in the atmosphere (Antokhin *et al.* 1992; Kudryashova and Kholtygin 2001). The concept of the stochastic cloud model was used to develop a three-phase cloud atmospheric model for early-type stars (Kholtygin 2001; Kholtygin *et al.* 2002). In this model, it is assumed that an ensemble of hot ($T = 10^6$–10^7 K) clouds that produce stellar X-ray radiation and of cold clouds in which ions of relatively low ionization stages (He II, C II, N II, and others) are preserved can be separated from the complete set of clouds.

The pattern of line-profile variability in the spectra of O and B stars is much more complex. Its clearest manifestation is the appearance of variable absorption features called discrete absorption components

*E-mail: afk@theor1.astro.spbu.ru

Table 1. A list of the program stars

HD	Name	Spectral type	V	V_∞	$V\sin i$, km s^{-1}	V_r, km s^{-1}
24212	ξ Per	O7.5III	4.04	2330	213	64.6
30614	α Cam	O9.5I	4.29	1590	129	6.1
36486	δ Ori	O9.5II	2.23	2060	144	118.3
36861	λ Ori A	O8III	3.66	2175	74	35.4
37742	ζ Ori A	O8III	1.79	1860	124	12.8
47839	15 Mon	O7Ve	4.66	2110	67	19.6
91316	ρ Leo	B1Iab	3.84	1110	75	42.0
203064	68 Cyg	O8e	5.04	2340	115	−3.9
209975	19 Cep	O9.5I	5.11	2010	95	−12.8
210839	λ Cep	O6Iab	5.09	2300	219	−75.9
214680	10 Lac	O9V	4.87	1140	35	−4.7

(DACs) in the profiles of the resonance and subordinate ultraviolet lines of N IV, Si IV, and other species. These features are detected in the violet parts of the profiles at frequencies that correspond to Doppler shifts from −300 to −800 km s^{-1} and then shift toward higher negative velocities until they reach the profile edge that corresponds to terminal wind velocities (1500–2500) km s^{-1}. The DAC formation is a cyclical process. The DAC evolution cycles are repeated at intervals of one or two days, while the overall pattern of DAC formation is stable over several years; the cycle length is virtually constant over the entire period of observations (de Jong *et al.* 1999), which argues for the hypothesis that the DAC formation is a periodic process.

The appearance of DACs is generally associated with the formation of large-scale structures in the stellar atmospheres in the regions where the star and the stellar wind corotate (Kaper *et al.* 1997; de Jong *et al.* 2001). The profile variability of the H I and He I lines in the visible spectrum of O stars is also associated with these structures. The fact that the periods of the optical-line profile variations are close to the DAC formation periods (Kaper *et al.* 1997) lends support to this hypothesis.

Although the line-profile variations in the spectra of early-type stars have long been studied, it is not yet completely clear why large-scale structures are formed. The presence of regions with different velocities and different mass outflow rates in the photospheres is suggested as one of the causes of their formation. The formation of such regions is associated with nonradial pulsations of O and B stars; the short-period (3–12 h) He I line profile variations detected in many B stars and six O stars (de Jong *et al.* 2001) serve as an indicator of these pulsations. One of the factors that favor the formation of large-scale atmospheric structures may be a weak (several hundred G) magnetic field on the stellar surface (Donati *et al.* 2001). However, as yet no evidence of a magnetic field has been found in O stars (Kaper *et al.* 1997).

Calculations of the dynamics of the expanding atmospheres in early-type stars (Owocki 1998) predict the radiative instability of the atmospheres of WR, O, and early-B stars and the formation of a broad spectrum of inhomogeneities in their atmospheres, both large-scale and small-scale ones. Because of the formation of small-scale inhomogeneities in the atmospheres, the optical line profiles in the spectra of all early-type stars must exhibit not only regular but also irregular (stochastic) profile variability characteristic of WR stars. This type of variability was found in the brightest O star ζ Pup. The subpeaks associated with small-scale inhomogeneities that shift toward the line wings were detected in the He II λ4686 Å line profiles in the spectrum of this star (Eversberg *et al.* 1998). No evidence of stochastic line-profile variability has yet been found in other O stars.

Note that the formation of large-scale structures in corotation regions is a stochastic process, as the shock front in the boundary region between fast and slow gaseous streams is unstable. This instability can lead to a breakup of the gaseous streams corotating with the star in its atmosphere into separate fragments. As a result, the line-profile variability in the stellar spectra will also be irregular.

For this reason, a detailed study of the regular and irregular (stochastic) line profile variability in the spectra of bright O stars attributable to the presence of small-scale inhomogeneities (clouds) in their atmospheres seems of current interest. This paper is the first in a series of papers that describe the results of such a study. We outline our program of searching for stochastic line-profile variability in the spectra of O stars and present the first results of our analysis of the line profiles for the stars α Cam, 19 Cep, and λ Ori obtained in 2001 with the 1-m Special Astrophysical Observatory (SAO) telescope.

THE PROGRAM OF SEARCHING FOR VARIABILITY

The studies of profile variability in early-type stars (Kaper *et al.* 1999; Eversberg *et al.* 1998; Kholtygin *et al.* 2000) indicate that high-quality spectroscopy is required to reliably detect both regular and stochastic profile variations: a spectral resolution of $R \geq 40\,000$; a signal-to-noise (S/N) ratio near the lines under

study of 200–300 or more; and a sufficiently high time resolution, 10–30 min.

Therefore, we selected bright ($V \leq 5^m.5$) northern-sky O stars whose spectra could be obtained with the parameters required to search for variability at the coudé focus using the CEGS coudè–echelle spectrograph of the 1-m SAO telescope (Musaev 1996). The program stars are listed in Table 1. Additionally, the list was supplemented with the bright B1 star ρ Leo to study the change in the pattern of profile variability when passing from late-O to early-B stars; during this passage, the mass-loss rate decreases sharply. The last columns of the table give terminal wind velocities V_∞ (Howarth *et al.* 1997), projected rotational velocities $V \sin i$ (Kaper *et al.* 1997), and radial velocities (Conti *et al.* 1977; Wilson 1953).

When choosing appropriate dates of observations, the program stars can be observed for almost the entire night. As a result, long series of observations (spanning two or three stellar rotation periods) needed for an accurate separation of the regular line-profile variability component can be obtained when they are observed for three to six nights. We suggest the following strategy for observations: obtaining long series of observations with the 1-m SAO telescope in order to reveal the overall pattern of variability in the program stars, and studying in detail those stars in which profile variability or any unusual spectral features were detected using the 6-m SAO telescope.

OBSERVATIONS OF THE PROGRAM STARS IN 2001

The first observations under the program described above were carried out during September 4–7 and November 29–December 4, 2001, with the 1-m SAO telescope. General data on these observations are given in Table 2.

The total number of spectra obtained in 2001 exceeds 200. Here, we consider the results of our observations for three stars: α Cam, 19 Cep, and λ Ori A. The results of our observations for the remaining program stars will be presented in the following publications. To achieve the signal-to-noise ratio S/N > 200 required to search for variability in the fainter star 19 Cep, we added the two spectra taken at adjacent times with 15-min-long exposures.

Organizing the Observations and Reducing the Spectroscopic Data

The program stars were observed with the CEGS coudé–echelle spectrograph of the 1-m SAO telescope. The configuration of this instrument was described by Musaev (1996). The detector was a Wright Instruments 1242 × 1152-pixel CCD array. With a spectrograph entrance slit width of 2″, the spectral resolution $R = 45\,000$ (0.08 Å pixel^{-1} near Hα) is achieved in the wavelength range from 4000 to 8000 Å.

Table 2. A list of the stars observed in 2001

Object	Exposure, min	Number of spectra	Total observing time, h
September 4–7, 2001			
ξ Per	10	4	0.7
α Cam	10	11	1.8
19 Cep	15	22	6.0
10 Lac	10–15	39	10.5
November 29–December 4, 2001			
ξ Per	5	5	0.4
α Cam	10	6	1.0
λ Ori A	10	75	12.5
ζ Ori A	2	36	1.2
10 Lac	15	27	6.7

The spectra were reduced by using the MIDAS package. The CCD image processing procedure included the following: scattered-light removal, echelle-order position determination, cosmic-ray particle hit removal, echelle-order extraction, continuum placement, correction for pixel-to-pixel CCD sensitivity nonuniformity, and spectrum linearization on the wavelength scale.

Since the operations described above were performed using standard procedures of the MIDAS package, we give comments only to those procedures that differ from the commonly used ones. The echelle spectra of the program stars were directly used to determine the order positions. We used the same order position mask for all the spectra of a given star taken on a given night.

To analyze the line-profile variability, we normalized the spectra to continuum. The continuum was placed separately in each echelle order by using a broad Gaussian-like filter (Shergin *et al.* 1996). For the entire sequence of spectra for a given star, we used the same parameters of the filter with a filter window width of 25–30 Å. In the three orders in the spectrum of λ Ori A with the Hα, C III λ5696 Å, and He II λ4686 Å lines, the continuum was placed by a different method: the spectrum was smoothed by a moving average, with the line regions being excluded from the procedure. We also studied the latter method

and tested it using spectroscopy for stars of various spectral types. It yields stable results in placing the continuum even if there are broad and variable lines in the spectrum or if the weather conditions change during the observations.

To make a correction for pixel-to-pixel CCD sensitivity nonuniformity, we observed the bright, rapidly rotating star α Leo ($V \sin i = 329$ km s^{-1}). As a result of this procedure, the S/N ratio in the individual spectrum increased by 20–50%, depending on the signal level and the residual pixel-to-pixel nonuniformities do not exceed 0.3% in amplitude.

The dispersion relation was derived from the spectrum of scattered solar light and its accuracy was 10 mÅ. Our reduction procedure ensures the same reduction of the entire sequence of spectra for a given star, which makes it possible to properly analyze the line-profile variability. For the wavelength calibration, we applied corrections for the Earth's rotation and its revolution around the Sun for each star.

Profile Variability

We elucidated the question of profile variability by using a standard technique. All spectra of the program star were added to obtain an average spectrum. The average Hβ and Hα profiles in the spectra of the program stars determined in this way are shown in Fig. 1. The radial velocities in Table 1 were used to transform the wavelength scale to the frame of reference associated with the star.

We determined the difference profiles (the individual profile minus the average profile) to identify variable features in the line profiles of all our spectra. Variable features were detected in the difference line profiles in the spectra of all our program stars. Figure 2 illustrates the difference Hα и He I λ5876 Å line profiles in the spectrum of 19 Cep, in units of the continuum intensity. The time axis is directed from the bottom upward. For clarity, the sequential profiles were displaced along the intensity scale. A variable feature with a maximum amplitude of 4–5% is clearly seen from the figure in the red part of the profile ($\approx$90 km s^{-1}). This feature shifted only slightly over the entire period of our observations of the star (6 h). Such variable features with the same velocity shift in the spectrum of this star were also detected in the Hβ profile.

Since the profile variation amplitude in the spectra of other program stars is appreciably smaller than that for 19 Cep, we used the following approach to ascertain whether the profile of a particular line was variable. For all wavelengths λ within the line profile, we calculated the quantity $\sigma_{\rm line}(\lambda)$—the standard deviation of the random variable $\Delta(\lambda, t)$, the difference between the individual and average line profiles for a given wavelength λ at time t. Simultaneously, we determined $\sigma_{\rm cont}$—a similar quantity for the continuum region near the line under consideration.

The measured flux in the difference spectrum at wavelength λ_j at time t_i can be represented as $F_j = F_j(t_i) = S_j + N_j$, where $S_j = S_j(t_i)$ is the sought-for signal and $N_j = N_j(t_i)$ is the noise component. Within one order, $N_j(t)$ can be assumed to be a normally distributed random variable with a zero mean and a variance $\sigma^2_{\rm cont}$. Let us analyze m difference spectra for the consecutive times $t_1, t_2, \ldots, t_m$. Assuming that the profiles are not variable ($N_j \gg S_j$), the random variable $S_{m-1} = \sigma_{\rm line}(\lambda)$ has the distribution $\sigma_{\rm cont}\sqrt{\chi^2/(m-1)}$, where χ^2 is the χ^2 distribution with $m-1$ degrees of freedom (see, e.g., Brandt 1975).

We specify a significance level α. Let the random variable

$$\sigma_{\rm line}(\lambda) > S^{\alpha}_{m-1}, \qquad (1)$$

where S^{α}_{m-1}, calculated for a given λ, is defined in such a way that the probability that this random variable exceeds $\sigma_{\rm line}(\lambda) > S^{\alpha}_{m-1}$ is equal to α. The hypothesis of a constant flux in the line at the significance level α is then rejected and the hypothesis of a variable component in the line is accepted.

The above procedure of searching for line-profile variability is similar to that used by Fullerton *et al.* (1996). These authors also used a procedure for smoothing the standard-deviation spectrum $\sigma_{\rm line}(\lambda)$ by taking into account the variation of the CCD sensitivity along the line profile. Since our technique for eliminating CCD sensitivity variations (pixel-to-pixel nonuniformity) proved to be efficient enough, no additional smoothing of the spectrum $\sigma_{\rm line}(\lambda)$ is required.

To illustrate our technique for searching variability, Fig. 3 shows the standard-deviation spectra $\sigma(\lambda)$ for the regions near the Hα, He II λ4686 Å, and C III λ5696 Å lines in the spectra of 19 Cep, α Cam, and λ Ori. We see from the figures that the lines in the spectra of all stars, except α Cam, satisfy the variability criterion (1). The position of the peak in the standard-deviation spectrum corresponds to the maximum line-profile variability amplitude. To increase the reliability of determining variable profiles in the spectra of the program stars, we used additional variability criteria based on the analysis of line-profile variations in the spectrum of a specific star:

(a) The lack of dependence of the profile variability pattern on the line position within a spectral order and the similarity of the profile variations for the same line

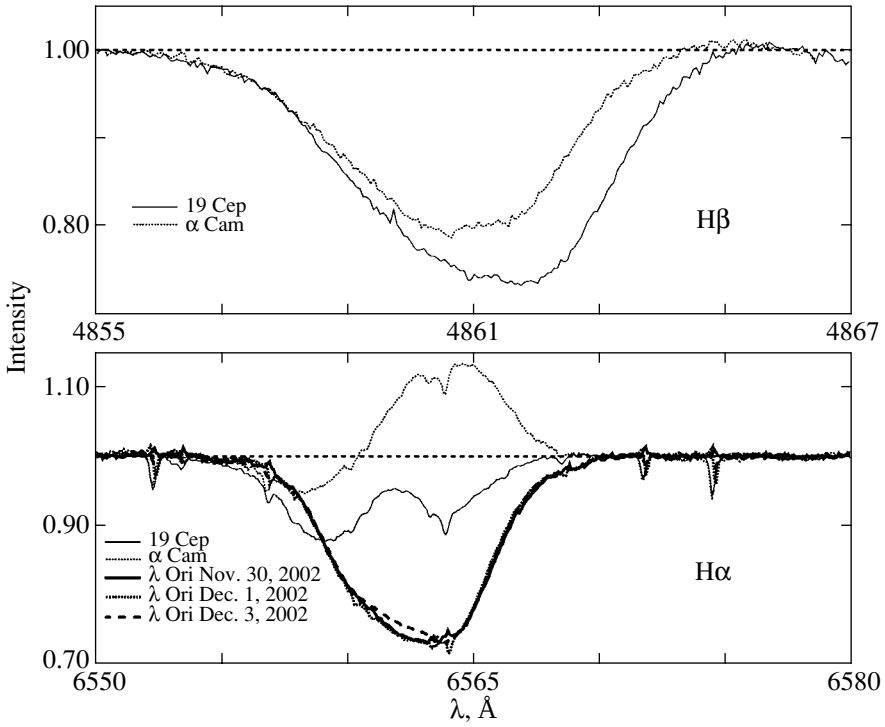

Fig. 1. Comparison of the Hα and Hβ profiles in the spectra of 19 Cep, α Cam, and λ Ori. The intensities (Y axis) are given in fractions of the continuum intensity.

in two adjacent orders (e.g., the Hβ and He I λ5876 Å lines);

(b) The same profile variability pattern for different lines of the same element and for lines of different elements (e.g., H, He, and C);

(c) Similar variability amplitudes for different lines; and

(d) Similar radial velocities of variable profile features for different lines.

Note, for example, that the variable features in the Hα and Hβ profiles in the spectrum of 19 Cep are shifted by 86 and 88 km s^{-1}, respectively.

An additional argument for the assumption that the profile variability we detected is real is that the variability was detected in the line profiles of the spectra of the stars under study, whereas in the profiles of intense unidentified interstellar bands (e.g., λ5778 and 5780 Å), no such variability was detected at a level down to 0.003 in flux units in the neighboring continuum. An additional argument for the reality of the profile variability is that the variability was detected in the profiles of strong H I, He I, He II, and C III lines, whereas no such variability was found in the profiles of intense unidentified interstellar bands (e.g. λ5778 and 5780 Å).

Table 3 gives a list of the lines for all of the program stars that satisfy criterion (1) with an allowance made for the above additional criteria (a)–(d). The profiles were found to be variable for all our program stars. At the same time, a variability of the Hα and C III λ5696 Å line profiles in the spectrum of λ Ori A has been detected for the first time (see Kaper *et al.* 1999). The similarity between the lists of variable lines for the program stars stems from the fact that the most intense lines in their spectra were included in the table. A significant increase in the signal-to-noise ratio is required to detect profile variability for weak lines.

The absence of lines that satisfy criterion (1) in the spectra of α Cam taken in September 2001 is attributable to the short period of our observations (less than 2 h) and to the small (11) number of spectra (see Table 2). At the same time, our observations of line profiles in the spectrum of this star in 1997 revealed variability of the He II λ4686 Å and Hα line profiles on time scales 2–4 h (Kholtygin *et al.* 2000).

The following technique is used to ascertain whether the line profiles are variable in the absence of their visible variations. Before obtaining the standard-deviation spectrum, the difference spectra are presmoothed by using a filter that is broad compared to the pixel size. In this case, if the filter width is $\Delta\lambda$ on the wavelength scale, then the amplitude of the random (noise) component of the difference profiles $\overline{N_j(t)}$ after applying the smoothing procedure

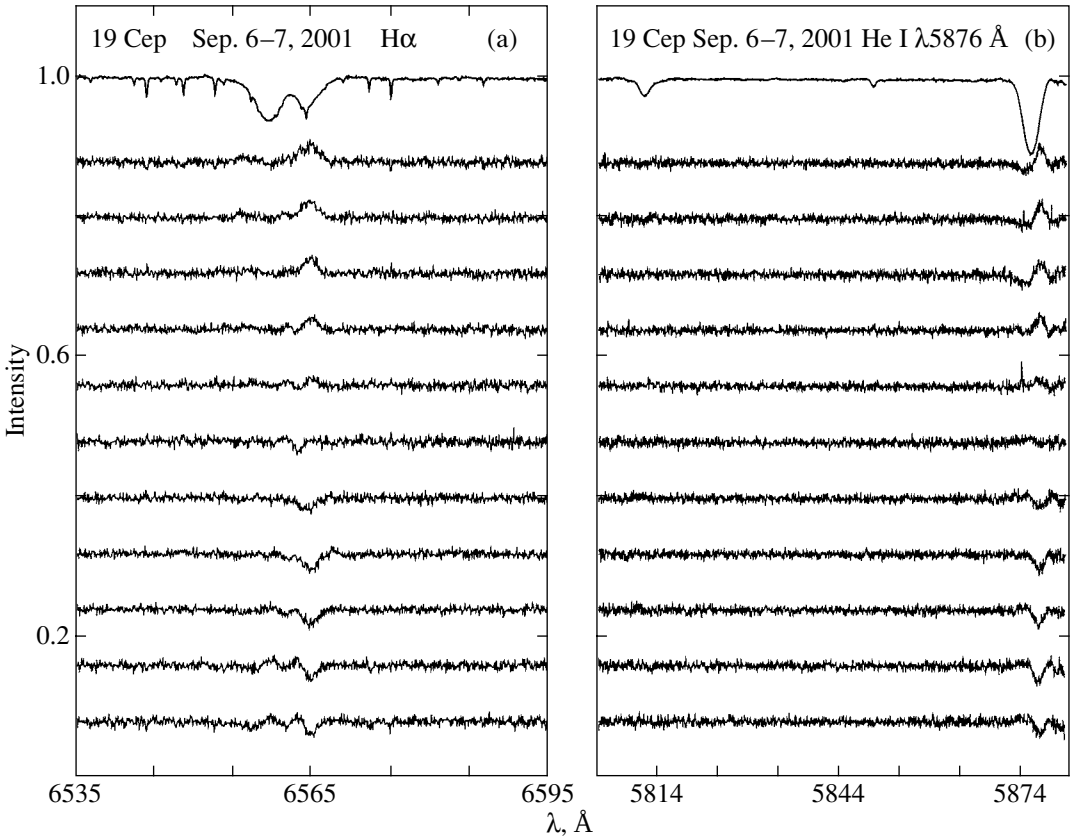

Fig. 2. Difference (a) Hα and (b) He I λ5876 Å line profiles in the spectrum of 19 Cep. The intensities are given in fractions of the continuum intensity. The individual profiles were displaced along the Y axis by 0.08 in the same units. The time axis is directed from the bottom upward. The upper curves are the mean profiles of the corresponding lines compressed by a factor of 2.5.

decreases by a factor of $\approx\sqrt{\Delta\lambda/\delta\lambda}$, where $\delta\lambda$ is the pixel width on the wavelength scale near the line under consideration. If the width of a variable component is not less than the filter width, then after applying the smoothing procedure, the peaks in the standard-deviation spectrum that correspond to the variable component are clearly distinguished. Figures 3b, 3d, 3f, and 3h illustrate the use of the profile smoothing procedure to analyze the profile variability.

It was empirically established that the most satisfactory results are obtained when smoothing the profiles with a Gaussian filter 0.5–1.0 Å (7–15 pixels) in width. An examination of Fig. 3 indicates that even if no significant profile variations are detected in the unsmoothed standard-deviation spectrum (Fig. 3c), presmoothing allows such variations to be distinguished quite clearly (see Fig. 3d). For several lines in the spectra of the program stars, criterion (1) is satisfied only for the smoothed difference spectra. A list of these lines is given in the last column of Table 3.

The question of how errors in the continuum placement affect the detection of profile variability should be considered separately. Analysis of these errors indicates that they increase with line width. However, even for the broadest lines, the absolute errors in continuum placement do not exceed 1%. In narrower lines, such as C III λ5696 Å or He II λ4686 Å, they are much smaller. In addition, the same procedure of continuum placement is used for all spectra. Thus, even the possible small errors in continuum placement affect all spectra in the same way.

The procedure of searching for profile variability described above only answers the question of whether the profile of a specific line is variable or not. At the same time, to elucidate the profile variability mechanism requires, as was noted in the Introduction, answering the question of whether the profile variations are to one or another degree regular (cyclical), irregular (stochastic), or a superposition of regular and irregular variations. To answer this question, it would be appropriate to use the techniques of Fourier (see, e.g., Roberts *et al.* 1987; Vityazev 2001) and wavelet (Dobeshi 2001; Kudryashova and Kholtygin 2001)

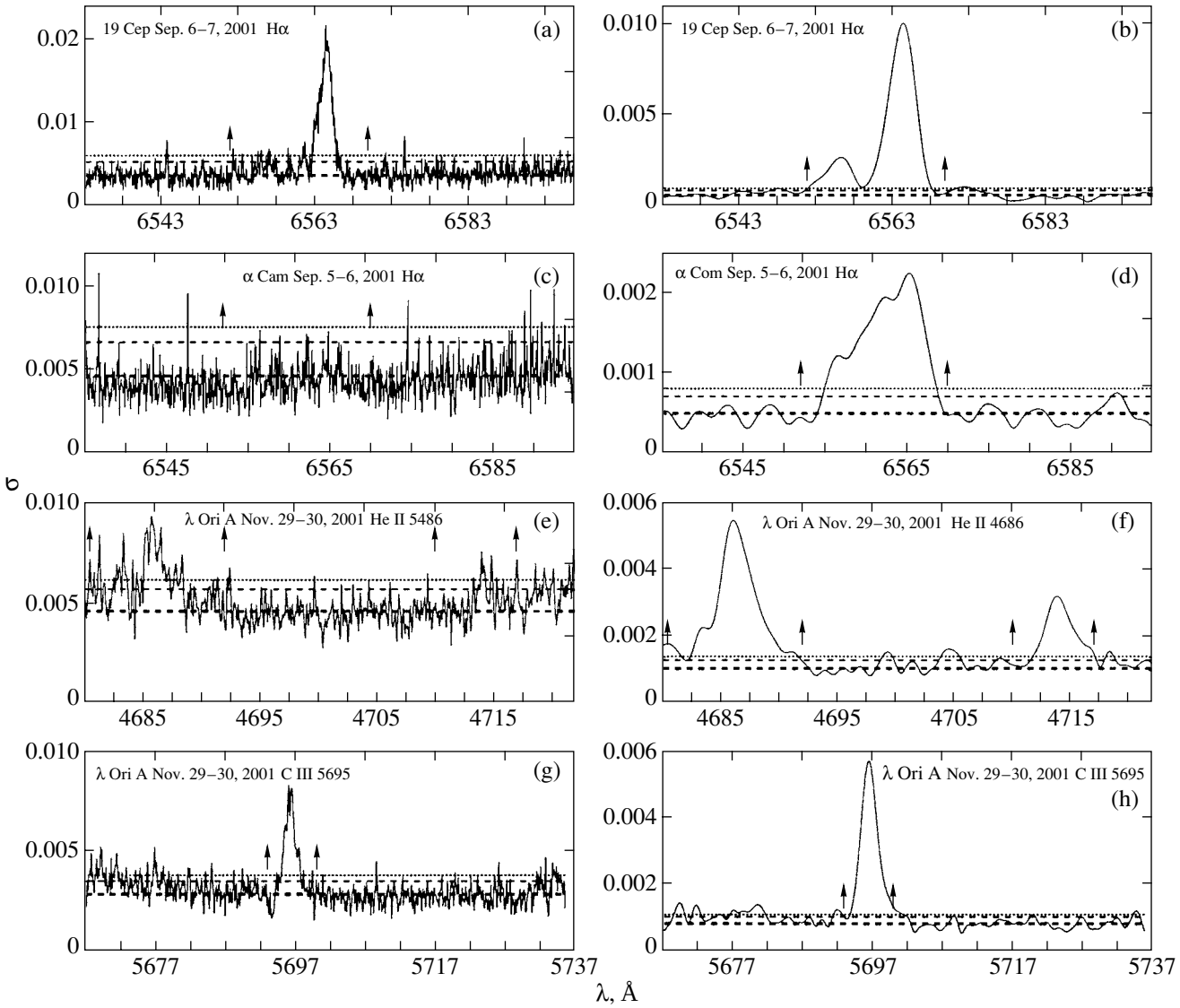

Fig. 3. Standard deviations of the difference Hα profiles in the spectra of 19 Cep, α Cam, and λ Ori A, in fractions of the continuum intensity. The horizontal lines in all figures correspond to the significance levels of the hypothesis that the profiles are not variable equal to 0.01, 0.05, and 0.50 (from the top downward). The arrows indicate the short- and long-wavelength boundaries of the line profiles. The unsmoothed and smoothed (with a 1.0-Å-wide Gaussian filter) difference line profiles were used in the left and right panels, respectively, to calculate the standard deviations.

analyses. The results of these analyses are described in the next sections.

VARIABILITY ANALYSIS

Wavelet Analysis

Analysis of the average line profiles in the spectra of the program stars (Fig. 1) and of the corresponding difference profiles (Fig. 2) indicates that the total line profile can be represented as a combination of the average profile and a large number of discrete features. The most suitable mathematical technique for studying the variability of such profiles is a wavelet analysis (see, e.g., Lépine *et al.* 1996). In this case, it would be appropriate to use the so-called MHAT wavelet $\psi(x) = (1 - x^2)\exp(-x^2/2)$ with a narrow power spectrum and zero zero and first moments as the analyzing (mother) wavelet. Note that the MHAT wavelet is the second derivative of the Gaussian function, which can be used to describe the shape of the features in the difference line profiles.

Using this wavelet, we can write the integral wavelet transform as (Lépine *et al.* 1996; Dobeshi

Table 3. Lines with variable profiles in the spectra of α Cam, 19 Cep, and λ Ori A

Star	Date of observation	Variable lines	Possible variability
19 Cep	Sep. 2001	Hβ, Hα, He I λ5876 Å	–
α Cam	Sep. 2001	–	He I λ4713 Å, Hβ, Hα
λ Ori A	Nov.–Dec. 2001	Hα, He II λ4686 Å, C III λ5696	He I λ4713 Å

2001):

$$W(s,u) = \frac{1}{s}\int\limits_{-\infty}^{\infty} f(x)\psi\left(\frac{x-u}{s}\right)dx \qquad (2)$$
$$= \int\limits_{-\infty}^{\infty} f(x)\psi_{su}(x)dx.$$

The signal power density $E_W(s,u) = W^2(s,u)$ characterizes the power distribution of the signal under study in space (s,u) = (scale, coordinate). Since in our case, the coordinate x is the wavelength, the scaling variable s can be expressed in Å.

The total power is distributed in scale in accordance with the global wavelet-transform power spectrum:

$$E_W(s) = \int\limits_{u_1}^{u_2} W^2(s,u)du = \int\limits_{u_1}^{u_2} E_W(s,u)du. \qquad (3)$$

The scale a where the function $E_W(s)$ reaches a maximum is called the dominant scale of the signal $f(x)$ under study on the interval u_1 and u_2 (Lépine *et al.* 1996).

We obtained wavelet power spectra for all the line profiles in the spectra of the programs stars in which variability was detected or suspected. The violet and red profile edges were used as u_1 and u_2, respectively. Thus, we considered the wavelet-transform power spectrum in the wavelength range that corresponded to the full profile width. Some of our spectra are shown in Fig. 4. Analysis of the power spectra reveals two components in the signal under study: small-scale (0.1–0.4 Å) and large-scale (0.5–8 Å) ones.

The first component in 19 Cep (Figs. 4a, 4b) and α Cam (Fig. 4c) changes only slightly over the period of our observations and has a maximum on a scale close to 0.1 Å, the CCD pixel size. The absence of noticeable variability of the small-scale component in the wavelet power spectrum for these stars provides evidence for the assumption that it is determined mainly by the noise contribution and by the residual effects of pixel-to-pixel CCD nonuniformity.

At the same time, the small-scale component in the wavelet power spectrum of the difference line profiles for λ Ori (Figs. 4d–4f) exhibits noticeable irregular variability with a maximum amplitude on the scale of 0.2–0.3 Å (10–15 km s^{-1}). The presence of a variable component in the wavelet power spectrum on these scales can be attributed to the existence of small-scale (10^{-3}–$10^{-2}R_\odot$) inhomogeneities in the atmosphere of λ Ori (Kudryashova and Kholtygin 2001).

The large-scale component in the wavelet power spectrum is highly variable for all our program stars. The maximum variability amplitude corresponds to the dominant scales of 1.5–6 Å, the characteristic size of variable features in the line profile (see Fig. 2). The time dependence of the power spectrum is the subject of the next section.

Periodic and Stochastic Line-Profile Variations

As was noted above, the studies of line profiles in the spectra of most O stars reveal their periodic variations. It would be natural to hypothesize that such variations also show up in the wavelet power spectrum of the difference line profiles. To test this hypothesis, we analyzed the time dependence of the integrated wavelet power spectra:

$$E[S_1,S_2](t) = \int\limits_{s_1}^{s_2} E_W(s,t)ds. \qquad (4)$$

Here, t is the time at which the profile under study was obtained, which is assumed to be equal to the midexposure time of the corresponding spectrum. The range 1.5–2.5 Å, in which the amplitude of the wavelet-spectrum variations is at a maximum, was chosen as the scale interval S_1, S_2. The derived functions $E[S_1,S_2](t)$ are plotted against the time of observation t in Figs. 4g–4l. For convenience, the time of observation is given in fractions of a day and the midexposure time of the first spectrum in the series of observations under study was taken to be zero.

As we see from Fig. 4, the dependences $E[S_1,S_2](t)$ are fairly regular. In searching for a harmonic component, we fitted the function $E[S_1,S_2](t)$ by a sine wave with the amplitude, period, phase, and shift determined by the least-squares method. The

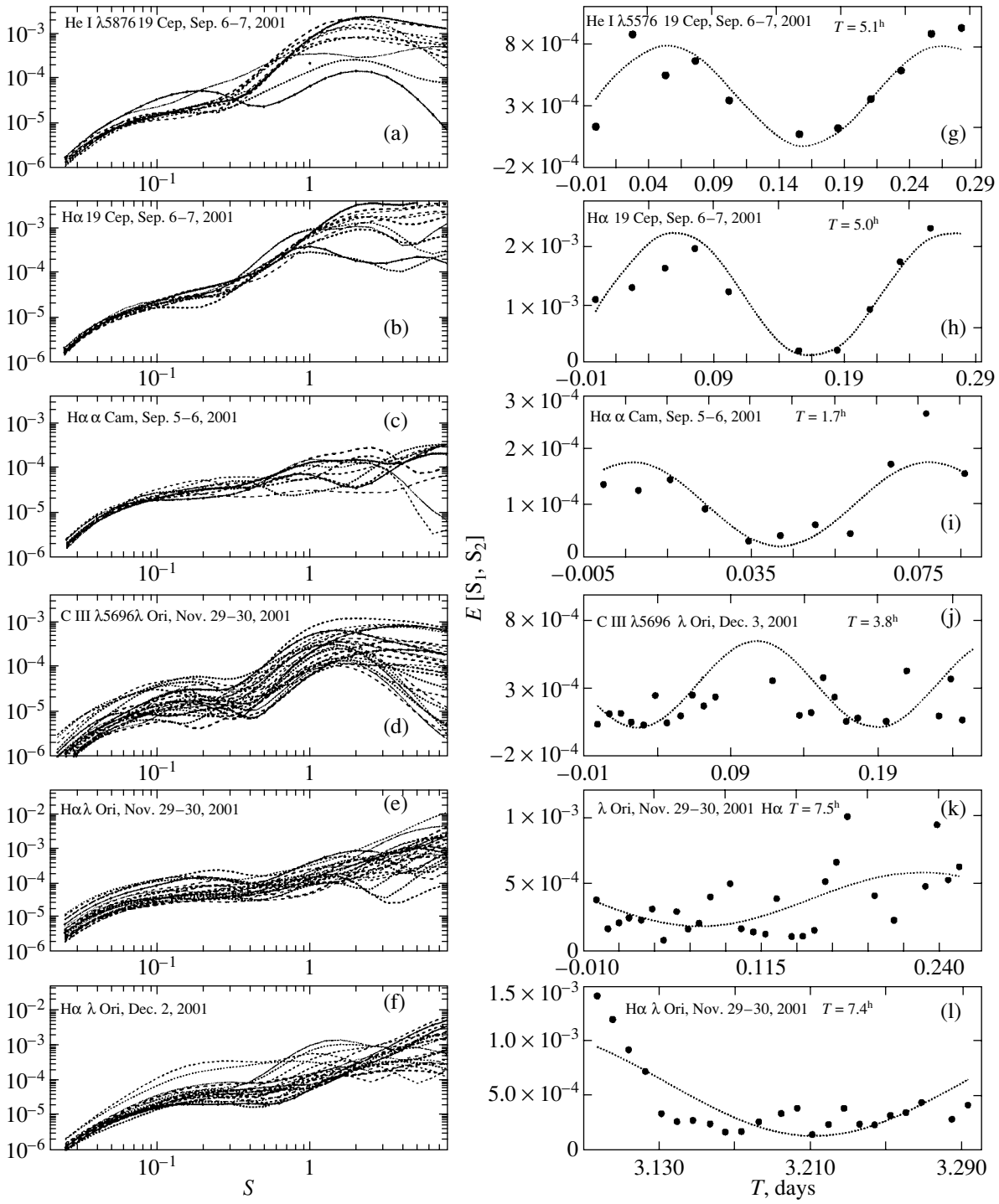

Fig. 4. (a–f) Wavelet power spectra of the difference profiles for the He I λ5876 Å, C III λ5696 Å, and Hα lines in the spectra of 19 Cep, α Cam, and λ Ori as a function of the wavelet-transform scale S in Å. (g–l) The total power-spectrum amplitudes in the scale range 1.5–2.5 Å (dots) versus the time of observation. The solid lines represent the sinusoidal fits.

derived fits are indicated in Figs. 4g–4l by the solid lines. Also shown in these figures are the inferred periods T of the wavelet power spectrum variations. The determined periods lie within the range $1.7–9.2^{\rm h}$ and correspond to the characteristic frequencies of the nonradial photospheric pulsations in stars of the corresponding spectral types (de Jong *et al.* 2001).

When the spectrum of λ Ori A was obtained, its companion λ Ori B ($5^{m}.61$) was within the spectrograph slit for about an hour out of the six hours

of observations (21–22 UT). For this reason, the question of how the companion contribution affects the line-profile variability is of considerable importance. The apparent magnitude of the companion is significantly fainter than that of the primary star (by $2^m.5$). In addition, no features were seen in the time dependence of the wavelet-transform amplitude (Figs. 4j–4l) when the companion was within the spectrograph slit. A detailed analysis revealed that the spectral scans across the dispersion were symmetric, suggesting that the line profiles are negligibly affected by the companion.

To elucidate the question of whether the periods found are real, we carried out a numerical experiment to determine the variation period of the function $E[S_1, S_2](t)$ from a model spectrum: a sinusoidal component plus a normally distributed noise component (N). As the times and the number of observed spectra (N_{sp}), we used the corresponding values for 19 Cep, α Cam, and λ Ori. The results of our experiment indicate that at the ratio A/N = 3–6, where A is the amplitude of the variable component and N is the noise level in the spectral range under consideration, with the number of spectra $k = 11$–30 and periods 1–10^h; the derived periods at a 0.95 confidence level lie in the interval $\pm 50\%$ of the original period of the harmonic component.

The effective value of A/N for the wavelet power spectra is determined by the S/N ratio for the original (nonnormalized) profiles of the program stars. It is A/N ≈ 6 for 19 Cep and α Cam and A/N ≈ 3 for λ Ori. Nevertheless, we believe that the conclusion regarding the detection of cyclical variations in the integrated wavelet power spectra would be premature. The time series shown in Figs. 4g–4l indicate that our derived periods are comparable to or even longer than the total period of observations of the program stars. Therefore, longer series of observations are required to confirm their reliability.

The period of the variations in the C III λ5696 Å emission line revealed by the analysis described above is approximately half the period of the variations in Hα, which may also suggest an insufficient reliability of the determined periods. It should be noted that the emission in these lines originate in different regions of the stellar atmosphere (Kaper *et al.* 1997). Therefore, the difference between the profile variation time scales may be quite real, although the question of whether the profile variations are periodic is still an open question.

Our analysis of the variations in the wavelet power spectrum is based on the assumption that one sinusoidal component mainly contributes to the variations in the function $E[S_1, S_2](t)$. More accurate methods should be used in the case of comparable contributions from harmonic components. For this reason, we performed a Fourier analysis of the line-profile variability in the spectrum of λ Ori A, for which the largest number (75) of profiles were obtained. All of the profiles observed over the three days of observations are difficult to use for our analysis, because there are long gaps (18 and 42 h) between the series of observations. These gaps result in a complex shape of the spectral window and require cleaning the Fourier spectrum from spurious peaks. To perform this procedure, we used the CLEAN algorithm (Roberts *et al.* 1987) in a modified version described by Vityazev (2001). To remove spurious components in the Fourier spectrum, we rejected all peaks at a confidence level lower than 0.99.

The square of the magnitude of the Fourier-transform amplitude (periodogram) for the time series $E[S_1, S_2](t)$ is shown for Hα in Fig. 5a. The periodogram exhibits only one peak at a frequency of 3.49 day^{-1}, which corresponds to a period of 6.9^h close to the period revealed by an elementary analysis (see Figs. 4k, 4l). Figure 5b illustrates the accuracy of fitting the time series by the harmonic component found.

It would be natural to assume that the frequencies of the periodic variations in the large-scale components of the line profiles must also be obtained when analyzing the variations in the profiles themselves. To test this assumption, we performed a Fourier analysis of the profile variations for the Hα, C III λ5696 Å, and He II λ4686 Å lines. The profile variations for each line were averaged over 25 km s^{-1} velocity intervals relative to the laboratory wavelengths of these lines.

To illustrate our results, Fig. 5c shows a Fourier spectrum of the temporal variations in the Hα profiles in the velocity range 25–50 km s^{-1}. In the figure, we see two close Fourier components with comparable amplitudes. Figure 5d shows the time dependence of the Hα profile deviations in this velocity range and their fit based on our Fourier analysis of the profiles. We see from the figure that the presence of two components with close frequencies in the Fourier spectrum can result in significant variations in the amplitude of the line-profile deviation from its average position in intervals of 1–3 days. Similar results are also obtained by analyzing the Hα profile in other velocity ranges. Note that the results of the Fourier analysis of the difference spectra and the wavelet power spectrum in Hα are similar.

At the same time, our Fourier analysis of the He I λ4714 Å, He II λ4686 Å, and C III λ5696 Å line profiles reveal a large set of frequencies in the Fourier spectra, those detected when analyzing Hα and other frequencies, as illustrated by Figs. 5e and 5g.

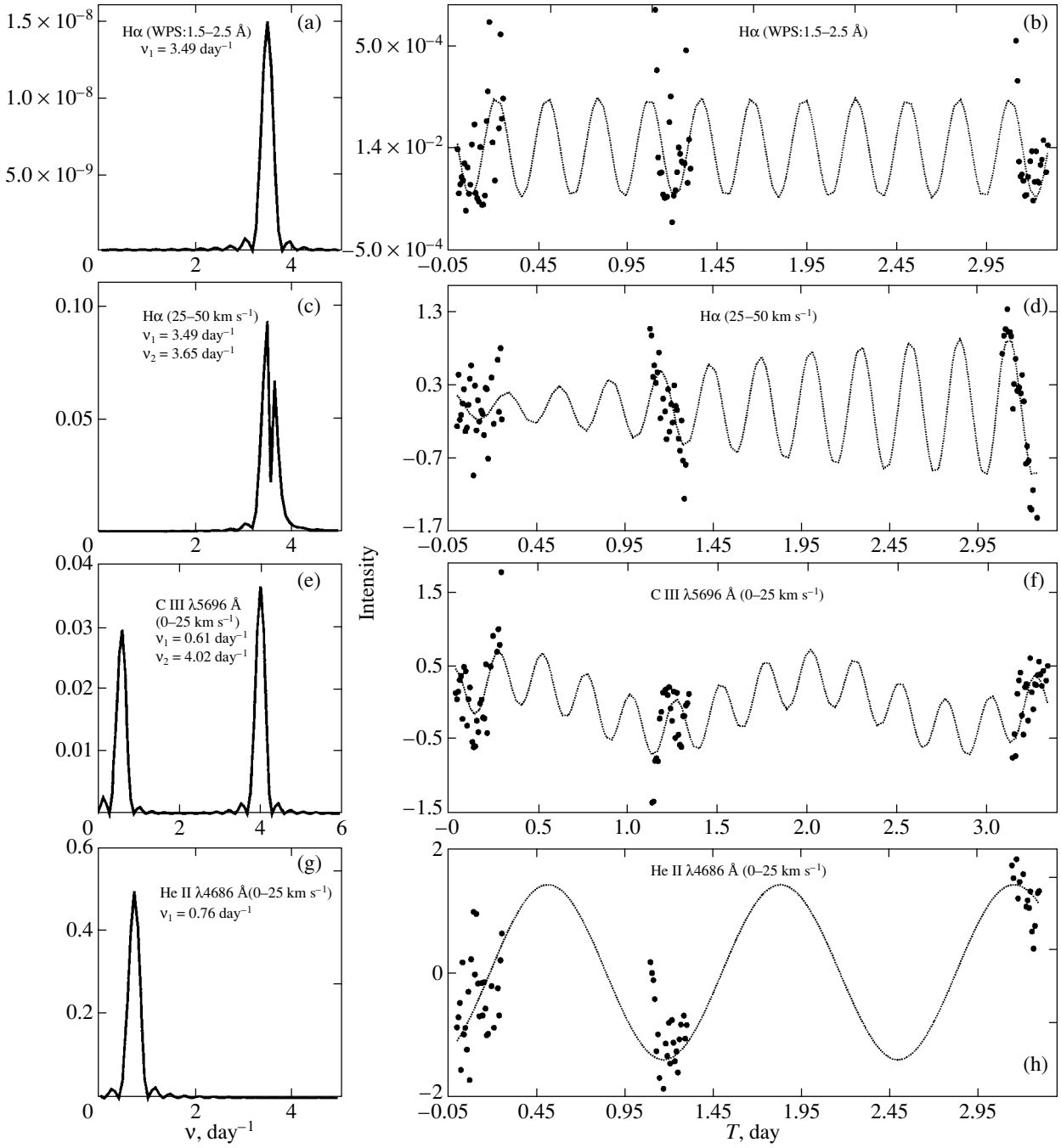

Fig. 5. (a) The periodogram of temporal variations in the wavelet power spectrum of the Hα line in the spectrum of λ Ori A in the range 1.5–2.5 Å determined from all of the spectra taken from November 30 through December 3, 2001; (b) a fit to the time dependence $E[S_1, S_2](t)$ for Hα; and (c) the same as (a) for the time dependence of the Hα profile deviations in the range 25–50 km s^{-1}. The continuum flux was assumed to be 100. (d) The same as (b) for the Hα profile variations; (e, f) the same as (c, d), for the C III λ5696 Å line ; and (g, h) the same as (c, d), for the He II λ4686 Å line.

Analysis of Line-Profile Variations

The Fourier analysis of the profile variations described in the preceding section shows the possible presence of both high-frequency and low-frequency components in the Fourier spectrum. The low-frequency components were detected in the profile variations for the He II λ4686 Å and C III λ5696 Å lines (see Figs. 5g, 5d); the frequencies of these components correspond to periods of $1^d.3$ and $1^d.6$, respectively. Kaper *et al.* (1997) detected profile

variation periods close to those found for λ Ori ($1-3^d$) in the Fourier spectra of the Hα profile variations in the spectra of the O stars O ξ Per, 68 Cyg, and λ Cep.

The regular profile variations for O stars with periods of several days are currently believed to be associated with the existence in their atmospheres of dense gaseous streams that corotate with the star at a distance of several tens of photospheric radii (Kaper *et al.* 1999; see, e.g., Fig. 21 in this paper). The profile variations are caused by the additional absorption of emission at line frequencies by the matter of the streams when they fall on the line of sight. Thus, the profile variation period is $P_n = P_{\rm rot}/n$, where $P_{\rm rot}$ is the stellar rotation period and n is the number of streams in the atmosphere.

The available data on profile variability in the spectrum of the star λ Ori itself are scarce. Its IUE ultraviolet observations (Kaper *et al.* 1999) reveal a DAC recurrence period in the Si IV $\lambda\lambda$1394, 1403 Å resonance line of $P_{\rm rec} = 5\overset{\rm d}{.}7$. Analysis of the variations in the difference profiles of the Si IV and N V $\lambda\lambda$1239, 11 243 Å resonance lines in the velocity range 1500–2000 km s^{-1} points to their regular variations with periods of $3\overset{\rm d}{.}4 \pm 0\overset{\rm d}{.}8$ and $4\overset{\rm d}{.}7 \pm 1\overset{\rm d}{.}4$, respectively. The above authors pointed out that the derived periods are unreliable because of the short period of observations and because of the detection of only one DAC event over the entire period of observation.

Thus, the presence of regular variations with periods $1\overset{\rm d}{.}3-1\overset{\rm d}{.}6$ in the spectrum of λ Ori can be said to be consistent with the available information on this star. Nevertheless, it would be premature to conclude that these periods were detected on the basis of our analysis of the profiles. According, for example, to Marchenko and Moffat (1998), when there are large gaps between the series of observations, even the choice of a high significance level does not give absolute confidence that the detected components in the Fourier spectrum are real. In light of these considerations, our detection of low-frequency components in the Fourier spectrum with periods $1\overset{\rm d}{.}3-1\overset{\rm d}{.}6$ needs to be additionally confirmed and the question of whether they are related to rotational profile modulation is still an open question.

Apart from the low-frequency components, the Fourier spectra of the profile variations for all the lines under study exhibit high-frequency components. The high-frequency components ($\nu = 2-8$ day^{-1}) are generally associated with nonradial photospheric pulsations (NRPs). The purely photospheric He I λ4713 Å line is considered to be the most convenient line for the detection of such components. Our analysis shows the possible presence of a component at frequency $\nu = 6.58$ day^{-1} ($P = 3.65^{\rm h}$) at the line center in the velocity range ($-25-100$ km s^{-1}) in the Fourier spectrum of the profile variations in this line in the spectrum of λ Ori. A $\nu = 4.39$ day^{-1} ($P = 5.47^{\rm h}$) component was detected in the violet part of the profile in the velocity range $-50 \ldots -25$ km s^{-1}. The same periods were found in the violet part of the He II λ4686 Å line profile.

In light of our remarks made above, we cannot assert that the presence of nonradial photospheric pulsations has been proven. To confirm this assertion and, if it is valid, to identify the periodic components found with specific (l, m) NRP modes requires a detailed analysis of the phase variations for these components along the line profiles (see, e.g., Schrijvers *et al.* 1997).

Apart from the components discussed above, we detected other components in the line-profile variations in the spectrum of λ Ori. In particular, the detection of short-period profile variations near the center of the C III emission line with the frequencies $\nu = 2.96$ day^{-1} ($P = 8.10^{\rm h}$) at $V =$ from -25 to 0 km s^{-1} and $\nu = 4.02$ day^{-1} ($P = 5.96^{\rm h}$) at $V = 0-25$ km s^{-1} (see Fig. 5e) proved to be unexpected.

A detailed analysis of these variations is to be performed in a separate publication. Note that the most reliable determination of the line profile periodicity pattern for the program stars requires obtaining their spectra with a high time resolution and with a much higher signal-to-noise ratio, which are to be taken with the 6-m SAO telescope in 2002. When using the 6-m telescope, a resolution of $R \approx 60\,000$ and a signal-to-noise ratio $S/N \approx 500-1000$ can be achieveed at short exposure times, up to 10–15 min.

CONCLUSIONS

We have presented our program of the search for and analysis of profile variability in the spectra of bright O supergiants with high time and spectral resolutions. Our observations and their analysis led us to the following conclusions.

(1) All of the program stars exhibit variable line profiles of hydrogen, He I and He II, C III, and other species. The variability amplitude is 4–5% for 19 Cep and 1–2% for α Cam and λ Ori on time scales of 6 h for 19 Cep and 1–3 days for λ Ori. The conclusion about profile variability is reliable at 0.99 confidence level.

(2) Variability of the Hα and C III λ5696 Å line profiles in the spectrum of λ Ori A was first detected at a 2% level of the continuum.

(3) The wavelet power spectra of the difference line profiles in the spectrum of λ Ori A were found to be variable on small scales: 0.2–0.3 Å (10–15 km s^{-1}), which may suggest the presence of small-scale perturbations in the stellar atmosphere.

(4) Our analysis of line profile variations is consistent with the hypothesis that regular profile variation components can exist. Low-frequency profile variations on time scales of 1.3–1.6 day consistent with the assumption of rotational profile modulation were detected in the variations of the He II λ4686 and C III λ5696 line profiles in the spectrum of λ Ori A.

(5) Short-period variations on time scales of 3.5–7 h close to the nonradial pulsation periods of O stars were detected in the violet parts of the Hα and He I λ4713 line profiles in the spectrum of λ Ori A.

ACKNOWLEDGMENTS

We are grateful to V.V. Vityazev for the remarks that improved the text of the paper and for providing the code that realizes the CLEAN algorithm. We are also grateful to A.B. Shneivais for help with the calculations. This study was supported by the Russian Foundation for Basic Research (project no. 01-02-16858) and the Federal Program "Research and Development in the Priority Fields of Science and Technology" (project "Studies of Energy Generation Mechanisms in Astrophysical Objects and the Behavior of Matter under Extreme Conditions ").

REFERENCES

1. I. I. Antokhin, A. F. Kholtygin, and A. M. Cherepashchuk, Astron. Zh. **65**, 558 (1988) [Sov. Astron. **32**, 285 (1988)].
2. I. I. Antokhin, T. Nugis, and A. M. Cherepashchuk, Astron. Zh. **69**, 516 (1992) [Sov. Astron. **36**, 260 (1992)].
3. Z. Brandt, *Statistical Methods of Monitoring Analysis* (Mir, Moscow, 1975), p. 87.
4. P. S. Conti, E. S. Leep, and J. J. Lorre, Astrophys. J. **214**, 759 (1977).
5. J. A. de Jong, H. F. Henrichs, S. Schrijvers, *et al.*, Astron. Astrophys. **345**, 172 (1999).
6. J. A. de Jong, H. F. Henrichs, L. Kaper, *et al.*, Astron. Astrophys. **368**, 601 (2001a).
7. J. A. de Jong, H. F. Henrichs, L. Kaper, *et al.*, Astron. Astrophys. **368**, 601 (2001b).
8. I. Dobeshi, *Ten Lections on Wavelets* (Moscow, 2001).
9. J.-F. Donati, G. A. Wade, J. Babel, *et al.*, Mon. Not. R. Astron. Soc. **326**, 1265 (2001).
10. T. Eversberg, S. Lépine, and A. F. J. Moffat, Astrophys. J. **494**, 799 (1998).
11. A. W. Fullerton, D. R. Gies, and C. T. Bolton, Astrophys. J., Suppl. Ser. **103**, 475 (1996).
12. I. D. Howarth, K. W. Siebert, G. A. J. Hussain, and R. K. Prinja, Mon. Not. R. Astron. Soc. **284**, 265 (1997).
13. S. M. Kahn, M. A. Leutenegger, J. Cottam, *et al.*, Astron. Astrophys. **365**, L312 (2001).
14. L. Kaper, H. F. Henrichs, A. W. Fullerton, *et al.*, Astron. Astrophys. **327**, 281 (1997).
15. L. Kaper, H. F. Henrichs, J. S. Nichols, *et al.*, Astron. Astrophys. **344**, 231 (1999).
16. A. Kaufer, O. Stahl, B. Wolf, *et al.*, Astron. Astrophys. **305**, 887 (1996).
17. A. F. Kholtygin, *Wolf-Rayet Stars: Binaries, Colliding Winds, Evolution, IAU Symp. 163,* Ed. by K. A. van DerHucht and P. M. Willams (Kluwer Acad. Publ., Dordrecht, 1995), p. 160.
18. A. F. Kholtygin, *All-Russian Astron. Conf., August 6–12, 2001* (St. Petersburg, 2001), p. 186.
19. A. F. Kholtygin, F. V. Kostenko, N. A. Kudryashova, and L. M. Oskinova, Astron. Soc. Pac. Conf. Ser. **204**, 227 (2000).
20. A. F. Kholtygin, J. C. Brown, J. P. Cassinelli, *et al.*, Astron. Astrophys. Trans. (2002) (in press).
21. N. A. Kudryashova and A. F. Kholtygin, Astron. Zh. **78**, 333 (2001) [Astron. Rep. **45**, 287 (2001)].
22. S. Lépine and A. F. J. Moffat, Astrophys. J. **514**, 909 (1999).
23. S. Lépine, A. F. J. Moffat, and R. N. Henriksen, Astrophys. J. **466**, 392 (1996).
24. S. Marchenko and A. F. J. Moffat, Astrophys. J. Lett. **499**, L195 (1998).
25. F. A. Musaev, Astron. Lett. **22**, 715 (1996).
26. S. P. Owocki, in *Proceedings of 2nd Guillermo Haro Conf.*, Ed. by J. Franco and A. Carraminana (Cambridge Univ. Press, Cambridge, 1998), p. 350.
27. D. H. Roberts, J. Lehar, and J. W. Dreher, Astron. J. **93**, 968 (1987).
28. C. Schrijvers, J. H. Telting, C. Aerts, *et al.*, Astron. Astrophys., Suppl. Ser. **121**, 343 (1997).
29. V. S. Shergin, A. Yu. Kniazev, and V. A. Lipovetsky, Astron. Nachr. **317**, 95 (1996).
30. V. V. Vityazev, *Analysis of Unevently Spaced Time Series* (Izd. St. Petersburg Gos. Univ., St. Petersburg, 2001).
31. R. F. Wilson, *III/21 General Catalogue of Stellar Radial Velocity* (Carnegie Institution of Washington, Washington D. C., 1953), Publ. 601.

Translated by V. Astakhov

Astronomy Letters, Vol. 29, No. 3, 2003, pp. 188–194. Translated from Pis'ma v Astronomicheskiĭ Zhurnal, Vol. 29, No. 3, 2003, pp. 223–229.

Optical Brightness Variability of LSI+61°303: Improving the Photometric Period

G. V. Zaitseva* **and G. V. Borisov**

Sternberg Astronomical Institute, Moscow State University, Universitetskiĭ pr. 13, Moscow, 119992 Russia

Received September 11, 2002

Abstract—The UBV observations of the variable radio source LSI+61°303 carried out at the Crimean Station of the Sternberg Astronomical Institute in 1989–1990 and 1999–2002 are presented. We constructed a combined light curve of the star spanning ~6400 days from our and published data. Slow brightness variability with an amplitude of $\sim 0^m.1$ was detected. Using the entire combined series, we searched for a periodicity in a frequency range close to the radio period $P = 26^d.5$. The optical period was found to be exactly equal to the radio period. The shape and amplitude of the mean curves constructed with the radio period change from V to U: the detected double wave shows up most clearly in the U band.

Key words: *radio sources, photoelectric observations, light curves.*

INTRODUCTION

In searching for variable radio sources in the Galactic plane in August 1977, Gregory and Taylor (1978) discovered the highly variable radio source GT 0236+610. The authors identified it with the optical star LSI+61°303. Subsequently, the Einstein observations (Bignami *et al.* 1981) revealed an X-ray source that coincided with LSI+61°303 to within 1″. Based on their spectroscopic studies, Gregory *et al.* (1979) determined the spectral type of the star, B0–1, and its distance from the Sun, 2.3 kpc. The spectrum of LSI+61°303 exhibits unusually broad Hα and Hβ emission lines. Radio outbursts occur periodically. Taylor and Gregory (1982) found the outburst period to be 26.52 days. Coe *et al.* (1983) independently confirmed this period.

After the radio source GT 0236+610 was identified with the optical star LSI+61°303, a study of its optical variability was initiated. The historical light curve was constructed from Harvard plates spanning approximately 100 years, starting in 1885 (Gregory *et al.* 1979). The yearly mean magnitude estimates showed a variability in B reaching $0^m.7$. The star was designated as V615 Cas in the General Catalogue of Variable Stars (Kholopov *et al.* 1985). The type of its variability did not fit in with the universally accepted classification. Photoelectric observations (Lipunova 1988) revealed variations reaching $0^m.07$–$0^m.08$ in several days and rapid variations reaching $0^m.07$–$0^m.08$ on time scales of several tens of minutes.

Periodic brightness modulation with the same period (~26.5 days) as that in the radio frequency range was observed by Mendelson and Mazeh (1989) in the V and I bands and subsequently confirmed by Paredes *et al.* (1994) in the optical and infrared wavelength ranges. This periodicity could result from the orbital motion of a compact object, presumably a neutron star, in an eccentric orbit around a hot B0–B0.5 star. The binary nature of the system was also confirmed by radial-velocity measurements (Hutchings and Crampton 1981), which revealed variability with a period of 26.5 days.

Here, we present our photoelectric observations performed in 1989–1990 and 1999–2002. Based on these observations and on published data, we constructed a combined V-band light curve of V615 Cas spanning ~6400 days and improved its photometric period. We also present the results of our time-resolved photometry.

OBSERVATIONS

We carried out our photoelectric UBV observations of V615 Cas with the 60-cm reflector at the Crimean Station of the Sternberg Astronomical Institute during two periods: in 1989–1990 and in 1999–2002. The comparison stars were HD 15785 (Hiltner 1956) and BD+60°544, located 12′ southeast of V615 Cas, whose magnitudes were determined on four different nights by referencing to the standard HD 15785: $V = 9^m.45$, $B-V = +0^m.56$,

*E-mail: hare@sai.crimea.ua

1063-7737/03/2903-0188$24.00

Table 1

JD 2400000+	V	$B-V$	$U-B$	JD 2400000+	V	$B-V$	$U-B$
47716.372	10.71	0.77	−0.23	51605.309	10.61	0.83	−0.29
47718.371	10.71	0.81	−0.19	51618.265	10.67	0.81	−0.31
47718.501	10.74	0.83	−0.39	51628.264	10.65	0.85	−0.32
47735.500	10.73	0.85	−0.35	51629.265	10.66	0.82	−0.29
47736.528	10.73	0.86	−0.30	51641.284	10.68	0.81	−0.30
47737.500	10.71	0.81	−0.35	51645.284	10.68	0.78	−0.32
47739.528	10.77	0.73	−0.26	51816.538	10.66	0.82	−0.29
47740.528	10.75	0.84	−0.38	51819.460	10.67	0.85	−0.31
47746.390	10.77	0.82	−0.32	51822.435	10.70	0.84	−0.25
47747.500	10.76	0.83	−0.37	51824.537	10.67	0.83	−0.46
47748.442	10.76	0.83	−0.26	51841.456	10.68	0.84	−0.28
47748.486	10.72	0.81	−0.37	51842.540	10.68	0.84	−0.25
47748.525	10.74	0.81	−0.36	51848.476	10.68	0.84	−0.29
47767.463	10.78	0.84	−0.31	51853.429	10.66	0.84	−0.27
47767.492	10.80	0.75	−0.30	51863.420	10.65	0.88	−0.25
47768.500	10.76	0.85	−0.37	51866.389	10.66	0.86	−0.33
47778.444	10.74	0.84	−0.36	51867.204	10.65	0.82	−0.37
47805.448	10.78	0.84	−0.33	51867.430	10.62	0.83	−0.31
47824.396	10.80	0.83	−0.35	51869.309	10.69	0.87	−0.31
47825.421	10.81	0.85	−0.34	51879.369	10.64	0.84	−0.30
47825.451	10.80	0.84	−0.33	51924.243	10.69	0.85	−0.32
47826.333	10.78	0.85	−0.36	51925.286	10.67	0.86	−0.32
47827.333	10.79	0.82	−0.37	51927.310	10.66	0.86	−0.28
47829.238	10.74	0.81	−0.37	51932.351	10.62	0.82	−0.28
47829.254	10.75	0.83	−0.35	51951.239	10.63	0.84	−0.28
47829.337	10.76	0.83	−0.34	52187.597	10.71	0.84	−0.28
47830.375	10.74	0.84	−0.35	52192.570	10.67	0.86	−0.30
47834.417	10.78	0.85	−0.36	52193.540	10.76	0.85	−0.33
47835.333	10.80	0.85	−0.36	52196.564	10.72	0.83	−0.32
47837.375	10.75	0.84	−0.35	52208.493	10.65	0.84	−0.28
47851.375	10.80	0.84	−0.33	52209.557	10.66	0.83	−0.28
47855.458	10.77	0.83	−0.24	52249.361	10.69	0.83	−0.29
47883.417	10.76	0.86	−0.34	52300.213	10.71	0.85	−0.30
47929.375	10.79	0.84	−0.37	52308.197	10.71	0.82	−0.31
48211.438	10.75	0.84	−0.34	52309.282	10.68	0.83	−0.31
51452.498	10.70	0.85	−0.29	52309.301	10.69	0.82	−0.30
51454.480	10.67	0.83	−0.28	52313.328	10.75	0.83	−0.36
51455.454	10.75	0.83	−0.32	52313.360	10.69	0.82	−0.29
51467.418	10.68	0.86	−0.30	52313.370	10.70	0.84	−0.33
51492.360	10.68	0.83	−0.28	52324.225	10.73	0.85	−0.36
51493.415	10.66	0.83	−0.28	52324.241	10.67	0.84	−0.29
51502.354	10.67	0.84	−0.29	52339.288	10.73	0.82	−0.37
51548.229	10.65	0.85	−0.34	52343.256	10.72	0.83	−0.32
51581.291	10.67	0.80	−0.28				

Table 2

Interval of observations, JD	Number of observations (V band)	Author
1 2 445 900–5935	20	Lipunova (1988)
2 446 256–6268	10	
2 2 446 039–6850	64	Mendelson and Mazeh (1989)
3 2 446 264–9034	105	Paredes *et al.* (1994)
4 2 447 716–8211	35	This paper
2 451 452–2324	52	
Total	286	

$U-B=-0\overset{m}{.}45$. All our measurements were made with a 27″ aperture. Note that there is a faint companion 11″ southeast of V615 Cas, which was within the 27″ aperture during our measurements. We estimated its contribution with respect to the variable star from a CCD image. This contribution is ∼11% in the V band and ∼8% in the B and U bands. The error of a single measurement did not exceed 1–2% in any of the bands. Table 1 contains our observations reduced to Johnson's system. If several measurements of the star's brightness were carried out during the same night, then they were not averaged, and the table gives individual measurements, so that all data points are of the same weight.

LONG-TERM VARIABILITY

To study the variability of V615 Cas on long time scales (several thousand days), in addition to our measurements, we used the densest series of V-band photoelectric observations by other authors. Table 2 gives information on the observations used.

The observations of Mendelson and Mazeh (1989) are given in their instrumental system with respect to the comparison star HD 15570. Their observations partly overlap with our observations in time and their mean V magnitudes in this interval match our values within the error limits. Thus, we conclude that the instrumental system of Mendelson and Mazeh (1989) is close to Johnson's international photometric system and shows no systematic deviation from our measurements. The same can be said about the observations of Paredes *et al.* (1994). The second set of observations by Lipunova (1988) was carried out with the same telescope, the same equipment, and the same aperture as those used in our observations. The mean magnitudes estimated from the Crimean observations of Lipunova (1988) and from our observations are $V=10\overset{m}{.}77\pm0\overset{m}{.}03$ and $10\overset{m}{.}76\pm0.03$, respectively. Thus, in 1984–1993, the data of different authors nicely complement each other and reveal no appreciable systematic trend. According to the 1999–2002 observations, V615 Cas became, on average, appreciably brighter. The mean brightness was $V=10\overset{m}{.}75$ for 1984–1993 and $10\overset{m}{.}68$ for 1999–2002; i.e., higher by $0\overset{m}{.}07$. Thus, apart from the fluctuations during individual nights and from night to night reaching $0\overset{m}{.}07$ in two or three hours, V615 Cas also exhibits long-term variability. Figure 1 shows all the V-band observations in 1984–2002.

PHOTOMETRIC PERIODICITY

To analyze the star for periodicity, we used all of the V observations listed in Table 2, i.e., 286 observations spanning 6424 days. Our goal was to improve the period that was previously revealed by the more limited photometric data of Mendelson and Mazeh (1989) and Paredes *et al.* (1994). For a periodicity analysis, we eliminated the slow component from the data file by applying a correction of $+0\overset{m}{.}07$ to the 1999–2002 observations. We performed our analysis by using the Fourier technique in the frequency range from 0.005 to 0.08 d^{-1}, which includes the frequency corresponding to the radio period. The frequency step was chosen to be $0.2T^{-1}=3\times10^{-5}$ d^{-1}, where T is the total interval of observations (6400 days). The derived periodogram is shown in Fig. 2. The highest peak corresponds to the period of $26\overset{d}{.}497\pm0\overset{d}{.}010$. The formal accuracy of determining this period is low but, first, it is exactly equal to the radio period improved by Taylor and Gregory (1984), $26\overset{d}{.}496\pm0\overset{d}{.}008$, and, second, this is the highest peak in the power spectrum. Thus, we conclude that the optical data contain a periodicity with the period exactly equal to the radio period.

Figure 3 shows the mean V-band light curve constructed from all of the observations in Table 2. The data were folded with the improved radio period of $26\overset{d}{.}496$ (Taylor and Gregory 1984) and the initial epoch $2\,443\,366\overset{d}{.}775$ (Taylor and Gregory 1982). Each

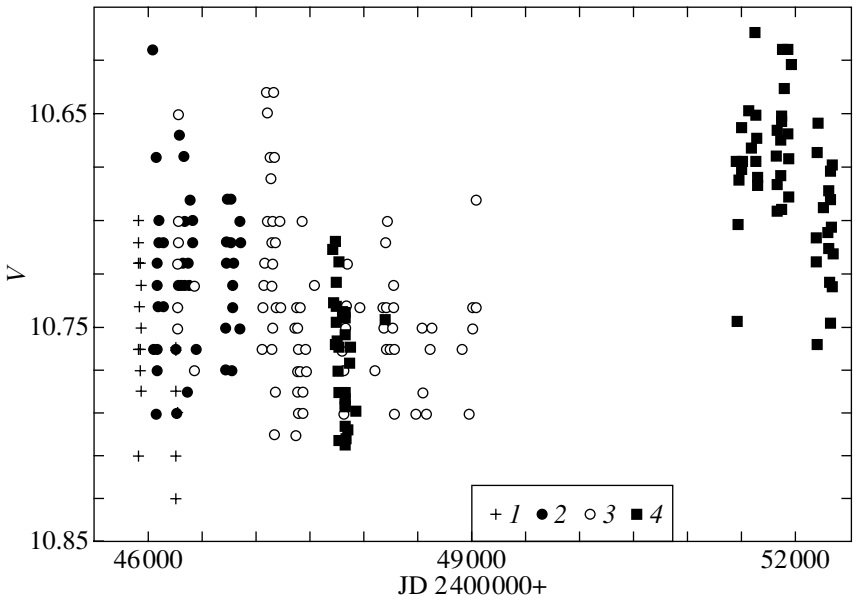

Fig. 1. The combined V-band light curve of V615 Cas in 1984–2002. (*1*) The observations of Lipunova (1988), (*2*) the observations of Mendelson and Mazeh (1989), (*3*) the observations of Paredes *et al.* (1994), and (*4*) our observations.

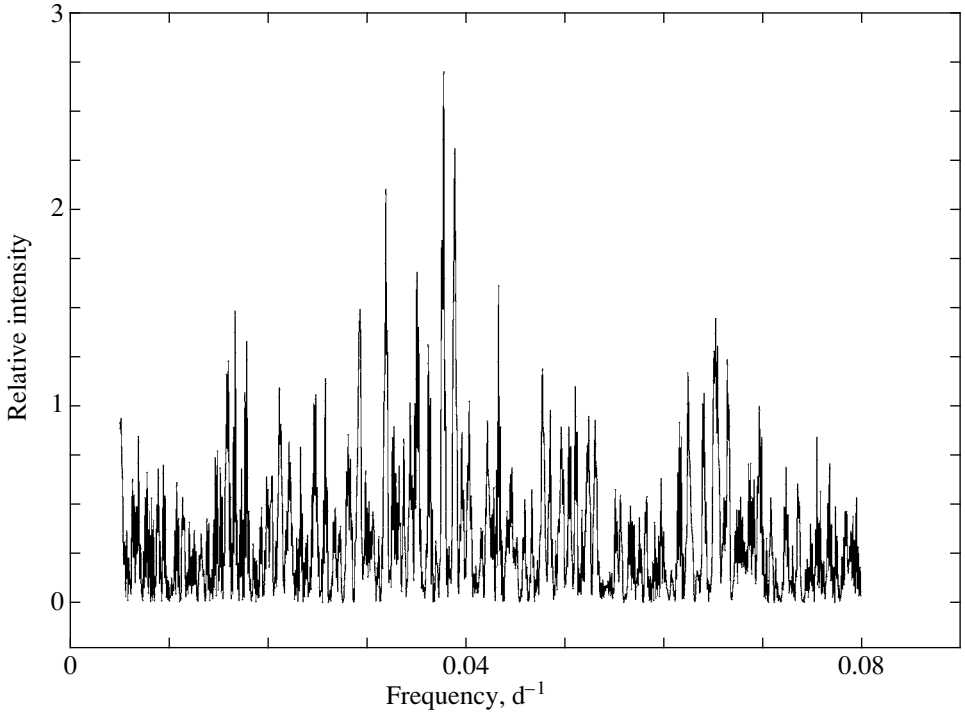

Fig. 2. The periodogram constructed from all of the V-band observations ($N = 286$) in the frequency range from 0.005 to 0.08 d^{-1} corresponding to the periods from 200 to 12.5 days. The highest peak corresponds to the period of $26\overset{d}{.}497$.

data point in the plot was obtained by averaging about 35 magnitudes over a 0.125 phase interval, with the shift of the interval by half. The rms error is indicated for each data point. The scatter of data points on the mean curve exceeds the measurement errors, is about $0\overset{m}{.}1$, and is attributable to the actual variability.

The periodicity amplitude is $\sim 0\overset{m}{.}04$. The highest brightness occurs at phase 0.85. The same phase of the maximum was determined by Mendelson and

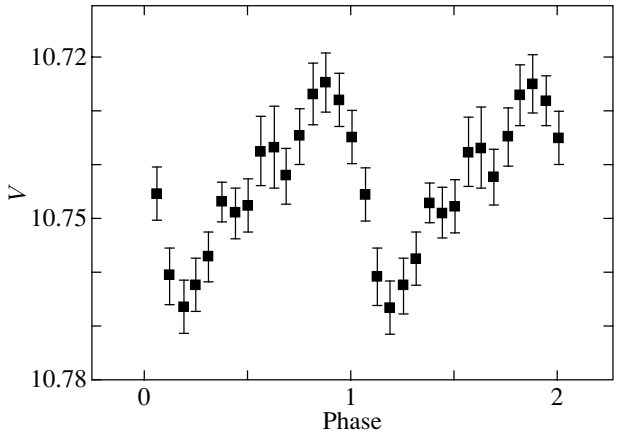

Fig. 3. The mean V-band light curve folded with the $26^{d}.496$ period. The initial epoch is $E_0 = 2\,443\,366.775$.

Mazeh (1989) for the V and I bands. Note that the mean light curve deviates from a sine wave, showing a gentler brightness rise and a steeper decline.

It is of interest to trace the changes in the shape and amplitude of the mean light curve in the different UBV color bands. To this end, we used only those observations which were reduced to Johnson's international system, because, in general, the uncertainties of insufficiently rigorous reduction have a stronger effect in the B and U bands. The number of such observations was 117 [the observations by Lipunova (1988) and our observations]. Figure 4 shows the UBV light curves obtained with the same light elements as those used to construct Fig. 3. A more rigorous selection of observational data led us to the following fundamentally new conclusions. A second wave appeared in the mean UBV light curves, with its amplitude increasing from V to U. Thus, whereas the amplitude of the maximum at phase 0.85–0.90 was almost constant when passing from V to U, being, on average, $0^{m}.045$, the amplitude of the maximum at phase 0.40 increased, being $0^{m}.015$, $0^{m}.025$, and $0^{m}.040$ in the VBU bands, respectively. The asymmetry of the second wave in B and V (a gentler rise and a steeper decline) ceased to be noticeable in U. However, this effect (the absence of apparent asymmetry in the second wave in the U band) can result from the large scatter of observational data in the ultraviolet.

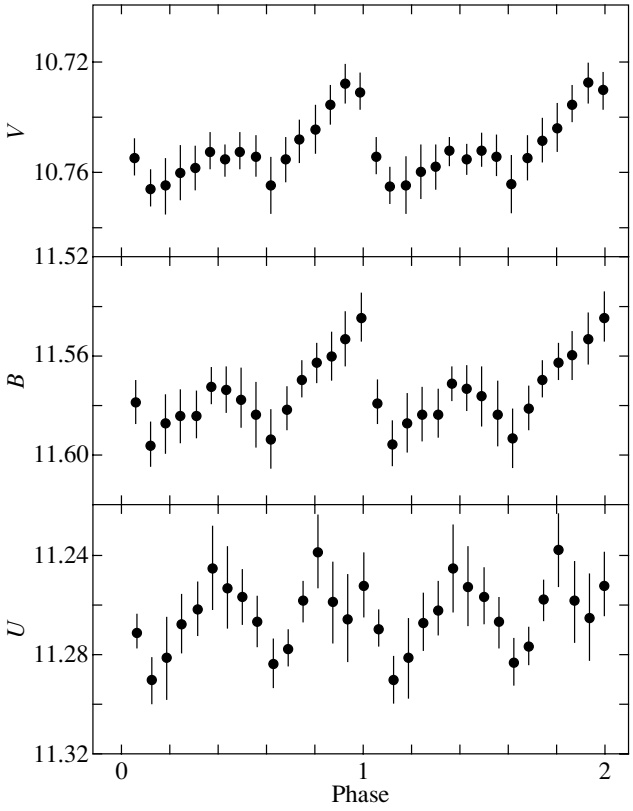

Fig. 4. The mean VBU light curves. The elements are the same as those used to construct Fig. 3.

RAPID VARIABILITY

Both large-scale brightness variations attributable to the ejection of the Be star's envelope and faster brightness variations from night to night and during the night are characteristic of the Be stars. Thus, in the system A0535+26, Lyuty and Zaitseva (2000) observed fluctuations with a 1400-day quasi-period and faster fluctuations reaching $0^{m}.1$ in two or three days and $0^{m}.05$ in several hours. In V615 Cas, Lipunova (1988) observed brightness variations on shorter time scales, by $0^{m}.07$–$0^{m}.09$ in several tens of minutes. In the same star, Bartolini *et al.* (1983) detected fluctuations reaching $0^{m}.03$ on time scales of the order of an hour.

Our observations for rapid variability with the same equipment as that used by Lipunova (1988) were carried out on four nights with stable transparency. Our observations on August 9/10 and 28/29, 1989, were performed for two hours and one hour, respectively, and showed no variations exceeding the measurement errors. The measurements on September 8/9 were made in the B band for two hours and revealed variability up to 10%. The densest and longest series of observations was obtained on July 10/11, 1989 (JD 2447718; Fig. 5). The measurements were carried out sequentially in the V, B, and U bands with a 10-s integration time. The mean statistical error of each measurement was $0^{m}.009$, $0^{m}.010$, and $0^{m}.040$ in the V, B, and U bands, respectively. The comparison star was observed between the measurements of the variable.

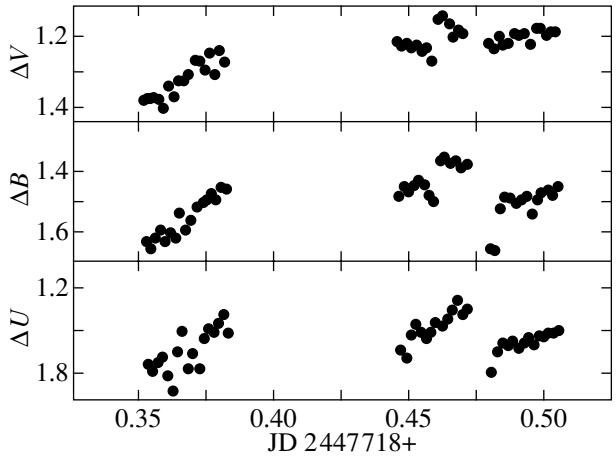

Fig. 5. Results of the observations of V615 Cas for rapid variability on July 10–11, 1989: the V, B, and U magnitude differences between V615 Cas and the comparison star. Each data point was obtained with a 10-s integration time.

During the first set of observations, the star gradually brightened by $0^m.2$ in V and B and by $0^m.6$ in U in 40 min. During the second set of observations, the star remained at a high brightness level in V, while its brightness variations in B and U were irregular in pattern.

The observations of rapid variability in Be stars are few in number, and it was inadequately studied, although there is certain evidence for microvariability in this class of objects. A two- or three-channel photometer is needed to study the low-amplitude variability on short time scales in more detail.

CONCLUSIONS AND DISCUSSION

Our main results are as follows.

(1) Based on our photoelectric observations and published data, we constructed a combined V-band light curve of the star LSI+61°303 = V615 Cas in a time interval of ~ 6400 days. The star exhibits long-term, low-amplitude ($< 0^m.1$) variability.

(2) Our Fourier analysis of the entire series of observations spanning about 240 periods allowed the photometric period to be improved: $P = 26^d.497 \pm 0^d.010$. This value is exactly equal to the radio period. The maximum in the mean curve constructed with the elements $E_0 = 2443366.775$ and $P = 26^d.497$ occurs at phase 0.85.

(3) The detected double wave in the mean UBV light curves shows up most clearly in the U band.

A double wave in the orbital light curve is also observed for the X-ray binary Cyg X-1. However, in contrast to LSI+61°303, the amplitude of this wave is the same in all the UBV bands, because the double-wave effect in Cyg X-1 is attributable to the geometrical factor of the optical component being ellipsoidal. By contrast, in LSI+61°303, physical factors, for example, the possible presence of an accretion disk, can be responsible for the appearance of a double wave in the light curve and for the increase in the amplitude of the second wave in the ultraviolet.

The I-band observations by Mendelson and Mazeh (1994) also revealed a modulation with the radio period, with the shape of the mean light curve (a gentler brightness rise and a steeper decline) and its amplitude ($\approx 0^m.04$) being similar to those which we obtained for the V band. The mean curve for the $(I - B)$ color index has the same shape but a lower amplitude ($0^m.02$). The system becomes redder at maximum optical light. The same color–magnitude relation is observed for the X-ray binary A0535+26 whose $(B - V)$ color curve is, in a sense, a mirror reflection of the V light curve (Lyuty and Zaitseva 2000; Clark *et al.* 1999).

A study of the various features in the Hα emission line (Zamanov *et al.* 1999) also revealed their variability with the radio period. This is the first case where a relationship was established between the period of radio outbursts and the disk surrounding a Be star.

The source LSI+61°303 is similar to Circinus X-1 and Cygnus X-3, which are also X-ray sources with periodic radio outbursts, but it is brighter at optical wavelengths and, hence, is easier to study optically. On the other hand, however, its variability amplitude is only a few hundredths of a magnitude and a two- or three-channel photometer is needed for its high-accuracy observations.

ACKNOWLEDGMENTS

We are grateful to V.M. Lyuty and A.E. Tarasov for valuable remarks.

REFERENCES

1. C. Bartolini, P. Custodi, F. Dell'Atti, *et al.*, Astron. Astrophys. **118**, 365 (1983).
2. G. F. Bignami, P. A. Caraveo, R. C. Lamb, *et al.*, Astrophys. J. **247**, L85 (1981).
3. J. S. Clark, V. M. Lyuty, G. V. Zaitseva, *et al.*, Mon. Not. R. Astron. Soc. **302**, 167 (1999).
4. M. J. Coe, S. R. Bowring, A. J. Court, *et al.*, Mon. Not. R. Astron. Soc. **203**, 791 (1983).
5. P. C. Gregory and A. R. Taylor, Nature **272**, 704 (1978).
6. P. C. Gregory, A. R. Taylor, D. Crampton, *et al.*, Astron. J. **84**, 1030 (1979).
7. J. B. Hutchings and D. Crampton, Publ. Astron. Soc. Pac. **93**, 486 (1981).

8. W. A. Hiltner, Astrophys. J., Suppl. Ser. **2**, 389 (1956).
9. P. N. Kholopov, N. N. Samus', V. P. Goranskii, *et al.*, *General Catalog of Variable Stars* (Nauka, Moscow, 1985–1988), Vol. 1.
10. N. A. Lipunova, Astron. Zh. **65**, 99 (1988) [Sov. Astron. **32**, 52 (1988)].
11. V. M. Lyuty and G. V. Zaitseva, Pis'ma Astron. Zh. **26**, 13 (2000) [Astron. Lett. **26**, 9 (2000)].
12. H. Mendelson and T. Maseh, Mon. Not. R. Astron. Soc. **239**, 733 (1989).
13. H. Mendelson and T. Mazex, Mon. Not. R. Astron. Soc. **267**, 1 (1994).
14. J. M. Paredes, P. Marziani, J. Marti, *et al.*, Astron. Astrophys. **288**, 519 (1994).
15. A. R. Taylor and P. C. Gregory, Astrophys. J. **255**, 210 (1982).
16. A. R. Taylor and P. C. Gregory, Astrophys. J. **283**, 273 (1984).
17. R. K. Zamanov, J. Marti, J. M. Paredes, *et al.*, Astron. Astrophys. **351**, 543 (1999).

Translated by N. Samus'

Astronomy Letters, Vol. 29, No. 3, 2003, pp. 195–198. Translated from Pis'ma v Astronomicheskiĭ Zhurnal, Vol. 29, No. 3, 2003, pp. 230–233.

The Orbital Period of Nova Aquilae 1999 No. 2 (V1494 Aql)

E. A. Barsukova[1*] and V. P. Goranskii[2]

[1] *Special Astrophysical Observatory, Russian Academy of Sciences, Nizhni Arkhyz, Karachaĭ-Cherkessian Republic, 357147 Russia*

[2] *Sternberg Astronomical Institute, Moscow State University, Universitetskiĭ pr. 13, Moscow, 119992 Russia*

Received October 9, 2002

Abstract—The photometric monitoring of Nova V1494 Aql at the Sternberg Astronomical Institute and at the Special Astrophysical Observatory in July and September 2002 has confirmed that the star is an eclipsing system. Its orbital period was improved, $0^d.1346141(5)$. Light elements and eight mid-eclipse times are given. The light-curve shape suggests that the star is an intermediate polar. © *2003 MAIK "Nauka/Interperiodica".*

Key words: *stars—variable and peculiar, stars—properties, classification.*

INTRODUCTION

Nova V1494 Aql ($19^h23^m05^s.38$, $+4°57'20''.1$, 2000) was discovered by Pereira (1999) on December 1, 1999, at 18^h50^m UT, when its brightness was 6^m vis. A faint star, $15^m.6$ r and $17^m.4$ b (USNO A2.0) is seen in the Digitized Sky Survey (DSS) images at its position. The star reached its maximum brightness of $3^m.9$ vis on December 2, 1999 (JD 2451515.7). V1494 Aql belongs to the group of fast FeII novae. The time of its brightness decline by 2^m and 3^m after maximum was 6.1 and 15.8 days, respectively. At the transition phase (JD 2451533–2451640) that began on the seventeenth day after the brightness maximum, the star exhibited quasi-periodic oscillations with periods from 7 to 22 days and with an amplitude reaching $1^m.5$. It is suggested that the novae with oscillations at the transition phase could be intermediate polars—binary systems with magnetic white dwarfs surrounded by an accretion disk outside their magnetospheres (Retter *et al.* 2000a; Retter 2002).

On August 6, 2000, V1494 Aql was observed for several hours in X-rays from the Chandra satellite as a supersoft X-ray source similar in spectrum to CAL 83 in the Large Magellanic Cloud (Starrfield and Drake 2001). The soft X-ray source was located on the surface of the white dwarf where nuclear reactions were still continuing at that time. A fast X-ray outburst with a sixfold rise above the normal level occurred during the observing session. The outburst had a complex structure and a hard X-ray component in its spectrum. Pulsations with a period of 2523 s were also observed, and they were interpreted as nonradial g-mode pulsations of a hot white dwarf (Starrfield *et al.* 2001; Krautter 2002). Krautter also reported orbital modulation with a period of 11635 s ($0^d.13466$).

An orbital period of 0.13467 ± 0.00002 was also found in the optical light curve (Retter *et al.* 2002b). The light curve in 2001 was reported to be an eclipsing one with two brightness minima, $0^m.5$ and $0^m.1$ deep, in the R band (Bos *et al.* 2001). Note that no X-ray eclipses were observed during the long Chandra sessions. The light elements for the eclipses have not yet been published.

We carried out a photometric monitoring of V1494 Aql in 2002, determined its accurate light elements, and studied its light curve.

PHOTOMETRY

First, we photometrically monitored V1494 Aql for 13 nights in July 2002 using the 60-cm Zeiss telescope at the Crimean Station of the Sternberg Astronomical Institute (SAI) equipped with SBIG ST-7 and ST-8 CCD arrays in a band close to Johnson's V band. On each night, we also obtained one or two observations in the B, R_J, and I_J bands to determine the color indices. Subsequently, two months later, for four nights in early September 2002, we continued our observations in the V band using the 1-m reflector at the Special Astrophysical Observatory (SAO) equipped with a photometer and a K-585 CCD array. The R and I bands in this photometer were such that the system response curves were close to those of Cousins's system. The exposure times ranged from 100 to 300 s. The total time of our observations was JD 2 452 458–2 452 523 (65 days).

*E-mail: bars@sao.ru

1063-7737/03/2903-0195$24.00

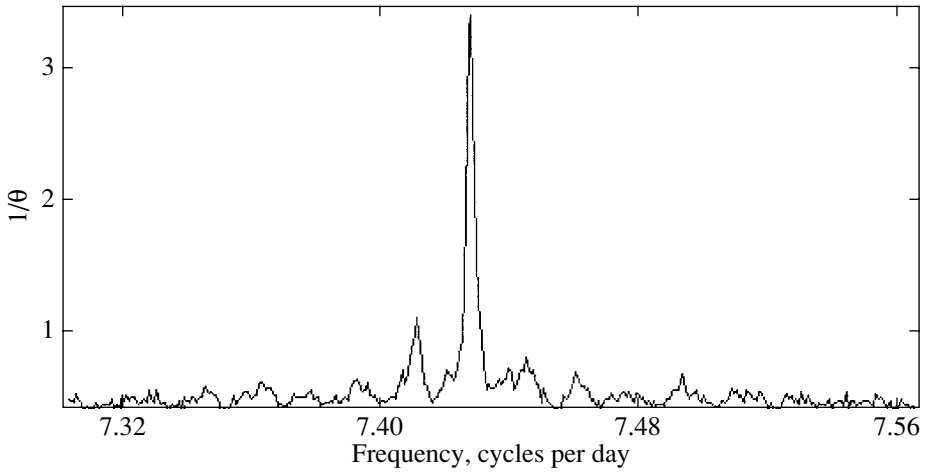

Fig. 1. The periodogram of V1494 Aql in a narrow range of periods near the orbital period.

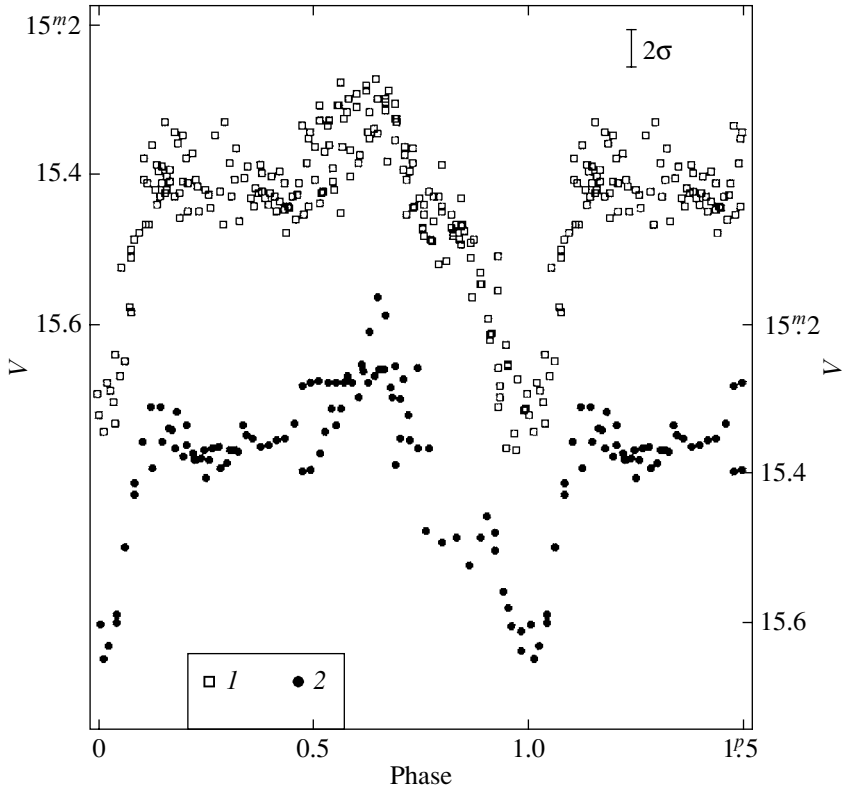

Fig. 2. The V-band light curves of V1494 Aql. *1*, July 2002 (SAI) and *2*, September 2002 (SAO).

We reduced our observations using the photometric code written by Goranskii and running it in the Windows operating system. The comparison star was GSC 473.4227 ($V = 13.86$, $B - V = 1.22$, $V - R_J = 0.92$, $V - I_J = 1.81$); its magnitudes were referenced to the $UBVRI$ standard sequence near SS 433 (Shakhovskoĭ and Sazonov 1996). Our measurements of check stars confirmed that the brightness of the comparison star was constant.

When measuring the star in the best images obtained at the SAO with $1''.0$–$1''.5$ seeing, we detected a close companion at an angular distance of $1''.1$ southwest of the Nova. We used the image separation technique to determine its magnitudes, $V = 18^m.1 \pm 0^m.15$ and $R_C = 16^m.20 \pm 0^m.02$. Since the companion is red, its contribution to the R_C band is large, $\approx 34\%$; in the V band, it is much smaller, $\approx 7\%$. The accuracy

of our measurements of the total V brightness is high, $0^m.02-0^m.03$.

THE LIGHT CURVE OF V1494 Aql

During our observations, the brightness of V1494 Aql varied within the range $15^m.16-15^m.86$ V. The color indices were, on average, $B-V=0^m.9$, $V-R_J=0^m.3$, and $(R-I)_J=0^m.7$. The close companion undoubtedly affected the colors by making them redder. The rapid irregular brightness fluctuations did not exceed 5%.

In two months, the mean brightness of the star changed by $\Delta=-0^m.07$; i.e., it rose, despite the general tendency for brightness decline. To perform a frequency analysis, we eliminated this difference between the two photometric series. We checked periodicity using the method for seeking periodicity from the minimum dispersion of the light curve by Lafler and Kinman (1965). The periodogram near the sought-for period is shown in Fig. 1. In this figure, the frequency $(1/P)$ and $1/\theta$, where θ is the Lafler–Kinman parameter, are plotted along the x and y axes, respectively. The best period corresponding to the minimum dispersion of the light curve is $0^d.134610$. The light curve is actually eclipsing in pattern, with the eclipse depth and width being about $0^m.25$ and $0^p.20=39$ min, respectively. Below, we give our mid-eclipse times. The times determined either from the ascending branch of the eclipse or from its descending branch are presented with less decimal digits. The accuracy of determining the eclipse time from the complete curve is $0^d.0002$.

JD hel. 2452000+	JD hel. 2452000+
458.324	471.513
458.4580	473.533
462.4967	519.3042
464.5164	520.2460

We determined the following linear elements from the five most reliable mid-eclipse times:

$$\text{Min I hel.} = 2\,452\,462.4966 \pm 2 + 0^d.1\,346\,141 \pm 5 \times E.$$

Figure 2 shows the light curve constructed from our original SAO and Crimean observations. The light curve appears quite unusual: in addition to the eclipse, we see a hump with a mean amplitude of $0^m.13$ at phases 0.48–0.75, with the maximum at phase 0.645. Ordinary cataclysmic variables also exhibit humps in their orbital light curves, but with the maxima at phases 0.75–0.80. The humps in cataclysmic variables result from the radiation of a hot spot at the edge of an accretion disk where the gaseous flow of the outer disk edge collides with the gaseous flow falling from the secondary component. The eclipse profiles of eclipsing cataclysmic variables show a step—a sharp brightness decline due to the shielding of hot spot by the secondary component. The hump radiation in Nova V1494 Aql disappears at phase 0.75, i.e., at the system elongation, when no eclipse is possible, and the eclipse begins at phase 0.88. Our Crimean observations show a normal out-of-eclipse brightness, a shoulder in the light curve, between phases 0.75 and 0.88, whereas our SAO observations show a similar shoulder but with the brightness reduced by $0^m.12$ relative to its out-of-eclipse level. The changes in brightness at the shoulder phases can result from changes in the accretion rate and absorption of the disk radiation by the accretion flow. During the nova outburst, accretion is undoubtedly enhanced through additional heating of the secondary component. No eclipse of the light source responsible for the hump in the light curve is seen in the eclipse profile, because this source disappears even before the eclipse.

We believe this light source to be an accretion column at one of the poles of the white dwarf with a magnetic field. Since the phase of the hump maximum is almost constant with time, we can conclude that the rotation of the white dwarf is synchronized with the orbital motion. Future observations can answer the questions of how accurate this synchronization is and whether it was broken after the nova outburst. Thus, our observations indicate that the system was in the stage of an intermediate polar in the summer of 2002. Since X-ray observations of the supersoft X-ray source revealed no eclipses, the orbital inclination is such that the white dwarf in this system is not eclipsed and part of the accretion disk is shielded at the primary eclipse.

According to the observations of Retter *et al.* (2002b), for 31 nights in July and August 2000, the light curve with a period of 0.13467 ± 0.00002 days was a double wave with unequal minima, with $0^m.07$ and $0^m.03$ amplitudes in the R band. One year later, the eclipse depths were $0^m.5$ and $0^m.1$ in the R band, with the period being the same (Bos *et al.* 2001). Nothing was reported on the appearance of a hump in the light curve. Our light curve shows no traces of the secondary eclipse. On the contrary, the brightness at these phases begins to increase because a hump appears. Besides, the difference between our period and the period from Retter *et al.* (2002b) is large and statistically significant. Unfortunately, since there is no date of minimum in Retter *et al.* and Bos *et al.*, we cannot establish how stable the period has been in the last three years. Clearly, the shape of the light curve for V1494 Aql varies significantly.

CONCLUSIONS

Our photometry for V1494 Aql confirms that the star is an eclipsing system with a period of $0^d.1346141$, which was determined from a 65-day time interval in July–September 2002. We gave light elements and eight mideclipse times. Partial eclipses of the accretion disk occur in the system.

The light-curve shape is highly variable. A hump appeared in the light curve with its maximum intensity observed at the orbital phase 0.645 unusual for cataclysmic variables. No eclipse of the light source responsible for the hump takes place. The phase of the hump maximum did not change during our observations. These observations lead us to conclude that the hump radiation source is an accretion column on the surface of the white dwarf near its magnetic pole and that the rotation of the white dwarf is synchronized with the orbital motion. Thus, the system is an intermediate polar and an example that confirms the relationship of intermediate polars during outbursts to novae exhibiting oscillations at the transition phase on the descending branch of the light curve (Retter 2002).

REFERENCES

1. M. Bos, A. Retter, L. Cook, and R. Novak, IAU Circ. No. 7665 (2001).
2. J. Krautter, AIP Conf. Proc. **637**, 345 (2002).
3. J. Lafler and T. D. Kinman, Astrophys. J., Suppl. Ser. **11**, 216 (1965).
4. A. Pereira, IAU Circ. No. 7323 (1999).
5. A. Retter, L. Cook, R. Novak, *et al.*, IAU Circ. No. 7537 (2000b).
6. A. Retter, W. Liller, and G. Gerradd, New Astron. Rev. **40**, 65 (2000a).
7. A. Retter, Astron. Soc. Pac. Conf. Ser. **261**, 655 (2002).
8. N. M. Shakhovskoi and A. N. Sazonov, Pis'ma Astron. Zh. **22**, 580 (1996) [Astron. Lett. **22**, 517 (1996)].
9. S. Starrfield and J. Drake, *Two Years of Science with Chandra* (Washington, DC, 5–7 September 2001), Abstracts No. 50 (2001a).
10. S. Starrfield, J. Drake, R. M. Wagner, *et al.*, Bull. Am. Astron. Soc. **33**, 804 (2001b).

Translated by N. Samus'

Astronomy Letters, Vol. 29, No. 3, 2003, pp. 199–204. Translated from Pis'ma v Astronomicheskiĭ Zhurnal, Vol. 29, No. 3, 2003, pp. 234–240.

Parameters of the Intense X-ray and Gamma-ray Radiation from the Solar Flare of May 20, 2002, as Observed from the Coronas-F Spacecraft

A. V. Bogomolov[1], A. P. Ignat'ev[2], K. Kudela[3], S. N. Kuznetsov[1], Yu. I. Logachev[1], O. V. Morozov[1], I. N. Myagkova[1], S. N. Oparin[2], A. A. Pertsov[2], S. I. Svertilov[1*], and B. Yu. Yushkov[1]

[1] *Skobeltsyn Institute of Nuclear Physics, Moscow State University, Vorob'evy gory, Moscow, 119899 Russia*

[2] *Lebedev Institute of Physics, Moscow, 117924 Russia*

[3] *Institute of Experimental Physics, Slovak Academy of Sciences, Watsonova 47, SK-04353 Kosice, Slovakia*

Received July 18, 2002

Abstract—We consider temporal, spectral, and polarization parameters of the hard X-ray and gamma-ray radiation observed during the solar flare of May 20, 2002, in the course of experiments with the SONG and SPR-N instruments onboard the *Coronas-F* spacecraft. This flare is one of the most intense gamma-ray events among all of the bursts of solar hard electromagnetic radiation detected since the beginning of the Coronas-F operation (since July 31, 2001) and one of the few gamma-ray events observed during solar cycle 23. A simultaneous analysis of the Coronas-F and GOES data on solar thermal X-ray radiation suggests that, apart from heating due to currents of matter in the the flare region, impulsive heating due to the injection of energetic electrons took place during the near-limb flare S21E65 of May 20, 2002. These electrons produced intense hard X-ray and gamma-ray radiation. The spectrum of this radiation extends up to energies $\geq$7 MeV. Intense gamma-ray lines are virtually unobservable against the background of the nonthermal continuum. The polarization of the hard X-ray (20–100 keV) radiation was estimated to be $\leq$15–20%. No significant increase in the flux of energetic protons from the flare under consideration was found. At the same time, according to ACE data, the fluxes of energetic electrons in interplanetary space increased shortly ($\sim$25 min) after the flare. © *2003 MAIK "Nauka/Interperiodica".*

Key words: *Sun, flares, X-ray and gamma-ray radiation, energetic electron acceleration.*

INTRODUCTION

At present (during solar cycle 23), solar flares are detected in the hard electromagnetic spectral range from the HESSI and Coronas-F spaceborne observatories. However, the statistics of the flares during which relatively high-energy (>1 MeV) gamma-ray photons were detected is much poorer than that accumulated during the previous (20–22) cycles. Coronas-F detected more than ten flares during which hard X-ray and gamma-ray radiation was observed. Among these events, the flare of May 20, 2002, was most intense in the gamma-ray range.

The gamma-ray radiation from solar flares is currently believed to be a superposition of the lines produced in nuclear reactions and the continuum attributable to the bremsstrahlung of relativistic electrons. Information on the gamma-ray radiation from solar flares was obtained during the experiments carried out onboard the OSO-7, SMM, CGRO, Yokhoh, Gamma, Granat, and other satellites (Suri *et al.* 1975; Chupp *et al.* 1982). A total of about 300 gamma-ray flares were identified during solar cycles 20–22. However, the spectra with >4 lines were observed in no more than 30 events, while the line-rich spectra (>12 lines) were measured in fewer than 10 flares. For example, a total of 185 flares with an intensity of the gamma-ray radiation high enough to perform a thorough spectral analysis were detected during the GRS SMM experiment. However, gamma-ray radiation was observed in lines only for 67 flares (Rieger and Rank 2002). Thus, according to the statistics accumulated during this experiment, most ($\sim$65%) of the flares during which gamma-ray radiation was observed exhibited a continuum-type spectrum at energies up to $\sim$1 MeV. At the same time, the relatively small fraction of the flares with gamma-ray lines may be due to the poor statistics of the events observed at energies above 1 MeV, because the power-law continuum is determined mainly in the

*E-mail: sis@coronas.ru

energy range 0.3–1 MeV. Therefore, measurements of the solar-flare fluxes and spectra at energies above 1 MeV are of great importance.

The features of the gamma-ray spectrum in the energy range $E_\gamma < 10$ MeV generated during the interaction of accelerated ions with the solar atmosphere were theoretically predicted before the first direct measurements (Lingenfelter and Ramaty 1967). Subsequently, these predictions were confirmed experimentally. The spectrum in the energy range 0.01–10 MeV consists of the lines emitted by excited nuclei, the 0.511-MeV annihilation line, the 2.223 MeV line of neutron capture by hydrogen, the continuum due to the superposition of kinematically broadened lines, and the bremsstrahlung continuum of accelerated electrons. In general, the bremsstrahlung spectrum of energetic electrons can be satisfactorily fitted by a single power law over the energy range from several tens and several hundred keV up to energies of $\geq$8 MeV. However, power-law spectra with breaks (Rieger and Rank 2002) provide a better fit to the bremsstrahlung continuum of some impulsive flares. The line-rich spectra, for example, during the flares of April 27, 1981 (Murphy *et al.* 1991) and March 6, 1989 (Marshhauser *et al.* 1991), exhibit lines from the most abundant nuclei and the 0.511 and 2.223 MeV lines.

Note that as yet there is no comprehensive theory for the source of the particles responsible for the gamma-ray spectrum. Various working hypotheses are considered: the simultaneous acceleration of electrons and protons at the impulsive phase of the flare with the capture of the accelerated particles in the flare loop and with their subsequent precipitation into the solar atmosphere; prolonged acceleration in the post-flare loops that are formed at the solar-flare decay phase during the gradual relaxation of the magnetic field to its original state; and a combination of these limiting cases (Mandzhavidze and Ramaty 1992; Chupp *et al.* 1993; Mandzhavidze *et al.* 1993; Kahler 1992; Chertok 1995). Therefore, new experimental data on the gamma-ray radiation from solar flares are of current interest.

EXPERIMENTAL CONDITIONS AND OBSERVING TECHNIQUES

The Coronas-F satellite was launched on July 31, 2001, into a quasi-circular orbit with an altitude of 507 ± 21 km, an inclination of 82.5, and a period of 94.5 min. This satellite is a spaceborne observatory designed to study nonstationary processes on the Sun and their effects on the interplanetary medium and the Earth's magnetosphere.

To study the neutral radiation from solar flares on Coronas-F, the Research Institute of Nuclear Physics of Moscow State University in cooperation with the Lebedev Institute of Physics of the Russian Academy of Sciences and the Institute of Experimental Physics of the Slovak Academy of Sciences designed and installed the SPR-N instruments to record the X-ray radiation from solar flares in the energy range 15–100 keV and to measure its polarization (Bogomolov *et al.* 2003) and the SONG instrument to record hard X-ray radiation (HXR), line and continuum gamma-ray radiation, and neutron and relativistic electron fluxes (Kuznetsov *et al.* 1995).

SPR-N measures the polarization of the X-ray radiation from solar flares in the energy range 20–100 keV. In addition, the instrument makes it possible to measure in detail the time profile for the intensity of X-ray radiation in the energy range 15–100 keV, to determine the flux, and to estimate the spectral hardness in this energy range.

The polarization detector unit consists of a beryllium X-ray scatterer (a hexahedral prism with an effective area of $\sim$100 cm^2) and three pairs of scintillation detectors that measure the intensity of the scattered radiation. The optical thickness of the scatterer τ ($\tau^{-1} = \mu\rho$) determined by the mass absorption coefficient μ and by the density ρ varies with photon energy over the range from 2.5 cm ($E_\gamma = 20$ keV) to 4.1 cm ($E_\gamma = 100$ keV). For the given scatterer size, this determines the detection efficiency 70–86%.

The time resolution of the SPR-N polarization detectors is specified by the exposure time set by commands from the Earth within the range from 1 to 16 s. The output signals from the polarization detectors are measured in the 20–40, 40–60, and 60–100 keV channels. In addition, the count rates of the anticoincidence caps made of a plastic scintillator are measured.

Monitoring measurements of the solar X-ray radiation intensity are performed in the energy range 15–100 keV. The X-ray radiation is recorded with a CsI(Na) crystal 1.5 cm in diameter and 0.3 cm in thickness with an effective area of $\sim$2 cm^2. A cylindrical collimator that provides a $5^\circ \times 5^\circ$ field of view of the detector is located above this crystal. To protect the crystal from charged particles, it was placed behind an anticoincidence shield made of a plastic scintillator (phoswich). The count rates in the 15–40 and 40–100 keV channels of the patrol detector are measured continuously and independently of the measuring cycle of the polarization detectors and the modes of operation of the instrument.

The SONG instrument is part of the SKL scientific instrumentation produced at the Research Institute of Nuclear Physics of Moscow State University that was installed on the Coronas-F satellite and, previously, on the Coronas-I satellite (Kuznetsov

et al. 1995). This instrument is designed to record X rays and gamma rays in the energy range 0.028–100 MeV, neutrons with energies >20 MeV, electrons with energies 11–108 MeV, and charged particles—mostly protons with energies >70 MeV and electrons with energies >55 MeV. The particles are detected with a CsI(Tl) crystal 20 cm in diameter and 10 cm in height surrounded from all sides by an active anticoincidence shield made of 2-cm-thick plastic scintillator.

The neutrons in the SONG instrument are recorded by the charged products of their interaction with Cs and I nuclei. The dependence of the pulse shape in CsI(Tl) on specific particle ionization is used to identify neutrons against the background of gamma-ray photons. The instrument measures the X-ray and gamma-ray fluxes in the energy ranges 0.028–0.053, 0.053–0.15, 0.15–0.50, 0.50–1.3, 1.3–4, 4–7, 7–15, 15–26, 26–41, 41–60, and 60–100 MeV and the neutron fluxes in the energy-release ranges 4–7, 7–15, 15–26, 26–41, 41–60, and 60–100 MeV. SONG has a maximum effective area of ~38 and 270 cm^2 for neutrons and gamma-ray photons, respectively.

The background variations in the count rates of the instruments result mainly from variations in the radiation conditions in the orbit when the satellite passes through different regions of the near-Earth space. The background counts are attributable mainly to the contribution of the local gamma-ray radiation produced by the interaction of primary cosmic rays with the matter of the Earth's atmosphere, the satellite, and the instrument. The intense increases in the background count rate correspond to the times when the satellite crosses the spurs of the outer radiation belt in the Northern and Southern Hemispheres or the South Atlantic Anomaly (the inner belt). These are attributable to the additional counts in the instrument channels of the bremsstrahlung of energetic electrons in the radiation belt. The region of a low background count rate between the belt spurs corresponds to the low-latitude regions under the inner belt and to the polar cap regions.

RESULTS OF THE OBSERVATIONS OF THE SOLAR FLARE OF MAY 20, 2002

The strong 2N/2.1X solar flare of May 20, 2002, with the coordinates 21S and 65E commenced in soft X-ray radiation (SXR) at 15.21 UT and in Hα emission at 15.08 UT and reached its maximum at 15.27 UT and 15.29 UT, respectively (Coffey 2002).

Figure 1 shows the SPR-N and SONG time profiles of the HXR fluxes and the GEOS-8 time profiles (Raben 2002), which characterize the thermal X-ray radiation: the temperature of the radiation region calculated from the intensity ratio in the 0.5–4 and 1–8 Å channels and the time derivative of the intensity in the 0.5–4 Å channel, $dW(XS_h)/dt$. The count rates in the SPR-N and SONG channels were determined by subtracting the count rates corresponding to the latitudinal variations in the background X-ray and gamma-ray radiation from the original time series. The SONG count rates are given only for those time intervals in which the excess of the count rates above the background level was statistically significant.

As we see from Fig. 1, the duration of the increase in the 15–40 keV channel (~420 s) was considerably longer than the duration of the increases in harder channels (~60 s). The time variation of the intensity in the 15–40 keV channel (with an allowance made for the time resolution used) correlates with the time variation of the count rates in the wavelength range 0.5–4 Å. We can assume that the variation of the radiation intensity in the 15–40 keV channel, to some extent, is attributable to the contribution of the thermal radiation whose intensity is determined by the temperature of the emitting region. As the temperature decreases, the thermal radiation becomes softer and its contribution to the X-ray 15–40 keV flux significantly decreases. This effect determines the high sensitivity of the count rates in this energy range to temperature variations and, accordingly, a steeper falloff of curve *1* in comparison with curve *11*. At the same time, the intensity in the 40–100 keV SPR-N channels and in the SONG channels that record gamma-ray radiation peaks at the time of the maximum of the derivative $dW(XS_h)/dt$. This suggests that the hard X-ray and gamma-ray radiation recorded on the Coronas-F satellite at the flare peak is attributable to the bremsstrahlung of the energetic electrons injected at the time when the derivative $dW(XS_h)/dt$ reaches its maximum. The specific power in the SPR-N 15–40 keV channel at the flare peak was about 2×10^{-8} W/m^2. Note also that the main intense peak is followed by two much weaker peaks (at 15.27 and 15.28 UT), which are traceable up to energies ~0.5 MeV. Thus, the profiles shown in Fig. 1 suggest the presence of short peaks associated with the bremsstrahlung of energetic electrons against the background of the intense, slowly varying (presumably thermal) continuum observed in the channels with energies <40 keV. The two spectral components were simultaneously observed in the 15–40 keV channel (curve *1* in Fig. 1), which only covers the relatively high-energy part of the thermal spectrum. The thermal component is absent in curves *2–9*.

Figure 2 shows the energy spectrum that corresponds to the intensity peak of the hard X-ray and gamma-ray radiation. We see from the figure that

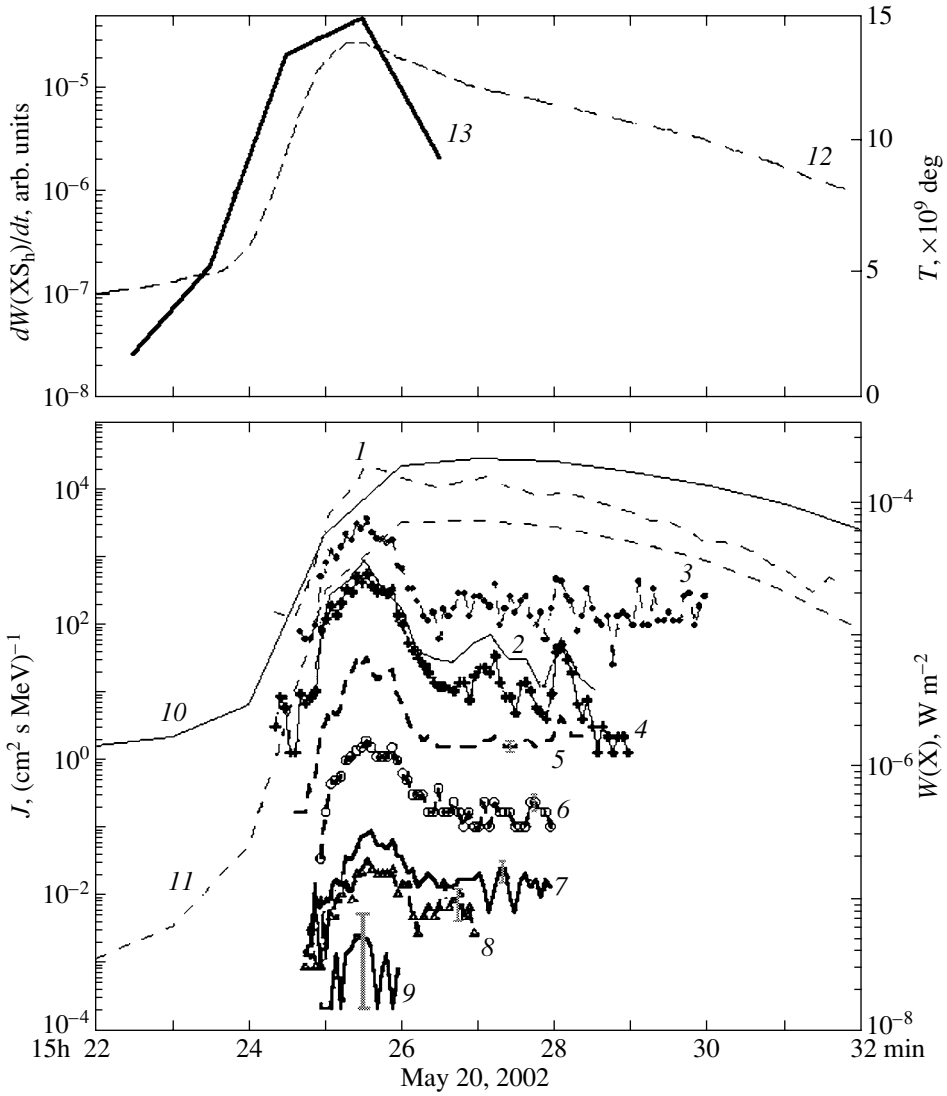

Fig. 1. Time profiles for the X-ray and gamma-ray fluxes. Lower panel: *1*, 15–40 keV (SPR-N); *2*, 40–100 keV (SPR-N); *3*, 0.028–0.054 MeV (SONG); *4*, 0.054–0.15 MeV (SONG); *5*, 0.15–0.5 MeV (SONG); *6*, 0.5–1.3 MeV (SONG); *7*, 1.3–4 MeV (SONG); *8*, 4–7 MeV (SONG); *9*, 7–15 MeV (SONG); *10*, 1–8 Å (GOES-8); and *11*, 0.5–4 Å (GOES-8). Upper panel: *12* is the temperature (K) in the region where thermal X-ray radiation is generated calculated from GOES data and *13* is $dW(XS_h)/dt$—the time derivative of the 0.5–4 Å channel. The statistical errors ($\pm\sigma$) for the SPR-N and SONG instruments at the flare time are also shown in Fig. 2.

except for the energy range 15–40 keV, the spectrum can be fitted by a single power law over the entire measured energy range:

$$J = (1.7 \pm 0.2)(E/E_0)^{-(2.5\pm0.2)}, \qquad (1)$$

where $E_0 = 1$ MeV and J is in photons cm^{-2} s^{-1} MeV^{-1}. In the 15–40 keV channel, the flux density is slightly higher than that given by dependence (1), which confirms the two-component structure of the radiation during this flare. The absence of statistically significant gamma-ray lines allows us to place this flare into the class of solar flares with an intense gamma-ray continuum. At the same time, as follows from Fig. 2, there can be an excess at energies 4–7 MeV attributable to gamma-ray lines. However, the statistical errors due to background counts do not give us grounds to assert that this excess is actually present. Comparison of the spectra measured with the SONG 240-channel analyzer before and during the flare revealed no significant spectral variations near the gamma-ray lines either.

Our estimates of the polarization of the hard radiation from the flare of May 20, 2002, yielded the following result: <20% (20–40 keV), <10% (40–60 keV), and <15% (60–100 keV). Thus, it can be concluded that the possible polarization of the hard

X-ray radiation from this flare does not exceed the theoretical estimates for the bremsstrahlung of a directed beam of accelerated electrons, which are 10–20% as derived by Zhitnik *et al.* (1989). At the same time, the flare location (near the limb), in principle, corresponds to favorable conditions for the detection of polarized electromagnetic radiation (Bogomolov *et al.* 2003).

Analysis of the count rates in the SONG neutron channels suggests that no neutrons were generated during the flare of May 20, 2002.

The charged-particle detectors installed on the GOES and ACE satellites detected no significant increases in the fluxes of energetic protons associated with the flare under consideration. However, the ACE satellite recorded a twofold increase in the flux of electrons with energies from several tens to several hundred keV near the libration point (Cooper 2002) immediately after the S21E65 flare of May 20, 2002.

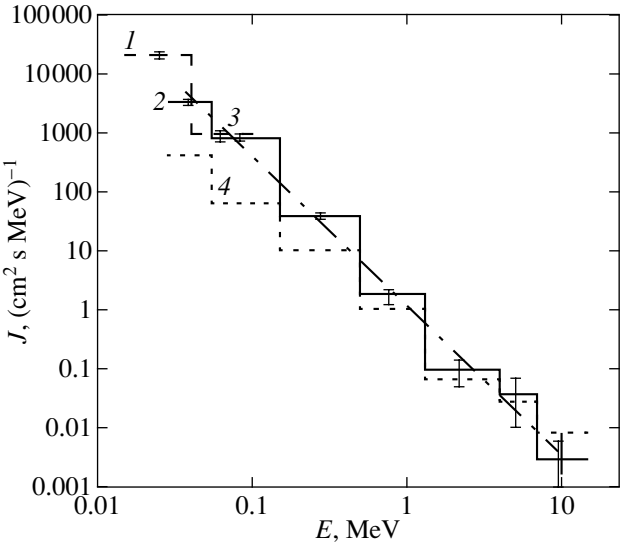

Fig. 2. The X-ray and gamma-ray spectrum measured with the SPR-N and SONG instruments during the flare of May 20, 2002, at the peak of its intensity ($\sim 15^h25^m30^s$ UT): *1*, SPR-N; *2*, SONG; *3*, the power-law fit obtained from all SONG channels (index $\gamma = -2.52$); *4*, the gamma-ray background spectrum in the SONG channels observed at the geomagnetic latitudes that correspond to the flare detection time.

DISCUSSION

As was pointed out above, during the flare of May 20, 2002, the intensity peak of the hard X-ray and gamma-ray radiation corresponded to the maximum time derivative of the intensity of the thermal X-ray radiation, i.e., to the maximum energy input into the emitting region. The time variation in the SPR-N 15–40 keV channel correlates with the time variation of the GOES count rate in the wavelength range 0.5–4 Å. We can assume that thermal photons contributed significantly to the count rate in the 15–40 keV channel, suggesting a high temperature of the emitting region. As we see from Fig. 1 (judging by the pulse of hard X-ray radiation that is shorter than the rise time of the thermal radiation), during the heating by the currents of the acceleration region, there was an intense precipitation of energetic electrons from the current-sheet discontinuity region into the chromosphere, which produced intense bremsstrahlung in the hard energy range. This precipitation resulted in additional strong heating of the emission region, which caused the temperature to increase by more than two orders of magnitude compared to the value that was reached through current heating.

The flare of May 20, 2002, under consideration was the closest (in time) solar event with respect to the electron flux increase in interplanetary space pointed out above (the preceding M5.0 flare occurred at 10^h52^m UT, while the succeeding C1.8 flare occurred at 18^h20^m UT). The flare of May 20, 2002, occurred at longitude E65 and the field line connecting the Earth and the Sun along the spiral of Archimedes was projected onto longitude W52 (the solar-wind velocity is $\sim$446 km s^{-1}), with the field-line length being $\sim$1.14 AU. Electrons with energies of 38 and 175 keV must spend $\sim$25.9 and 14.2 min in motion along a field line, respectively; i.e., if the flare occurred at longitude W52, then the electrons would have been delayed relative to bremsstrahlung by 17.6 and 5.9 min, respectively. However, the flare occurred at E65 and the actual delay was 15 ± 2.5 and 25 ± 2.5 min (we used 5-min electron data). Thus, for electrons with $E \sim 38$ keV, the delay, if it exists, is less than 1 min. The delay for electrons with $E \sim 175$ keV is $\sim$25 min. This contradiction may stem from the fact that the data on the electron flux increase are statistically unreliable.

Estimates show that even in the case of Bohm diffusion across field lines, the electrons will traverse an angular distance of 118° in a time $\sim 10^{10}$ s. Therefore, the flare may bear no relation to the emergence of electrons near the Earth.

REFERENCES

1. A. V. Bogomolov, Yu. I. Denisov, S. N. Kuznetsov, *et al.*, Astron. Vestnik (2003) (in press).
2. I. M. Chertok, Izv. Ross. Akad. Nauk, Ser. Fiz. **59,** 112 (1995).
3. E. L. Chupp, D. J. Forrest, J. M. Ryan, *et al.*, Astrophys. J. Lett. **263**, L95 (1982).
4. E. L. Chupp, H. Marschhauser, G. Trottet, *et al.*, in *Proceedings of 23rd ICRC* (Calgary Univ., Calgary, 1993), Vol. 3, p. 87.

5. H. E. Coffey, http://www.ndgc.noaa.gov/stp/SOLAR/gedata.html (2002).
6. J. F. Cooper, http://nssdc.gsfc.nasa.gov/space (2002).
7. S. Kahler, Ann. Rev. Astron. Astrophys. **30**, 113 (1992).
8. S. N. Kuznetsov, A. V. Bogomolov, Yu. P. Gordeev, *et al.*, Izv. Ross. Akad. Nauk, Ser. Fiz. **59**, 2 (1995).
9. R. E. Lingenfelter and R. Ramaty, *High Energy Reactions in Astrophysics*, Ed. by B. S. P. Shen (Benjamin Press, New York, 1967), p. 99.
10. N. Mandzhavidze and R. Ramaty, Astrophys. J. **389**, 739 (1992).
11. N. Mandzhavidze, R. Ramaty, V. V. Akimov, and N. G. Leikov, in *Proceedings of 23rd ICRC* (Calgary Univ., Calgary, 1993), Vol. 3, p. 119.
12. H. Marshhauser, E. Rieger, and G. Kanbach, in *Proceedings of 22nd ICRC* (Reprint Ltd., Dublin, 1991), Vol. 3, p. 61.
13. R. J. Murphy, R. Ramaty, B. Kozlovsky, and D. V. Reames, Astrophys. J. **371**, 793 (1991).
14. V. J. Raben, http://sec.noaa.gov/data/goes.html (2002).
15. E. Rieger and G. Rank, in *The Universe in Gamma Rays*, Ed. by V. Schoenfelder (Spring-Verlag Heidelberg, Berlin, 2002), p. 92.
16. I. A. Zhitnik, I. P. Tindo, and A. M. Urnov, Tr. Fiz. Inst. Ross. Akad. Nauk **195**, 3 (1989).

Translated by A. Dambis